NUMERICAL IMPLEMENTATION OF THE REFINED ZIGZAG THEORY FOR STRUCTURAL ANALYSIS OF CURVILINEAR FIBER REINFORCED COMPOSITE AND FUNCTIONALLY GRADED PLATE STRUCTURES

By

Pouya Zoghipour

Submitted to the Graduate School of Engineering and Natural Sciences
in partial fulfillment of
the requirements for the degree of
Doctor of Philosophy

Sabanci University

July 2023

NUMERICAL IMPLEMENTATION OF THE REFINED ZIGZAG THEORY FOR STRUCTURAL ANALYSIS OF CURVILINEAR FIBER REINFORCED COMPOSITE AND FUNCTIONALLY GRADED PLATE STRUCTURES

Pouya Zoghipour

Ph.D. Dissertation, July 2023

Supervisor: Prof. Dr. Mehmet Yildiz

Co-Supervisor: Assoc. Prof. Dr. Adnan Kefal

ABSTRACT

Keywords: Composites laminates, Sandwich plates (SP), Tailoring, Variable stiffness, Curvilinear fibers, Functionally Graded (FG) materials, Plate kinematics, Refined Zigzag Theory (RZT), Finite Element Modeling (FEM).

The use of composite structures is becoming increasingly prevalent in structural engineering, due to their superior specific strength and stiffness. Fiber steering and functional grading of material to produce a Variable Stiffness (VS) composite or a Functionally Graded (FG) material composite, are two widely used tailoring methods for achieving the desired mechanical properties in composite structures to prevent their failure. However, the increased expansion in the design space for tailoring in these structures can pose a substantial challenge during structural analysis. It is essential to address this challenge by utilizing computationally efficient and accurate evaluations, particularly during determining the optimal fiber angles and the right material Compositional Gradient (CG) profiles based on the mechanical requirements. This study aims to comprehensively adopt and reformulate the Refined Zigzag theory (RZT) to accurately predict the strain and stress of different VS composite and FG sandwich plate laminates under static deformation. Therefore, the second chapter of this thesis proposes an RZT-based model which considers the variation of the curvilinear fiber angles in calculation of the ZigZag (ZZ) functions and utilizes their derivatives with respect to in-plane coordinates in the definition of strains. Also, in the same chapter, the ZZ functions of the proposed model are enhanced to account for the continuous thickness-wise variation of the material. This enhancement allows the model to be capable of analyzing

sandwich panels and composite plates consisting of FG and/or VS layers composite plates. Furthermore, a shear locking-free three node triangle RZT element is adopted to keep the degree of freedom in its minimum level and increase the computational efficiency. In order to accurately predict thickness-wise transverse stresses, a recovery procedure based on the integration of the Cauchy's equilibrium equations is presented. In the third and fourth chapters, by solving numerical problems it is shown that the results of this procedure have a high level of accuracy, comparable to more computationally demanding three-dimensional Finite Element (FE) approaches or other higher-order theories. Therefore, the proposed model in this thesis provides an efficient and accurate method for analyzing VS and FG composite laminates. This model can be reliably integrated to design platforms to serve for tailoring the curvilinear fiber orientations and the material CG profiles and potentially improve the structural performance of these structures.

EĞRİSEL FİBER TAKVİYELİ KOMPOZİT VE FONKSİYONEL DERECELENDİRİLMİŞ PLAKA YAPILARININ YAPISAL ANALİZİ İÇİN RAFİNE ZİKZAK TEORİSİNİN SAYISAL UYGULAMASI

Pouya Zoghipour

Doktora tezi, Temmuz 2023

Tez Danışmanı: Prof. Dr. Mehmet Yıldız

Eş-danışmanı: Doç. Dr. Adnan Kefal

ÖZET

Anahtar Kelimeler: Kompozit laminatlar, Sandviç plakalar (SP), Uyarlamak, Değişken rijitlik, Eğrisel fiberler, Fonksiyonel Derecelendirilmiş (FG) malzemeler, Plaka kinematiği, Rafine Zigzag Teorisi (RZT), Sonlu Eleman Modellemesi (FEM).

Kompozit yapıların kullanımı, üstün özgül dayanımları ve rijitlikleri nedeniyle yapı mühendisliğinde giderek yaygınlaşmaktadır. Değişken Sertlik (VS) kompoziti veya Fonksiyonel derecelendirilmiş malzeme (FG) kompoziti üretmek için fiber yönlendirme ve malzemenin fonksiyonel derecelendirmesi, kompozit yapılarda hasar oluşmalarını önlemek için istenen mekanik özellikleri elde etmek için yaygın olarak kullanılan iki uyarlama yöntemidir. Bununla birlikte, bu yapılarda uyarlama için tasarım alanında artan genişleme, yapısal analiz sırasında önemli bir zorluk oluşturabilir. Özellikle mekanik gereksinimlere dayalı olarak en uygun fiber açılarının ve doğru malzeme bileşimi gradyan profillerinin belirlenmesi sırasında, hesaplama açısından verimli ve doğru değerlendirmeler kullanarak bu zorluğun üstesinden gelmek çok önemlidir. Bu çalışma, statik deformasyon altında olan farklı VS kompozit ve FG sandviç plaka laminatlarının gerinim ve gerilimi doğru bir şekilde tahmin etmek için rafine Zikzak teorisini (RZT) kapsamlı bir şekilde benimsemeyi ve yeniden formüle etmeyi amaçlamaktadır. Bu nedenle, bu tezin ikinci bölümü, zikzak fonksiyonlarının hesaplanmasında eğrisel fiber açılarının değişimini dikkate alan ve gerinimlerin tanımlanmasında düzlem içi koordinatlara göre türevlerini kullanan RZT tabanlı bir model önermiştir. Ayrıca, aynı bölümde, önerilen modelin ZikZak (ZZ) fonksiyonları, malzemenin sürekli kalınlık-bazlı değişimini hesaba katacak şekilde geliştirilmiştir. Bu geliştirme, modelin sandviç panelleri ve FG ve/veya VS katmanlı kompozit plakalardan oluşan kompozit plakaları analiz edebilmesini sağlar. Bunlara ek olarak, serbestlik derecesini minimum seviyede tutmak ve hesaplama verimliliğini artırmak için kayma kilitlenmesiz üç düğümlü üçgen RZT elemanı kullanılmıştır. Kalınlık yönü kayma gerilmelerini doğru bir şekilde tahmin etmek için, Cauchy'nin denge denklemlerinin entegrasyonuna dayalı bir geri kazanım prosedürü sunulmuştur. Üçüncü ve dördüncü bölümlerde, sayısal problemler çözülerek, bu prosedürün sonuçlarının, hesaplama açısından daha zorlu üç boyutlu Sonlu Eleman (FE) yaklaşımları veya diğer üst düzey teorilerle karşılaştırılabilir yüksek bir doğruluk düzeyine sahip olduğu gösterilmiştir. Bu nedenle, bu tezde önerilen model, VS ve FG kompozit laminatların analizi için verimli ve doğru bir yöntem sağlar. Bu model, eğrisel fiber oryantasyonlarının ve malzeme CG profillerinin uyarlanmasına hizmet etmek ve potansiyel olarak bu yapıların yapısal performansını iyileştirmek için tasarım platformlarına güvenilir bir şekilde entegre edilebilir.

To my father,

whose unwavering resolve is akin to that of a mighty mountain.

To my mother,

whose compassionate heart knows no bounds, like the vastness of the ocean.

To my brother,

whose bravery soars high like the endless expanse of the blue sky.

Acknowledgment

With the utmost humility and gratitude, I humbly express my appreciation to all those who have aided and guided me on my research journey.

Above all, I offer my deepest appreciation to my supervisor, Prof. Dr. Mehmet Yildiz, whose remarkable mentorship, sagacious insights, and steadfast encouragement have been invaluable in enhancing my skills and knowledge in the field of composite materials.

I extend my heartfelt thanks to my co-supervisor Assoc. Prof. Dr. Adnan Kefal and Asst. Prof. Dr. K.A Hasim for their unwavering support, motivation, and advice throughout my research journey.

I cannot forget the unwavering support of my cherished friends and supporters, Sefa Yildirim, Kathi Wyldeck, Ali Fallah, Morvarid Safari Vesal, Ammar Saleem, Turkhan Khalilov, Ata Alipour, Wael Al-Dulaimi, Fatih Basoglu, Ali Tufani, Farzin Asghari, Samad Nadimi, Adnan Tasdemir, Deniz Kisakol, Cagan diyaroglu, and Muhammed Cakir, Kaveh Rahimzadeh Berenji who stood by me through thick and thin.

My research experience would not have been as rich and rewarding without the guidance and collaboration of my exceptional research colleagues and friends, Isa Emami Tabrizi, Shayan Ramezanzadeh, Roozbeh Saghatchi, Abdalrahman Al-Nadari, Hafiz Qasim Ali, Mohammad Amin Abdollahzadeh, Sasan Karimi, and Sina Khalilvand, Dilay Serttan. Their insightful discussions and support have been instrumental in shaping my research experience.

I am deeply grateful to my parents and brother for their unwavering love, encouragement, and support throughout my academic journey. Their immeasurable sacrifices and unwavering support have been the driving force behind my success.

Finally, I express my profound gratitude to Sabanci University and SU-IMC for their generous support and resources that made my research possible.

TABLE OF CONTENTS

List of Figures

List of Tables

1 INTRODUCTION

Material technology directly impacts the efficiency and effectiveness of human activities and plays a pivotal role in shaping our world. With the growing manufacturing industry, materials that offer better strength, affordability, and environmental sustainability are becoming increasingly important. In this regard, many applications demand materials with conflicting properties which are not achievable with a single, monolithic material. As a result, as a viable solution composite materials have been introduced due to their superior properties and potential for use in multiple applications [1–3]. These materials consist of a combination of two or more components, known as the matrix phase and the reinforcement phase namely particles or fibers. The combination of the matrix and fibers offer superior performance when compared separately to either of these components. It has been demonstrated in many research studies that Fiber-Reinforced Composites (FRCs) can serve to be an alternative to their conventional metal counterparts due to significant improvements in their structural, mechanical, and tribological properties [3–5]. The design technique of conventional Constant Stiffness (CS) composites with Unidirectional (UD) fibers entails a consistent selection of fiber angles of the plies, ply number, thickness, and constant material properties throughout each lamina [6]. These structures are also known as Constant Stiffness Composite Laminates (CSCL). However, with the advent of new technologies such as Automated Fiber Placement (AFP) and Three-Dimensional (3D) printing, a further extension beyond CS design space can be achieved through a tailoring strategy that allows stiffness to vary across different regions of the structure and improves material efficiency and structural performance. Composite tailoring involves the selection and modification of components, as well as engineering interfaces [7]. In this thesis, two tailoring strategies are pursued. The first strategy includes fiber steering, and the second strategy entails material tailoring or functional gradation. Fiber steering refers to varying the fiber angle with a rule locally relative to the in-plane coordinates, and functional gradation refers to modifying the composition and structure of the composite material. Fiber-steered composites are referred to as Variable Stiffness Composite Laminates (VSCL) [8–10], whereas Functionally Graded (FG) materials [11–17] are tailored multifunctional materials. The determination of mechanical requirement-driven fiber angles, and the proper material CG profiles necessitates the utilization of novel optimization methodologies [18–21] integrated with fast and robust mechanical analysis tools that minimize the undesirable failure modes for these structures. In this regard, this thesis aims to develop an accurate, time-efficient, robust, reliable, and low-cost computational model to perform structural analysis on VSCLs and Functionally Graded Sandwich Plates (FG-SP). This computational model utilizes the Refined Zigzag Theory (RZT) as its basis. Recently, the RZT was provided for multilayered composites and Sandwich Plates (SP), with the kinematics of First-Order Shear Deformation Theory (FSDT) serving as its foundation. RZT by enriching these kinematics with linear ZZ functions, provides accurate estimations of the in-plane displacements [22,23]. The theory was derived from the principle of virtual work in a variationally consistent manner. The RZT avoids the shortcomings of prior ZZ theories that limited their accuracy and enhances efficient adaptation to FE modeling frameworks [22–28]. The majority of structural investigations on composite structures using RZT are primarily concerned with beam, plate, and shell laminates with UD fibers. Nonetheless, RZT in its original form is ineffective for modeling true variation of in-plane displacements of VSCLs and FG material structures due to their complexity. That is, for in-plane curvilinear fiber reinforcements, the average shear rigidities depend on in-plane coordinates, whereas for thickness-wise material variation within the FG layers, these terms need to be continuously regulated along the thickness coordinate due to the variation of the elasticity modulus. Therefore, a modification to the original theory is essential. To the best of the authors' knowledge, no prior research in the literature has been dedicated to providing a robust mathematical RZT-based formulation for structural analysis of laminated plates with curvilinear fiber reinforcements and/or FG materials. Therefore, in this research by adding further to the predictive capabilities of the original RZT, a novel comprehensive model is proposed to address this shortcoming in two steps. The first step involves the development of a model capable of performing accurate static analysis of the composite and SPs reinforced by curvilinear fibers with computational efficiency using a three-node triangle element. In the second step, the developed model is enhanced to predict the behavior of FG material layers in the presence of curved fibers in composite laminates. The accuracy, performance, and computational efficiency of the proposed model are assessed and validated through bending analysis of several VSCL plates with various curvilinear fiber paths and different span-to-thickness ratios. The obtained results from the proposed formulation are verified with reference solutions available in the literature and those generated by high-fidelity 3D ANSYS models. They reveal remarkable benefits of the proposed model for predicting highly accurate displacement and stress distributions of VSCLs. Furthermore, CPU runtime comparisons of RZT3C, QUAD-RZT4, and 3D Ansys solid 185 components show the computational efficiency and superiority of the proposed model.

Additionally, by utilizing the proposed enhanced RZT model, this thesis investigates the flexural behavior of moderately thick SPs made of FG material core and curvilinear fiber-reinforced face sheets as novel hybrid composites under various lamination schemes, loading, and boundary conditions, for the first time in the literature. The increased performance of hybrid composites because of the regulated strength and stiffness through rigorous analysis is demonstrated to be potentially utilized to enhance the structural integrity, and durability for a wide range of applications. The author is aware that no prior study has reported the use of the three-node shear-locking free triangle RZT element formulation for analyzing the displacements and stresses for SPs with FG material cores and VS face sheets at a lower computational cost and acceptable accuracy. The comprehensive numerical results highlight the key factors affecting structural performance and provide valuable insights into the design and tailoring of composite sandwich structures with FG cores and VS face sheets. Thus, the obtained results of this study can be reliably used as potential benchmark solutions for future research in this area.

The final section of this thesis is designated to the concluding remarks drawn from the presented numerical results based on the proposed formulation.

1.1 The curvilinear fiber reinforcement concept

The FRCs are classified based on the length of their fibers as discontinuous FRCs with short, and continuous with long fibers. Generally, the composites reinforced by continuous fibers show high specific strength and modulus, enabling them ideal candidates for aerospace, automobiles, ships, and high-speed trains [29–31]. In continuous FRCs, the fibers can be arranged either unidirectionally [32–34] or curvilinearly [35–38] within the matrix. In these composites the load transfer interaction between the matrix and fibers is in a highly efficient manner, and the orientation of the fibers determine the mechanical behavior [39,40]. In composite structures subjected to combined loadings, stress distributions are not uniform. The UD FRCs perform weakly against stress concentration leaving the efficiency of the composite material decrease [35,41]. The utilization of curvilinear FRCs can be a promising approach to tackle this problem [8–10]. In curvilinear FRCs, the variation of the fiber orientation with respect to spatial in-plane position results in a controlled and varied local stiffness of the structure. Fig. 1-1 depicts the schematic of CSCLs and VSCLs respectively. Aside from using curvilinear fibers, various other techniques can also modify panel stiffness to obtain VSCLs. For instance, in plates with in-plane variation of material properties (in-plane FG plates) can also be considered VSCL plates [42]. However, for the purposes of this thesis, the term Variable Stiffness (VS) refers specifically to laminates in which the fiber angle within a ply can continuously change with spatial location. This distinction is important to clarify the specific focus of the research being conducted.

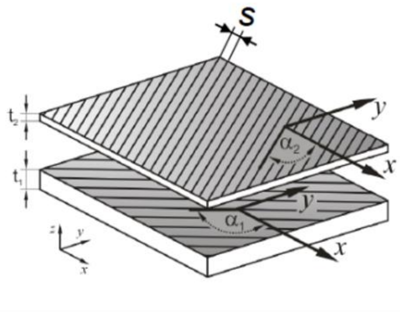

(a)

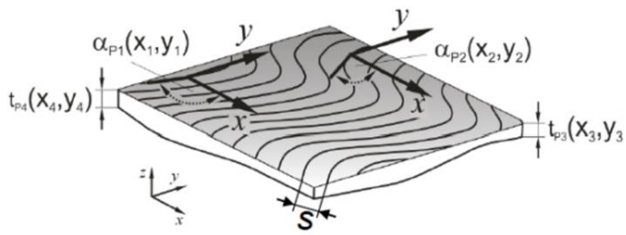

(b)

Fig. 1-1 Schematic of (a) CSCL and (b) VSCL [43].

1.2 The curvilinear fiber path

In a lamina, fibers can theoretically follow any pattern. One possible pattern that fiber orientation may follow is a curvilinear fiber path. Generally, in curvilinear FRCs, all fibers follow a path defined for a reference curvilinear fiber. There are two common methods to define the curvilinear fiber path for non-reference fibers. These methods are known as parallel and shifted methods [42]. Fig. 1-2 depicts the reference fiber path of the curvilinear lamina.

1.2.1 The shifted curvilinear fiber path method

In this technique the reference fiber path is constructed as the first step and then the reference fiber path is translated by a defined amount along y axis to construct the rest of the paths [42]. Fig. 1-3a represents the shifted curvilinear path in a composite plate. For the shifted curvilinear fiber path method, the curvilinear fiber path is only a function of x-direction. In this thesis, the curvilinear fiber paths are defined based on the shifted method.

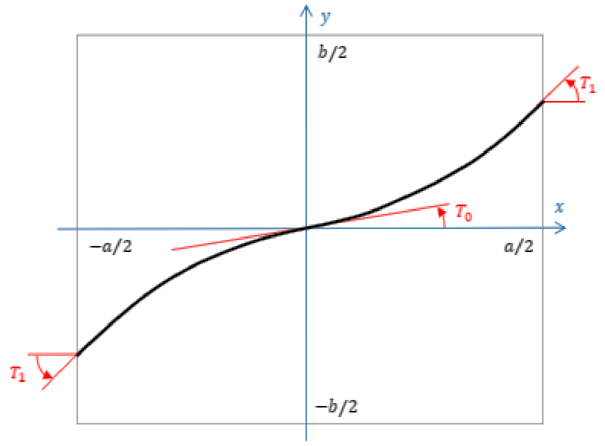

Fig. 1-2 Reference curvilinear fiber path [42].

1.2.2 The parallel curvilinear fiber path method

This technique constructs the curvilinear fiber path as a group of locations parallel to the reference curve. Hence, each fiber curve maintains a fixed distance from the other fiber path. In contrast to the shifted fiber technique, in this method the curves of non-reference fibers do not necessarily follow the same analytical rule as does the reference one. As is seen in Fig. 1-3b. the curvilinear fiber orientation for the two points A and B, with the same x coordinate, are not equally the same [42].

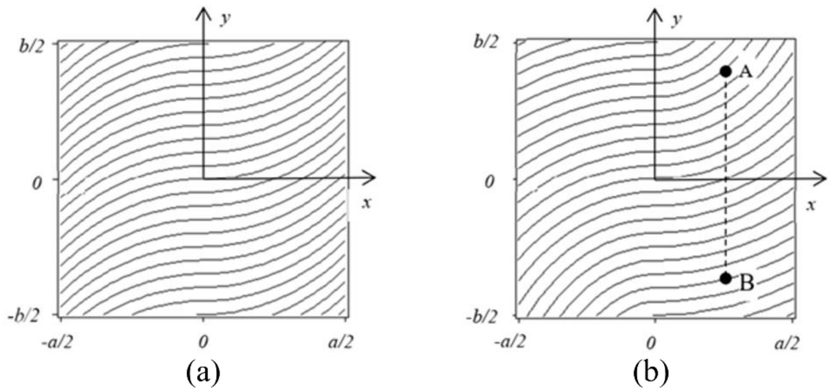

Fig. 1-3 Curvilinear fiber path (a) Shifted (b) parallel [42].

1.3 Functionally graded material composites

Albeit having improved properties such as stiffness, and weight reduction, laminated composites perform weakly in their laminae’s interfaces due to the discontinuity of the properties and stresses. Using FG materials is a technique to mitigate this issue. The FG material concept was first introduced to minimize thermal stress in the aerospace structures [44,45]. FG materials are categorized as composite materials with an inhomogeneous distribution of constituents [46]. The volume percentage of each constituent (phase) of an FG material varies continuously/discontinuously while moving in a certain direction (Fig. 1-4) [47–49]. This results in the substitution of sharp contacts with gradient interfaces, and reduces the mechanical/thermal mismatch between two discrete adjacent zones [50]. As is seen in Fig. 1-4a and Fig. 1-5a, for the continuous FG materials, the variation of the constituents as well as the material properties has no positional separation zone within the domain of the FG. However, for discontinuous FG materials this does not hold true (Fig. 1-4b and Fig. 1-5b) [51,52].

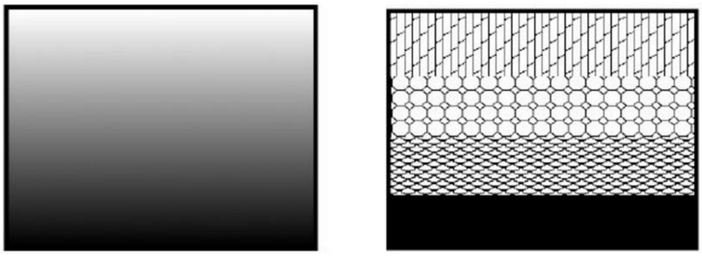

(a) (b)

Fig. 1-4 The structure of FG material (a) continuous FG (b) discontinuous FG [51].

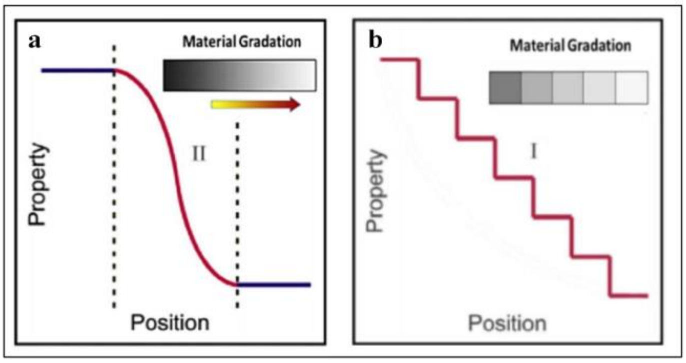

Fig. 1-5 The distribution of the material properties for (a) continuous (b) discontinuous FG material [53].

Depending on the desired design and functionality, the FG material composites can be tailored both with internally/externally specific non-uniformity in the structure and composition [54]. Several configurations of composite plates with FG material layers include SPs with FG face sheets and a homogenous core or an FG core and isotropic/orthotropic face sheets, and FG material in all layers. Fig. 1-6 Shows all combinations of the possible configurations of the FG-SPs [55]. In this thesis, the FG-

SPs are assumed to be plates with orthotropic composite face sheets (skins) and an FG core made of a two-phase material (soft foam).

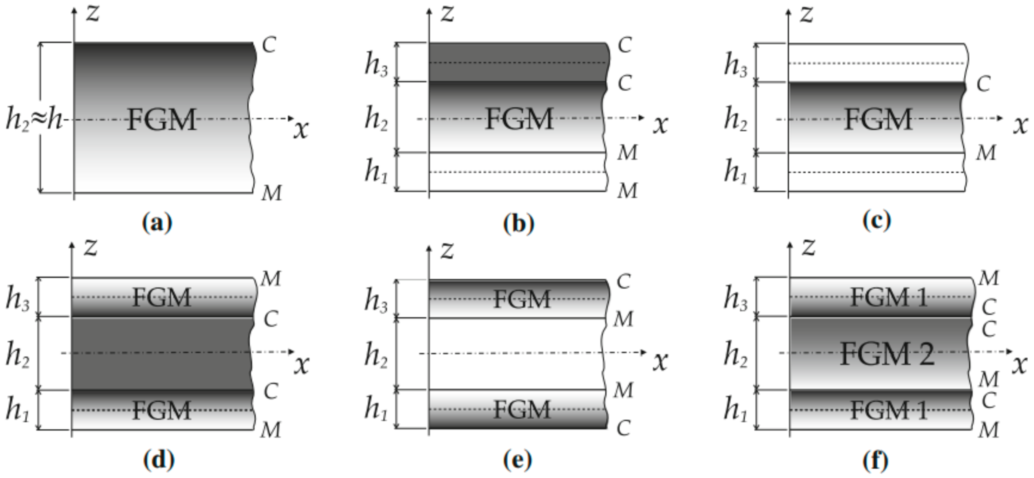

Fig. 1-6 Configurations of an FG-SP (a) an isotropic FG panel with very thin face sheets (b) and (c) homogeneous/composite face sheets with an FG core (d) and (e) FG face sheets and a homogeneous hard/soft core (f) both FG face sheets and an FG core [55].

1.4 Homogenization

In FG materials made up of distinct constituents, the change in the volume fraction of each constituent results in the variation of the effective material properties along the gradation direction. Therefore, for a mechanical model to predict the behavior of an FG material, the estimation of the effective properties of the two or multi-phase composition is required. Usually, a homogenization method provides an approximation of the effective properties in FG materials in the absence of information about the size of the dispersed phases, and their distribution. It is therefore necessary to make assumptions based on the distribution of volume fractions of each phase. In the literature, various homogenization models the such as Voigt model or the rule of mixture [56], the Mori-Tanaka scheme [57], and the self-consistent method [58] have been developed and compared in terms of their capability in determining the effective properties of FG materials. The Voigt model, estimates the effective properties of the FG material by taking the average of strain/stresses all present constituents with the assumption that their distributions are uniform [59]. Nonetheless, for the Mori-Tanka [57] and self-consistent homogenization models [58] the average of these fields are taken locally. Hence, the Mori-Tanaka model is useful for analyzing periodically dispersed discontinuous particulate-based reinforcements. However, the Voigt model is a quick and easy way to predict overall material properties and structural responses in continuously graded materials [60]. Several Other methods to determine the effective properties of FG materials have been developed by other researchers [61–63]. Below, the Voigt model is briefly introduced.

1.4.1 The Voigt model.

The Voigt homogenization model is utilized to determine the effective elastic properties in various single or multi-directionally graded FG materials [64–66]. In this model, P, an FG material's arbitrary property varies based on the variation of the constituents' volume fractions and properties [64]. The following is the mathematical relationship describing the property P:

$$P = \sum_{i=1}^{n} P_i V_i \tag{1.1}$$

In the above formulation, the i^{th} FG material constituent is characterized by its property P_i and volume fraction V_i, where the sum of all the volume fractions equals unity [64].

1.4.2 Gradation Laws (Material gradation profiles)

In FG materials, the Compositional Gradient (CG) of the constituents in a multi-phase material is fulfilled according to a predetermined profile. This profile or the gradation law regulates the variation of volume fractions based on the spatial position and results in continuously graded macro properties [67]. In the literature, the power-law, exponential-law, and sigmoid-law are among the commonly used gradation laws [66].

1.4.2.1 The power-law

The power law for material gradation is frequently used in analyzing the stresses in FG material plates and shells with uniform thickness [68]. Wakashima et al.[69] initially proposed this law. For the FG plate shown in Fig. 1-7, the gradation-wise local volume faction of the constituents according to power-law holds as the following relation [67]:

$$v(z) = \left(\frac{z + h/2}{h} \right)^n \tag{1.2}$$

where h, and z respectively represent the thickness, and n is the Compositional Gradient Index (CGI) or CG exponent which can theoretically vary in the range,

$0 \le n \le \infty$ [64]. In general, the function $v(z)$ can be any non-negative function of z that is not singular [70].

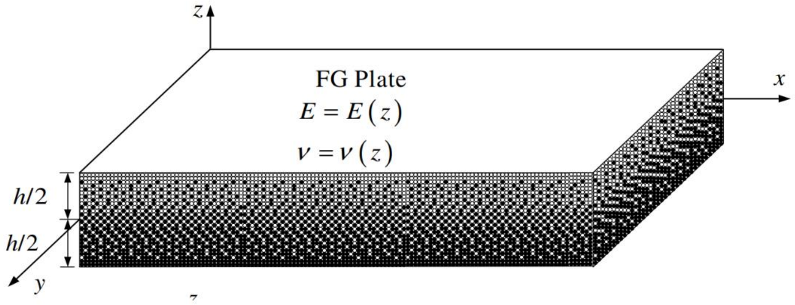

Fig. 1-7 Uniform thickness FG plate [67]

1.4.2.2 The Sigmoid-law

Using a single power-law function to describe the variation profile of volume fraction can result in stress concentration. This is because for values of n less or greater than one, the value of volume faction changes abruptly near the surfaces [67]. Therefore, describing the volume fraction with two power-law functions, results in a more gradual change. The explicit definitions of the two power-law functions (volume fractions) are as follows [67]:

$$v_1(z) = 1 - \frac{1}{2}\left(\frac{h/2 - z}{h/2}\right)^n \text{ for } 0 \le z \le h/2 \tag{1.3}$$

$$v_2(z) = \frac{1}{2}\left(\frac{h/2 + z}{h/2}\right)^n \quad \text{for } -h/2 \le z \le 0 \tag{1.4}$$

1.4.2.3 The Exponential-law

The exponential profile for the variation of the volume fraction of the constituents in FG plates is described as [71]:

$$P(z) = \alpha e^{\beta\left(\frac{h}{2}+z\right)} \tag{1.5}$$

with,

$$\alpha = P_1, \text{ and } \beta = \frac{1}{h}\ln\left(\frac{P_2}{P_1}\right) \tag{1.6}$$

where P_1 and P_2 are the predetermined properties at the bottom and top surfaces of the FG material [71].

1.5 State of art on Modeling

The VSCL and FG composite structures offer a wider range of design options than CSCLs. A reliable design requires an accurate evaluation of strain and stress states. This brief review focuses on the state of art regarding the modeling of VSCL and FG composites. Relying solely on analytical solutions to predict the mechanical response of VS and FG laminated structures may be insufficient. In the absence of an exact solution, detailed 3D Finite Element (FE) models are frequently required to perform high-fidelity analyses of VSCLs and FG composite structures within a multidisciplinary design and optimization framework. However, the high accuracy of 3D continuum FEM comes at an enormous computational cost. To model the VSCL and FG composite laminates, researchers have focused on developing approximated models that compromise accuracy and computational efficiency. The two types of approximate models are the displacement-based, and the mixed models. Displacement-based models assume displacements as the primary variable and they are developed on the basis of the virtual displacement principle [72], while mixed models assume displacements and stresses independently and are developed according to the Reissner’s Mixed Variational Theorem [73]. With a main concentration on approximate modeling techniques, the following two sub-sections provide the state of art on modeling VSCL and multilayered FG composites respectively.

1.5.1 The VSCL modeling.

The proper design of the fiber path in VSCLs assists the improvement of stress redistribution from weak to strong areas within the domain of the structure, and the reduction of stress concentration [74]. The spatially varying orientation of fibers has been demonstrated to improve VSCLs’ mechanical behavior in several studies [75–77]. For instance, Ijsselmuiden et al. [78] showed that the locally tailored VSCLs tolerate substantially more compressive load before buckling. Nonetheless, finding the spatially varying optimal fiber orientation in the optimization platforms relies on accurate and efficient modeling techniques. In this regard, modeling of VSCLs has become a major area of research after the initial discussion of the pioneer studies in this area in refs.[79,80].

Khaneh et al. [81] analytically investigated the static deflection of VS composite beams under non-uniform loads and changed the coefficients of the governing differential equations to express VS properties. To investigate thin-walled VSCL beams, Gunay et al.

[82] proposed an analytical approach that takes bend-torsion coupling, warping impacts, and VS along the beam's cross-section into account. For analyzing composite structures, plate and shell models are among the best approximated models. Several studies in literature have reported the use of these models to estimate the strain, stress fields, and critical failure conditions of curvilinear fiber reinforced laminates. For the most part, these approaches use FE discretization to form and solve their governing equations. Jegley et al. [83] in their research, have underlined the relevance of extra-fine FE discretization for the exact and smooth modeling of curvilinear fibers in VSCLs. However, the use of the extra high-resolution mesh significantly increases the degrees of freedom in a numerical system. As a result, this FE model, when paired with the necessary optimization procedures, necessitates extensive computing effort [84]. In the open literature, approximate models have been dominantly used to model the mechanical behavior of VSCLs. Among these models, approximate axiomatic displacement-based models are generally classified into three types: Equivalent Single Layer (ESL) models [85–92], Layer-wise theories (LW) [93–98], and ZZ models [99–104]. To predict the stress fields in the ESL models, an assumption is made for thickness-wise distribution of displacement components, resulting in the reduction of the 3D problem to a 2D problem. The Classical Plate Theory (CPT)/Classical Laminate Theory (CLT), and the FSDTs are the most basic ESL methods. Antunes et al. [105] studied the modal behavior of the VSCL plates by comparing the experimental results with those of the CPT, and the FSDT under different boundary conditions. She reported that for the thin plate, the results of the CPT and the FSDT are almost identical. In another study, Setoodeh et al. [38] used a conforming CPT approach to carry the buckling analysis of the rectangular plates in conjunction with a reciprocal approximation to update the fiber angle in the VSCL. Ganapathi et al. [106] by employing an FSDT approach, considered the variation of the continuous fiber orientation in composite plates, and proved that the critical buckling behavior of the laminates with higher fiber angles at the edges and lower in the center improves.

In spite of the fact that simple 2D ESL models are efficient in computation and can accurately predict a structure's global response, they fail to predict local responses for thick laminates with high anisotropy. In particular, the CLT [107] ignores transverse shear stresses, whereas the FSDT [108,109] assumes transverse shear strain distribution throughout the plies' thickness to be constant [110]. As a result, these theories have limited accuracy due to their assumptions made for field variables. To obtain precise thickness-wise stress components, both theories require a subsequent step such as solving the Cauchy's equilibrium equations [91,111–113]. To address these issues, it may be necessary to use ESL Higher-Order Shear Deformation Theories (HSDT) or LW theories to model the VSCLs [114,115]. Using the Third Order Shear Deformation Theory (TSDT) and a new p-version FE, Akhavan et al. [116] investigated the behavior of VSCL plates with curvilinear fibers subjected to large deflection and stresses and found that large deflection of VSCLs reduces when the fiber orientation linearly varies in the plate.

Compared to ESL HSDTs, LW theories, on the other hand, provide more accurate local response predictions, and thereby more accurate state of 3D stress fields in thick laminated composite structures [97,114,117]. There is a wide range of applications in the literature that utilize LW theories for modeling VSCLs [118–122]. An important study in this field was conducted by Pagani et al. [118], in which the buckling performance of VSCLs with misaligned fibers were modeled using an LW approach and utilizing Carrera's unified formulation (CUF). Diaz et al. [120] utilized Fagiano et al.'s LW interlaminar stress recovery methodology [122] in modeling VSCLs to obtain continuous stress profiles through-the-thickness of laminate. In another study, Yazdani et al. [121] used a p-type FEM supplemented with thickness-wise displacement functions to account for the ZZ behavior in the asymmetric VSCL plates in a LW manner.

In laminated composite or sandwich structures, the ESL theories do not precisely capture the ZZ effect which is caused by the severe transverse anisotropy. This is because the ESL does not account for the thickness-wise discontinuity of the first derivatives of in-plane displacements [123]. Therefore, ESLs may not always accurately capture the 3D state of stress. On the other hand, modeling multiple-layered thick composite laminates with LW models features a significant challenge due to the increase in the number of unknown variables leading to a dramatic computational cost [89]. Moreover, the use of these techniques with high-order Lagrange/Legendre polynomials would result in a high complexity, regardless of accounting for the thickness-wise discontinuity in the slope of the in-plane displacements [124,125]. From the other side, while the LW methods capture the state of stresses with higher accuracy as compared to ESL methods, the continuity of the transverse stresses is still not assured [10]. In response to these issues, ZZ theories were devised to minimize the computational cost by keeping the number of kinematic variables constant without scarifying the accuracy [100–103].

The first ZZ theory was proposed by Di Sciuva [99], to model the multilayered composite and sandwich structures. In ZZ theories, piecewise ZZ distributions of in-plane displacements as well as the constant transverse shear stresses are captured through-the-thickness of the laminate/lamina while keeping a fixed number of kinematic variables with no regard to the number of material layers [22,126–131]. To capture the actual stress fields with admissible computational cost, special attention was dedicated to the development of various ZZ theories. In this regard, many studies implemented higher-order terms in previously proposed ZZ functions [22,97,126,132,133]. To avoid discontinuous shear stresses during the static analysis of constant/variable laminates, Luan et al. [134] employed the Hellinger-Reissner mixed variational principle. His study used different order ZZ kinematics to form governing equations of bending and stretching, which were then solved by using a mixed inverse Differential Quadrature Method (DQM). To obtain accurate predictions of the in-plane response of the shear deformable composite plates, Murakami [92] developed a plate theory based on Reissner’s variational principle [90]. The theory, which later referred to as Murakami’s ZZ function (MZZF) [104], and included ZZ shaped functions to approximate the thickness-wise variation of the in-plane displacements. MZZF was included in linear and higher-order expansions for in-plane and out-plane displacements to model the layered structures [135]. Gupta et al. [136] used MZZF function in the linear/non-linear static analysis of VSCL shells. To account for geometrical nonlinearities, he used a nine-node isoparametric element and von Kármán relations.

In combining MZZF with numerous structural theories (beam/plate/shell theories of various orders linear/higher-order), Carrera et al. [137] proposed a unified formulation (CUF) which treated the displacements as the unknowns variables. Demasi et al. [138–140] took one step further and expanded the CUF to a more general form named the General Unified Formulation (GUF). In GUF, all displacements are independently expanded of the same order along the thickness direction for ESL, ZZ (MZZF), and LW theories. The independent modeling of each displacement component in GUF allows for a larger number of axiomatic theories compared to CUF. Both CUF and GUF have been used for modeling the VSCLs. For instance, Demasi et al. [141] extended the GUF to the case of fourth-order triangular shell elements with variable thickness in VSCLs. VSCLs have extended beyond straight plates and many investigations have been conducted on the cylindrical, conical, and doubly curved shell VSCLs [142–145]. Tornabene et al.

[146,147] investigated the static and dynamic response of the singly and doubly curved VSCLs. In his modeling approach, a combination of higher-order theories in the framework of CUF, and the governing equations were solved locally by the generalized DQM. In another study, Tornabene et al. [142] included MZZF in various HSDTs to capture the ZZ effect in a soft-core SP with curvilinear fibers in the skins under static loading. There are also other studies that have used the strong form of the Unified Formulation (UF) to reduce the computational cost. Ojo et al. [148] proposed a geometrically nonlinear Strong Unified Formulation (SUF), and demonstrated the improved response of VS composites under large deflections by analyzing their 3D stress state. In another study, Patni et al. [149] used a Unified displacement-hierarchical Serendipity Lagrange Finite element (UF-SLE) to remove anomalies (mathematical singularities) caused by the presence of the absolute value in the fiber orientation function to predict accurate 3D stress fields even around local features of VSCLs.

In the literature, attempts to model the VSCLs include both higher-order and ZZ theories as well as UFs which accommodate the former two. These efforts have covered the prediction of the normal and transverse shear deformations, the thickness-wise variation of the ZZ effect because of the presence of anisotropy in multi-layered structures, and fulfilling the thickness-wise continuity of the displacements and the interlaminar transverse stresses [150–152]. No matter what order theory is employed to model VSCLs, accurate approximation of the curved fiber paths requires fine discretization of the geometric domain. Even for basic sine/cosine fiber paths, a minimum third-order element type is required unless the kinematic equations account for the curvature of the fibers. Nonetheless, this can be computationally incommodious. Therefore, there is a pressing need for an alternative and computationally efficient approach. Given that the ZZ theories are introduced to improve the thickness-wise distribution of the in-displacement fields, the ZZ function should be chosen so that the desired accuracy is obtained, especially for unsymmetric and arbitrary lay-ups [153] with curved fiber path in the layers. In this context, the RZT was developed by Tessler et al. [22,23] for investigating the static response of sandwich beams, composite plates, and shell structures, might be a suitable candidate theory for analyzing the VSCLs. Since the concentration of this thesis is on RZT, the literature review for the RZT and the research on VSCLs based on this theory will be provided in a separate sub-section.

1.5.2 FG material modeling.

Understanding the mechanical behavior of the FG material laminates is crucial to be able to use them effectively in engineering structures. Current efforts in literature on these layered structures have mainly focused on the modeling of FG core/face sheet in the SPs and/or on single/multi-layered plates using analytical and numerical approaches. Some examples of noteworthy papers on modeling of FG materials include the following studies. Vel et al. [154] developed an accurate analytical method to capture the 3D deformations of FG thick rectangular plates and employed the Mori-Tanaka/self-consistent approaches to determine the effective material properties. Kumari et al. [155] investigated orthotropic Levy-type plates using the elasticity approach and reported that the in-plane variation of material properties highly improves flexural behavior. Pan [156] proposed an accurate 3D solution for rectangular FG anisotropic elastic single/bi-layered composite plates exposed to sinusoidal pressure, based on Pagano's [157] solution. Handling 3D analytical solutions can be time-consuming and challenging because of their mathematical complexity. Therefore, these solutions can be used for straight forward geometries and boundary conditions [64]. To address these problems, 3D continuum element FEM can be replaced by 3D analytical solutions to expand the domain of solutions to complex geometries while preserving the accuracy. Nonetheless, albeit having accuracy in results, solid element solutions come at a significant cost particularly for tailored FG structures which demand for very fine discretization along the grading direction.

As alternatives to analytical and 3D FEM solutions, meshless methods have gained attention to accurately analyze isotropic/FG composite and SPs with varying shapes and boundary conditions. Fouaidi et al. [158] combined the FSDT and Multiquadric radial basis functions to investigate the linear bending response of FG composite beams. In his study, the effective Young's modulus and the equivalent Poisson's ratio were obtained by the modified Halpin-Tsai model and the rule of mixture, respectively. In another study, Karamanli et al.[159], employed a quasi-3D theory of shear deformation and the Symmetric Smoothed Particle Hydrodynamics (SSPH) method to analyze the static response of bidirectional FG material sandwich beams under various boundary conditions. Based on SSPH and Reddy-Brick’s TSDT, Li et al. [160] proposed an improved accurate approach using the Taylor’s series expansion to analyze the bending behavior of the bi-directional FG material beams. Ferreira [161,162] studied the structural deformations of FG plates by utilizing the meshless collection approach employing Multi Quadrics basic functions and TSDT. Several challenges associated with meshless methods are as difficulty of boundary conditions enforcement, increased number of variables by Lagrange multipliers, the augmented computational cost of iteration due to the insufficient/incomplete convergence [163], instability, and lack of accuracy [164,165]. Hence, the use of a proper approximate displacement-based method can be a good way to counteract these problems.

The CPT has been reported to be used in the static analysis of thin FG plates. For instance, Zenkour et al. [166] investigated the bending response of FG-SPs under sinusoidal thermo-mechanical loads and compared the results obtained by CPT with other HSDTs and analytical solutions based on the Navier procedure. Due to the limitations of the CPTs, the research on FG composite plates concentrated on a more accurate approach, FSDT. In this context, Reddy et al. [167] studied the axisymmetric bending and stretching of circular and annular FG plates, and correlated the results of FSDT with those of CPT. Mantari et al. [168] used a FSDT to evaluate the impact of the shear correction factor and material variation on the static behavior of FG plates. To investigate the nonlinear bending behavior of the FG plates, Singha et al. [169] developed a high-precision formulation based on FSDT by taking into account the position of the exact/physical neutral plane to obtain the correct transverse shear stresses from the equilibrium equations. In addition, some studies on FG plates using FSDTs have attempted to reduce the need for shear correction factor while increasing accuracy. Thai et al. [170] proposed a new four unknown FSDT for structural and vibration analysis of FG-SPs with FG skins and an isotropic core. The theory did not require shear correction factors because transverse shear stresses were calculated directly from equilibrium of transverse shear forces. For predicting the static behavior of doubly curved shells and revolving laminated panels made of FG material, Tornabene et al. [171] devised a 2D Generalized Differential Quadrature (GDQ) solution based on FSDT which included the initial curvature via generalization of the Reissner-Mindlin theory. Although the FSDT is simple and efficient for analyzing thin to moderate plates, the results obtained for thick FG plates remain rudimentarily rough and the accuracy is highly dependent on the proper selection of the shear correction factor [172,173].

To address associated problems with CPTs and FSDTs as well as improving the accuracy, many studies concentrated on developing and implementing HSDTs in analyzing FG structures [174–176]. Using a HSDT and assuming a quadratic thickness-wise distribution for the transverse shear stresses to avoid the need for shear correction factors, Gulshan Taj et al. [175] investigated the static behavior of FG plates. For analyzing bending of FG-SPs, Daikh et al. [177] suggested an HSDT and showed the material gradation impact on deflection and stresses. Many non-polynomial HSDTs have recently been proposed to improve the accuracy and computational cost of the previous HSDTs. For instance, Mahi et al. [178] proposed a theoretical hyperbolic model for shear deformation for FG-SPs' bending. To study the static flexural and vibration response in FG plates, Mantari et al. [176,179] developed a novel non-polynomial HSDT to account for proper distribution of the transverse shear strains through the FG plate's thickness and avoid the need shear correction factor. HSDTs offer better accuracy than simpler approaches like CLT and FSDT in representing strain and stress fields of FG structures [10]. However, the presence of multiple layers of FG material in structures further limits the applicability of HSDTs due to the complexity of the mathematical equations in adaptation to varying material properties. As a result, because of the inclusion of more dependent unknowns by the increase in the power of the thickness coordinate, and the need for shear correction factors to adjust thickness-wise transverse stresses in HSDTs [180], some other studies implemented and improved the LW theories for more precise predictions of the 3D state of stresses the FG structures. These studies have discretized the in-plane displacement and transverse fields by 2D and 1D interpolations respectively [10].

In this context, a higher-order LW approach was used by Pandey et al. [181] to study the static and dynamic characteristics of FG-SPs while maintaining the interlaminar displacement continuity. An LW multi-layered shell model based on isogeometric formulation and the assumption of C^0-continuous transverse displacement was presented by Liu et al. [182] to analyze laminated composites and FG-SPs. Hirane et al. [183] proposed a novel C^0-continuous LW FEM for analyzing the static and free vibration of FG-SPs which employed a higher-order displacement field for the core and a first-order displacement field for the face sheets to ensure layer continuity. Although LW theories accurately calculate interlaminar stress and predict the ZZ shape of displacements, they have a high number of unknowns when dealing with many layers of a thick laminated composite or FG material plates. This is because the LW models treat each layer separately and combine them using interlaminar relations to maintain displacement continuity and stress equilibrium [184]. This procedure leaves these methods susceptible to drastic computational costs when it comes to analyzing the behavior of FG laminates.

Aiming to reduce the number of the DOF of the problem and the computation, UFs, which combine multiple axiomatic theories such as ZZ theories, were adopted to FG structures' analysis [10]. Carrera et al. [185] studied the effect of thickness stretching in single and multilayered FG plate and shell structures by utilizing the CUF, for linear to fourth-order thickness expansion of transverse displacement. He pointed out that if transverse normal strain effects are not considered, classical theory refinements may be ineffective. Mantari et al. [186] used the CUF to accommodate five different non-polynomial displacement fields of sinusoidal, tangential, exponential, hyperbolic, and modified sinusoidal to analyze the static response of simply supported FG single and SPs subjected to a bi-sinusoidal load. Rahmani et al. [187] investigated the vibration and bending properties of FG beams by combining the CUF with isogeometric analysis. In addition to using CUF for analyzing the mechanical behavior of FG composite plates, many other studies have adopted Demasi's GUF [141]. Gorgeri et al. [188] analyzed free vibration and bending behavior of FG cylindrical sandwich panels using formulation S-GUF formulation. The SUF-GUF enables tuning the kinematic description of displacement fields independently in different thickness subregions of heterogeneous material layers of complex FG problem.

Recalling that the major limitation of displacement-based ESL methods is the lack of consideration of the C^1-discontinuity (C^0-continuity) of in-plane displacements in the thickness direction [123], any prediction with UFs in the form of ESL approaches without taking into account ZZ functions would not be flawless. Incorporating ZZ displacements leads to a more computationally accurate and efficient formulation [123]. The effectiveness of including the discontinuity of the first displacement derivative in axiomatic modeling has been demonstrated in many studies [189,190]. In recent years, the trial to capture the ZZ displacements in FG sandwich structures has prompted the development and use of accurate ZZ-based modeling approaches. An FE model based on ZZ theory was developed by Khan et al.[191] for the static response and free vibration of FG material beams. Linear interpolation and cubic Hermite interpolation were both used in this model to handle axial displacement and deflection respectively. Nath et al. [192] proposed a ZZ theory for investigating the behavior of a multilayered FG cylindrical shell and rectangular plate under static loading and free vibration. To approximate the in-plane displacements, linear LW and cubic global terms were used. In his ZZ theory, Hamilton's principle was utilized to derive the governing equations. Natarajan et al. [193] investigated the flexural and free vibrational behavior of FG-SPs by means of a higher-order ZZ shear flexible element, QUAD-8. To study the bending of FG plates, Garg et al. [194] developed a higher-order ZZ theory based on which the transverse shear and transverse normal stresses are continuous at interlaminar spaces, and the transverse shear stresses vanish at the bounding surfaces of the laminate. Neves et al. [195] presented a theory for the static analysis of FG-SPs by modifying the MZZF. The theory included a hyperbolic sine term for in-plane displacement expansion and a quadratic transverse displacement evolution term to account for thickness-wise deformation and stretching effect.

In ZZ modeling approaches, ZZ function enhances the global responses of the base ESL model and determines the accuracy of predictions [196]. Di Sciuva's [99] and Murakami's ZZ [104] functions are two major ZZ functions which have been utilized either directly or as the basis for additional ZZ theories for analyzing FG structures. In terms of accuracy, Gherlone [153] and Iurlaro [197] found that Di Sciuva's ZZ function surpassed MZZF. The RZT, which was created from Di Sciuva's ZZ theory has recently been used in several investigations of FG laminated structures and composites while representing the same level of accuracy as TSDT [198]. As well as conventional structures, FG/VSCL structures can be analyzed using RZT. Thus, the RZT can deliver reliable results while maximizing computational efficiency. The next section will go over the RZT and the studies conducted on modeling of VSCL and FG structures by this theory.

1.5.3 The RZT and the VSCL and FG composites' modeling

The RZT formulation [22,23], as briefly discussed, was initially developed for analyzing laminates with straight fibers with CS. However, the theory has been used in different studies to simulate the behavior of the constant/variable-stiffness composite laminates as well as FG materials. Having seven kinematic variables, RZT defines unique ZZ functions and thickness-wise slopes for the in-plane displacements by using the differences of transverse shear stiffness of the plies and the laminate's average rigidity [6,28,89,94,199]. Numerous studies have shown that for a large range of span-to-thickness ratios, RZT predicts stress and strain states as accurately as LW and exact solutions for laminates with highly heterogenous materials, resulting in the transverse shear flexibility between the layers, with low computational complexity [22–28]. Furthermore, the RZT does not require the enforcement of transverse shear stress continuity along the thickness of the laminate. This indeed increases the accuracy of results and allows for the use of C^0-continuous representation of the in-plane displacements [22]. Therefore, the elements developed based on RZT, due to the implementation of C^0-continuous formulation, provide appropriate estimations of in-plane displacements without shear-locking and with a compromise between the prediction capability and computational cost [200,201]. For instance, with constraining the first and second shear strains to be constant on the edges of the element, Versino et al. [89] developed a three-node triangle RZT element and showcased the best predictive capability and fast convergence of his element for a diverse set of span-to-thickness ratios and heterogenous laminates. This study was later improved by Wimmer et al. [202] who applied and edge-based smoothed element technique to improve convergence rate of Versino's three-node triangle RZT element for the stresses for thin/thick plates with regular/irregular meshes. The effectiveness of RZT's linear analysis has been verified for CSCLs in many previous studies. However, unlike UD fiber-reinforced composite structures, relatively less effort has paid to capturing the 3D stress fields in VSCLs [152] and/or FG laminated structures based on RZT.

In recent years, the utilization of the RZT method has attracted the attention of researchers for simulating the behavior of curvilinear fiber-reinforced composite laminates. To give an example, for analyzing and optimizing composite SPs with soft-core and straight/curvilinear fiber-reinforced skins, an RZT-based shell element was presented in ref. [203] and shown that curvilinear fiber reinforcement improved the laminates performance. Patni et al. [152] proposed an approach relying on UF-SLE by employing MZZF and the RZT function to predict true stress fields in structural analysis of composites with curvilinear fibers. According to his study, the results obtained from the UF-RZT formulation were more accurate than other ESL approaches for examined cases. Additionally, Hasim et al. [6] proposed an Iso-geometric formulation based on RZT to perform static analysis of the laminates and sandwich panels with curvilinear fibers.

As for the FG laminated structures, Farhatnia et al.'s [204] study is considered as one of the pioneer studies on bending and buckling modeling of FG material metal/ceramic thick beams using the RZT. In another study, an analytical solution was presented for vibration analysis of cantilevered FG sandwich beams on the basis of RZT [205]. The model used infinite sublayers to model the material gradient in the FG face layers. Di Sciuva et al. [206] used the RZT to study the bending and free vibration of SPs made of FG materials and found that, despite its simplicity, RZT predictions of displacements, stresses, and frequencies outperform those of FSDT and TSDT. In a similar study, Iurlaro et al. [198] extended the RZT to laminated FG material plates by eliminating material property discontinuities, allowing the new model to predict transverse shear stresses in FG material laminated structures. According to his study, under various boundary and load conditions, the RZT results for bending and free vibration of SPs with FG material layers are more accurate than traditional FSDT and TSDT reference solutions. Dorduncu [207] combined RZT and the PDDO to develop a non-local model to investigate the static bending behavior of FG plates. Dorduncu [208] also proposed a nonlocal beam model based on RZT to analyze adhesively bonded graded modulus beams. In his study, Peridynamics Least Square Minimization (PDLSM) was successfully used to calculate accurate RZT stresses.

1.6 Summary

To summarize, the modeling techniques of FG materials (i.e., core, face sheet, plate) and VSCLs mainly include 3D elasticity solutions [156,174,209,210], and advanced computational techniques such as meshless [159,161,162,164,207,211–215] or mesh-dependent (i.e., based on LW [93–98] or ESL theories [85–92,109], ZZ theories [129,131,136,194], UF [137,140]) methods. RZT by accounting to the ZZ effect, provides accurate approximations of complex deformations and state of stress fields of CS/VS composites and SPs with isotropic/FG layers, and requires less calculation effort than the LW, HSDTS, and 3D theories. Thus, it meets the requirement of VSCL/FG design in terms of the trade-off between the accuracy and computational costs and can be reliably used as fast and robust analysis to in design platforms of such structures [203].

1.7 Outline

Keeping the objective of the current research in mind, this thesis is structured in logical sequences. The first part of this study in the second chapter focuses on enhancing RZT formulation for composite and sandwich structures with curvilinear fiber reinforcements and FG layers. This model is adapted to a 3-node triangle RZT element to predict the linear behavior of composites for the VS/FG composites as well as SPs. A stress recovery formulation is also provided to accurately capture the transverse shear stresses between adjacent piles continuously. By fulfilling these objectives, an efficient and reliable modeling RZT-based approach to address the challenges of accurate modeling of VS/FG composites and SPs is provided.

The third chapter of this study delves into the numerical analysis of composite structures with curvilinear fibers using the proposed RZT3C formulation. It is shown in chapter that the proper selection of the curvilinear fiber path in the layers plays a critical role in tailoring the strains and stresses to be desirable within the laminate domain. Also, the comparison of the CPU run-time is provided to show that the RZT3C element is more computationally efficient than solid elements and other elements with higher degree of freedom. Therefore, due to its efficiency and accuracy, the RZT3C formulation can be an effective tool for optimizing composite structures with curvilinear fibers.

The fourth chapter of this investigation showcases the potential of the enhanced RZT3C formulation in accurately simulating FG material systems that feature curvilinear fiber reinforcements. The numerical solutions are provided and compared with literature methods and 3D FEM ones for various geometries, boundary conditions, lamination sequences, materials, CG profiles for the through-the-thickness variation of the FG material, and various UD and curvilinear fiber paths. It is shown that the RZT3C approach well-captures the thickness-wise distribution of the strains/stresses for these structures. Therefore, the enhanced RZT3C formulation can serve to accurately tailor the SPs with VS face sheets and FG cores.

Finally, the last part of this study summarizes and highlights the novelty of the contribution of this work and concludes the findings in chapter five.

2 REFINED ZIGZAG THEORY FOR LAMINATES WITH CURVILINEAR FIBER AND FUNCTIONALLY GRADED MATERIALS

2.1 Motivation

As discussed in the previous chapter, the modeling approaches without including the ZZ functions are not suitable for predicting the mechanical behavior of VSCLs and FG layered structures because of their inaccuracy and/or computational cost. The RZT was proposed to conserve the accuracy in predicting the mechanical response of the laminated structures and composites efficiently. This chapter follows two objectives.

The first objective focuses on reformulating the RZT for composites and sandwich structures that contain curvilinear fiber reinforcements in their plies. In these structures, the fiber orientation angle changes in the in-plane coordinates. Therefore, as the novel part of this study, the RZT displacement-strain relations are adopted and readjusted to incorporate the derivatives of ZZ functions with respect to spatial coordinates to reflect the effect of varying fiber angles in linear bending analysis of VSCLs. To develop the FE model, a three-node triangle non-shear locking RZT element (RZT3C) is implemented for the first time in literature in the proposed formulation to predict the displacements and stresses in the plies of VSCLs with minimal computational cost and acceptable accuracy. This is owing to the use of RZT formulation with constant number of kinematics as an ESL theory and the selected element which has the lowest possible node number. Therefore, the model is ideal for the optimization of fiber orientations. Moreover, to ensure the continuity of the transverse shear stress between the adjacent piles, the stress recovery formulation is presented. This posteriori procedure incorporates the in-plane stresses obtained from the proposed formulation in Cauchy's equilibrium equations.

In addition, in response to the growing interest in advanced FG materials, the model is expanded to include FG layers in the presence of curvilinear fibers in multilayered sandwich and composite plates for the first time in the literature. Therefore, the second objective involves enhancing the RZT3C formulation for curvilinear FRCs to accommodate the continuous thickness-wise variation of material for the FG layers. In the enhanced model, the terms for the reduced transformed stiffness, and average transverse shear rigidity depend on the thickness coordinate of the FG material layer(s) resulting in nonlinear variation of piecewise ZZ functions. The successful accomplishment of both objectives in this study results in the development of an ESL

RZT-based formulation that significantly contributes to understanding and modeling of composites and sandwich structures which include both curvilinear fiber-reinforced and FG layers.

2.2 RZT for laminates with curvilinear fibers.

RZT provides highly accurate static and dynamic response of thin and thick laminated structures by utilizing piecewise ZZ functions, $\phi_i^{(k)}$. These functions are incorporated into the displacement fields vary linearly through the laminate's thickness and satisfy all the boundary conditions [22,24,25]. Therefore, in this section, mathematical formulation of original RZT will be reformulated for structural analysis of laminated panels and sandwich structures with curvilinear fibers.

2.2.1 Zigzag kinematics for the curvilinear fiber reinforced laminates

In Fig. 2-1, a laminated plate is depicted with a total thickness of $2h$ and N orthotropic layers reinforced with curvilinear fibers wherein the superscript k denotes the $k^{(th)}$ ply. An orthogonal reference coordinate system (x_1, x_2, z) with the origin of $(0,0,0)$ is located at centroid of the plate. The in-plane coordinates are defined as $\mathbf{x} = (x_1, x_2)$, and z axis represents the through-the-thickness coordinate, $-h \le z \le h$. As depicted in Fig. 2-1, the plate is subjected to normal pressure q whereas it is fully constrained for any rigid body motion.

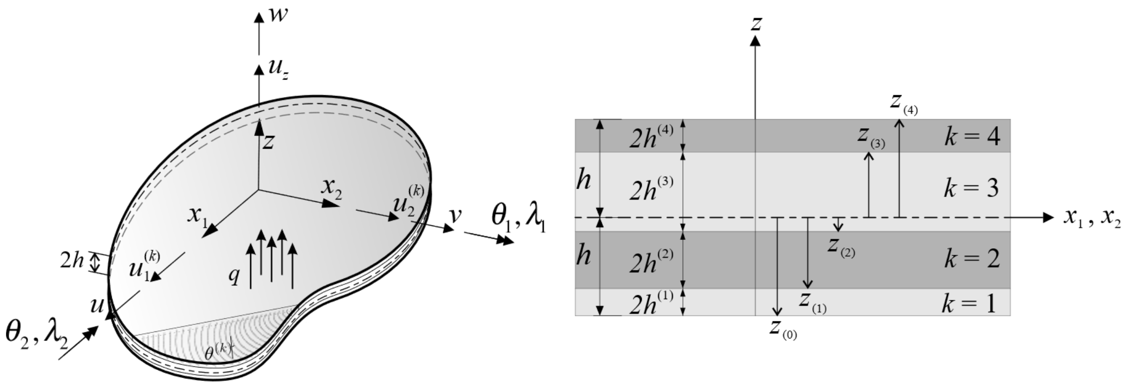

Fig. 2-1 The kinematics of curvilinear fiber reinforced RZT plate and layer notation for a four-layer laminate.

The displacement vector components of a material point in curvilinear fiber reinforced laminate can be defined as the same as the original RZT theory [22]:

$$u_1^{(k)}(\mathbf{x},z) = u(\mathbf{x}) + z\theta_1(\mathbf{x}) + \phi_1^{(k)}(\mathbf{x},z)\lambda_1(\mathbf{x}) \tag{2.1}$$

$$u_2^{(k)}(\mathbf{x},z) = v(\mathbf{x}) + z\theta_2(\mathbf{x}) + \phi_2^{(k)}(\mathbf{x},z)\lambda_2(\mathbf{x}) \tag{2.2}$$

$$u_z(\mathbf{x},z) = w(\mathbf{x}) \tag{2.3}$$

where the RZT kinematic variables $u = u(\mathbf{x})$ and $v = v(\mathbf{x})$ indicate the constant uniform in-plane translations along with positive directions of x_1 and x_2 axes respectively. Moreover, the transverse deflection, $u_z(\mathbf{x},z) = w(\mathbf{x})$ is constant through the thickness of the laminate. In addition, the $\theta_1(\mathbf{x})$ and $\theta_2(\mathbf{x})$ variables represent average bending rotations of RZT and are defined in accordance with positive directions shown in Fig. 2-1. The contribution of the bending rotations changes linearly through the thickness of the laminate as given in Eqs.(2.1)-(2.2). The amplitudes of the ZZ rotations are denoted by $\lambda_i \equiv \lambda_i(\mathbf{x}) \quad (i = 1,2)$, which are coupled with ZZ functions to account for through the thickness ZZ distortions of the cross-sections. The ZZ functions, $\phi_i^{(k)} (i = 1,2)$, vary linearly along the thickness coordinate of individual plies. Hence, the seven RZT kinematic variables can be written more compactly as $\mathbf{u} = [u\ v\ w\ \theta_1\ \theta_2\ \lambda_1\ \lambda_2]^T$. The variation of the ZZ functions can be expressed as [28]:

$$\phi_i^{(k)} = zb_i^{(k)} + a_i^{(k)} \quad (i = 1,2) \tag{2.4}$$

$$b_i^{(k)}(\mathbf{x}) \equiv \phi_{i,z}^{(k)} = \frac{G_i(\mathbf{x})}{\bar{Q}_{ii}^{(k)}(\mathbf{x})} - 1 \ (i = 1,2;\ k = \ldots, N) \tag{2.5}$$

$$\begin{aligned} a_i^{(k)}(\mathbf{x}) &= b_i^{(k)}(\mathbf{x})h \\ &\quad + \sum_{j=2}^{k} 2h^{(j-1)} \left(\frac{G_i(\mathbf{x})}{\bar{Q}_{ii}^{(k)}(\mathbf{x})} - \frac{G_i(\mathbf{x})}{\bar{Q}_{ii}^{(j-1)}(\mathbf{x})} \right) \quad (i = 1,2;\ k = 1,\ldots, N) \end{aligned} \tag{2.6}$$

with

$$G_i(\mathbf{x}) = \left(\frac{1}{h} \sum_{k=1}^{N} \frac{h^{(k)}}{\bar{Q}_{ii}^{(k)}(\mathbf{x})} \right)^{-1} \quad (i = 1,2) \tag{2.7}$$

where $b_i^{(k)}$ is the slope of the ZZ functions along the thickness direction, and $a_i^{(k)}$ enforce the continuity of the ZZ function through the thickness of the laminate. The parameter, $b_i^{(k)}$ is dependent on the transformed transverse shear material moduli of individual plies, $\bar{Q}_{ii}^{(k)}(\mathbf{x})\ (i = 1,2)$ [28] and can be expressed in terms of shear moduli in material axes as:

$$\begin{Bmatrix} \bar{Q}_{11}^{(k)}(\mathbf{x}) \\ \bar{Q}_{22}^{(k)}(\mathbf{x}) \end{Bmatrix} = \begin{Bmatrix} Q_{11}^{(k)} \cos^2 \theta^{(k)}(\mathbf{x}) + Q_{22}^{(k)} \sin^2 \theta^{(k)}(\mathbf{x}) \\ Q_{22}^{(k)} \cos^2 \theta^{(k)}(\mathbf{x}) + Q_{11}^{(k)} \sin^2 \theta^{(k)}(\mathbf{x}) \end{Bmatrix} \tag{2.8}$$

As depicted in Fig. 2-2, the variation of the curvilinear fiber path and its angle, $\theta = \theta(\mathbf{x})$ are dependent on reference surface coordinates, $\mathbf{x} = (x_1, x_2)$ which results in the ZZ functions being a function of all spatial coordinates, $\phi_i^{(k)} \equiv \phi_i^{(k)}(\mathbf{x}, z)$. Hence, the derivatives of ZZ functions with respect to in-plane coordinates are considered in the present study.

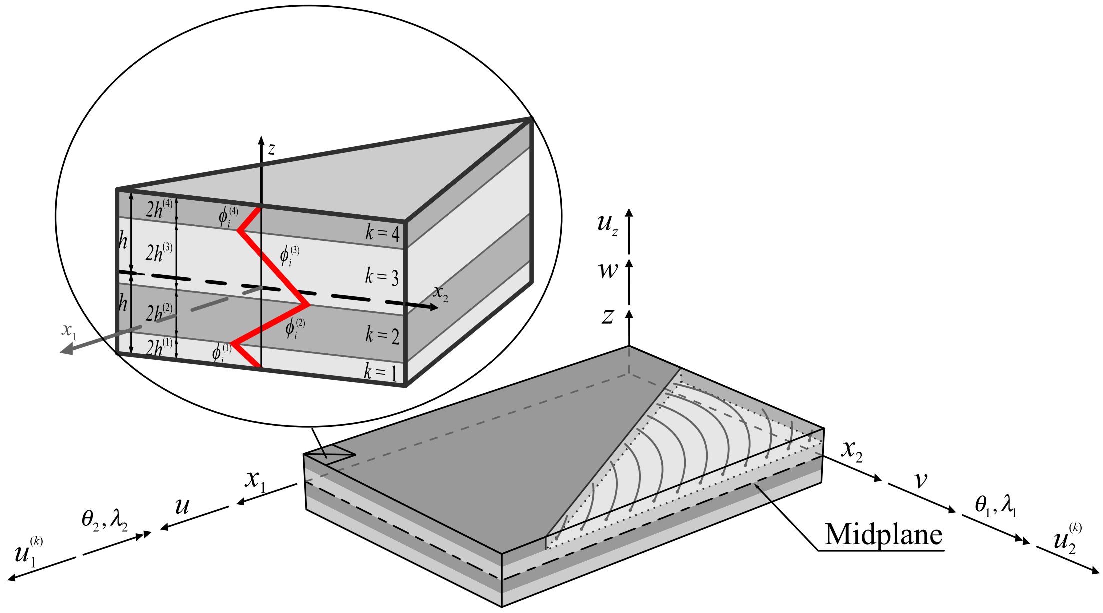

Fig. 2-2 The linear variation of the RZT ZZ function along the thickness of the rectangular laminate with curvilinear fiber path.

2.2.2 Constitutive relations for the curvilinear fiber reinforced laminates

The linear strain-displacement relations are given in Eqs.(2.9)-(2.18). By examining Eqs.(2.9), (2.15), (2.16), and (2.18), the contributions of the ZZ functions' spatial derivatives to in-plane and transverse shear strain fields result in a different form of strain definition than that of the original RZT [23–28].

$$\boldsymbol{\varepsilon}^{(k)} = \begin{bmatrix} \varepsilon_{11}^{(k)} & \varepsilon_{22}^{(k)} & \gamma_{12}^{(k)} \end{bmatrix}^T = \begin{bmatrix} u_{1,1}^{(k)} & u_{2,2}^{(k)} & u_{1,2}^{(k)} + u_{2,1}^{(k)} \end{bmatrix}^T \equiv \boldsymbol{\rho} + z\boldsymbol{\kappa} + \boldsymbol{\Lambda}_{\phi}^{(k)}\boldsymbol{\mu} + \boldsymbol{\Lambda}_{\phi\eta}^{(k)}\boldsymbol{\eta} \tag{2.9}$$

$$\boldsymbol{\rho} = \begin{bmatrix} u_{,1} & v_{,2} & u_{,2} + v_{,1} \end{bmatrix}^T \tag{2.10}$$

$$\boldsymbol{\kappa} = \begin{bmatrix} \theta_{1,1} & \theta_{2,2} & \theta_{1,2} + \theta_{2,1} \end{bmatrix}^T \tag{2.11}$$

$$\boldsymbol{\mu} = \begin{bmatrix} \lambda_{1,1} & \lambda_{2,2} & \lambda_{1,2} & \lambda_{2,1} \end{bmatrix}^T \tag{2.12}$$

$$\boldsymbol{\eta} = \begin{bmatrix} \lambda_1 & \lambda_2 \end{bmatrix}^T \tag{2.13}$$

$$\boldsymbol{\Lambda}_{\phi}^{(k)} = \begin{bmatrix} \phi_1^{(k)} & 0 & 0 & 0 \\ 0 & \phi_2^{(k)} & 0 & 0 \\ 0 & 0 & \phi_1^{(k)} & \phi_2^{(k)} \end{bmatrix} \tag{2.14}$$

$$\boldsymbol{\Lambda}_{\phi\eta}^{(k)} = \begin{bmatrix} \phi_{1,1}^{(k)} & 0 \\ 0 & \phi_{2,2}^{(k)} \\ \phi_{1,2}^{(k)} & \phi_{2,1}^{(k)} \end{bmatrix} \tag{2.15}$$

The vectors $\boldsymbol{\rho}, \boldsymbol{\kappa}$, and $\boldsymbol{\mu}$ include membrane, bending, and ZZ strain measures, respectively. Additionally, $\boldsymbol{\eta}$ stands for the vector of ZZ function amplitudes. In a similar manner, the transverse-shear strain components can be defined as:

$$\boldsymbol{\gamma}^{(k)} = \begin{bmatrix} \gamma_{1z}^{(k)} & \gamma_{2z}^{(k)} \end{bmatrix}^T \equiv \begin{bmatrix} u_{1,z}^{(k)} + u_{z,1} & u_{2,z}^{(k)} + u_{z,2} \end{bmatrix}^T = \boldsymbol{\gamma} + \boldsymbol{\Lambda}_{\eta}^{(k)} \boldsymbol{\eta} \tag{2.16}$$

where $\boldsymbol{\gamma}$ consists of the components of the FSDT shear angles defined as:

$$\boldsymbol{\gamma} \equiv \begin{bmatrix} \gamma_1 & \gamma_2 \end{bmatrix}^T \equiv \begin{bmatrix} w_{,1} + \theta_1 & w_{,2} + \theta_2 \end{bmatrix}^T \tag{2.17}$$

with

$$\boldsymbol{\Lambda}_{\eta}^{(k)} = \begin{bmatrix} b_1^{(k)} & 0 \\ 0 & b_2^{(k)} \end{bmatrix} \tag{2.18}$$

To express the stress field, the 3D constitutive relations can be derived according to the plane stress reduced form of Hooke’s law as:

$$\begin{bmatrix} \boldsymbol{\sigma}^{(k)} \\ \boldsymbol{\tau}^{(k)} \end{bmatrix} = \begin{bmatrix} \mathbf{C}^{(k)} & \mathbf{0} \\ \mathbf{0} & \mathbf{Q}^{(k)} \end{bmatrix} \begin{bmatrix} \boldsymbol{\varepsilon}^{(k)} \\ \boldsymbol{\gamma}^{(k)} \end{bmatrix} \tag{2.19}$$

where $\boldsymbol{\sigma}^{(k)}$ and $\boldsymbol{\tau}^{(k)}$ represent the vectors of in-plane and transverse-shear stresses. $\mathbf{C}^{(k)}$ and $\mathbf{Q}^{(k)}$ are reduced transformed stiffness matrices referred to the (x_1, x_2, z) coordinate system, which are related to the elastic coefficients in the material coordinates [72]. The explicit form of in-plane normal and shear stress vectors as well as transverse stresses are shown below. Also, The terms $C_{ij}^{(k)}$ $(i, j = 1, 2, 6)$ and Q_{mn} $(m, n = 1, 2)$ in $\mathbf{C}^{(k)}$ and $\mathbf{Q}^{(k)}$ matrices are the ply-level reduced transformed stiffness components which are obtained with passive transformation of the coordinate system from fiber reference $(1,2,3)$ to global reference coordinates $(\mathbf{x},z)$.

$$\boldsymbol{\sigma}^{(k)}=\begin{bmatrix}\sigma_{11}^{(k)} & \sigma_{22}^{(k)} & \tau_{12}^{(k)}\end{bmatrix},\ \boldsymbol{\tau}^{(k)}\equiv\begin{bmatrix}\tau_{1z}^{(k)} & \tau_{2z}^{(k)}\end{bmatrix} \tag{2.20}$$

$$\mathbf{C}^{(k)}=\begin{bmatrix}C_{11} & C_{12} & C_{16}\\ C_{12} & C_{22} & C_{26}\\ C_{16} & C_{26} & C_{66}\end{bmatrix}^{(k)},\quad \mathbf{Q}^{(k)}=\begin{bmatrix}Q_{11} & Q_{12}\\ Q_{12} & Q_{22}\end{bmatrix}^{(k)} \tag{2.21}$$

2.2.3 The principle of virtual work

According to the principle of virtual displacements, the actual equilibrium configuration makes the total virtual work done equal to zero and can be expressed as:

$$\delta U-\delta V=0 \tag{2.22}$$

in which δV represents the virtual work done by the external distributed forces, $q_0(x_1,x_2)$ in moving through the virtual displacement, δw and expressed as:

$$\delta U=\int_V(\delta(\boldsymbol{\varepsilon}^{(k)})^T\boldsymbol{\sigma}^{(k)}+\delta(\boldsymbol{\gamma}^{(k)})^T\boldsymbol{\tau}^{(k)})dV \tag{2.23}$$

$$\delta V=\int_A\delta w q_0 dA \tag{2.24}$$

The variation of internal strain energy, δU in Eq.(2.22) can be obtained by replacing Eqs.(2.9)-(2.15) and Eqs.(2.16)-(2.18) into Eq.(2.23), and integrating through the thickness that results in:

$$\delta U=\int_A(\delta\boldsymbol{\rho}^T\mathbf{P}+\delta\boldsymbol{\kappa}^T\mathbf{M}^b+\delta\boldsymbol{\mu}^T\mathbf{M}^\phi+\delta\boldsymbol{\eta}^T(\mathbf{S}^\phi+\mathbf{S}_z^\phi)+\delta\boldsymbol{\gamma}^T\mathbf{S}_z)dA \tag{2.25}$$

where the stress resultants $(\mathbf{P},\mathbf{M}^b,\mathbf{M}^\phi,\mathbf{S}^\phi,\mathbf{S}_z^\phi,\mathbf{S}_z)$ are defined as:

$$\mathbf{P}\equiv\begin{bmatrix}P_{11} & P_{22} & P_{12}\end{bmatrix}^T=\sum_{k=1}^{N_L}\int_{z_k}^{z_{k+1}}\boldsymbol{\sigma}^{(k)}dz \tag{2.26}$$

$$\mathbf{M}^b\equiv\begin{bmatrix}M_{11}^b & M_{22}^b & M_{12}^b\end{bmatrix}^T=\sum_{k=1}^{N_L}\int_{z_k}^{z_{k+1}}z\boldsymbol{\sigma}^{(k)}dz \tag{2.27}$$

$$\mathbf{M}^\phi\equiv\begin{bmatrix}M_{11}^\phi & M_{22}^\phi & M_{12}^\phi & M_{21}^\phi\end{bmatrix}^T=\sum_{k=1}^{N_L}\int_{z_k}^{z_{k+1}}(\boldsymbol{\Lambda}_\phi^{(k)})^T\boldsymbol{\sigma}^{(k)}dz \tag{2.28}$$

$$\mathbf{S}^{\phi} \equiv \left[S_{11}^{\phi} \quad S_{22}^{\phi} \right]^{T} = \sum_{k=1}^{N_L} \int_{z_k}^{z_{k+1}} (\mathbf{\Lambda}_{\phi\eta}^{(k)})^{T} \boldsymbol{\sigma}^{(k)} dz \tag{2.29}$$

$$\mathbf{S}_{z} \equiv \left[S_{1z} \quad S_{2z} \right]^{T} = \sum_{k=1}^{N_L} \int_{z_k}^{z_{k+1}} \boldsymbol{\tau}^{(k)} dz \tag{2.30}$$

$$\mathbf{S}_{z}^{\phi} \equiv \left[S_{1z}^{\phi} \quad S_{2z}^{\phi} \right]^{T} = \sum_{k=1}^{N_L} \int_{z_k}^{z_{k+1}} (\mathbf{\Lambda}_{\eta}^{(k)})^{T} \boldsymbol{\tau}^{(k)} dz \tag{2.31}$$

$\mathbf{D}$ is the symmetric stiffness matrix comprised of the sub-stiffness matrices of various loadings of the whole laminate, and $\boldsymbol{\omega}$ is the vector consisting of the RZT strain measures. The components of the stiffness matrices can be computed in a similar way to the Ref. [22] as detailed below.

$$\begin{Bmatrix} \mathbf{P} \\ \mathbf{M}^{b} \\ \mathbf{M}^{\phi} \\ \mathbf{S}_{\mathbf{z}} \\ \mathbf{S}^{\phi} + \mathbf{S}_{\mathbf{z}}^{\phi} \end{Bmatrix} = \begin{bmatrix} \mathbf{A} & \boldsymbol{\beta} & \boldsymbol{\beta}_{\phi} & \mathbf{0} & \boldsymbol{\beta}_{\phi\eta} \\ \boldsymbol{\beta}^{T} & \mathbf{\Delta}_{\kappa} & \mathbf{\Delta}_{\kappa\mu} & \mathbf{0} & \mathbf{\Delta}_{\kappa\eta} \\ \boldsymbol{\beta}_{\phi}^{T} & \mathbf{\Delta}_{\kappa\mu}^{T} & \mathbf{\Delta}_{\mu} & \mathbf{0} & \mathbf{\Delta}_{\mu\eta} \\ \mathbf{0} & \mathbf{0} & \mathbf{0} & \mathbf{\Gamma}_{\gamma} & \mathbf{\Gamma}_{\gamma\eta} \\ \boldsymbol{\beta}_{\phi\eta}^{T} & \mathbf{\Delta}_{\kappa\eta}^{T} & \mathbf{\Delta}_{\mu\eta}^{T} & \mathbf{\Gamma}_{\gamma\eta}^{T} & \mathbf{\Delta}_{\eta} + \mathbf{\Gamma}_{\eta} \end{bmatrix} \begin{Bmatrix} \boldsymbol{\rho} \\ \boldsymbol{\kappa} \\ \boldsymbol{\mu} \\ \boldsymbol{\gamma} \\ \boldsymbol{\eta} \end{Bmatrix} = \mathbf{D}\boldsymbol{\omega} \tag{2.32}$$

with

$$\mathbf{A} = \int_{-h}^{+h} \mathbf{C}^{(k)} dz, \ \boldsymbol{\beta} = \int_{-h}^{+h} \mathbf{C}^{(k)} z dz \tag{2.33}$$

$$\boldsymbol{\beta}_{\phi} = \int_{-h}^{+h} \mathbf{C}^{(k)} \mathbf{\Lambda}_{\phi}^{(k)} dz, \ \boldsymbol{\beta}_{\phi\eta} = \int_{-h}^{+h} \mathbf{C}^{(k)} \mathbf{\Lambda}_{\phi\eta}^{(k)} dz \tag{2.34}$$

$$\mathbf{\Delta}_{\kappa} = \int_{-h}^{+h} \mathbf{C}^{(k)} z^{2} dz, \ \mathbf{\Delta}_{\kappa\mu} = \int_{-h}^{+h} \mathbf{C}^{(k)} \mathbf{\Lambda}_{\phi}^{(k)} z dz \tag{2.35}$$

$$\mathbf{\Delta}_{\mu} = \int_{-h}^{+h} \mathbf{\Lambda}_{\phi}^{(k)^{T}} \mathbf{C}^{(k)} \mathbf{\Lambda}_{\phi}^{(k)} dz, \ \mathbf{\Delta}_{\kappa\eta} = \int_{-h}^{+h} z \mathbf{C}^{(k)} \mathbf{\Lambda}_{\phi\eta}^{(k)} dz \tag{2.36}$$

$$\mathbf{\Delta}_{\mu\eta} = \int_{-h}^{+h} \mathbf{\Lambda}_{\phi}^{(k)^{T}} \mathbf{C}^{(k)} \mathbf{\Lambda}_{\phi\eta}^{(k)} dz \text{ .,} \ \mathbf{\Delta}_{\eta} = \int_{-h}^{+h} \mathbf{\Lambda}_{\phi\eta}^{(k)^{T}} \mathbf{C}^{(k)} \mathbf{\Lambda}_{\phi\eta}^{(k)} dz \tag{2.37}$$

$$\mathbf{\Gamma}_{\gamma} = \int_{-h}^{+h} \mathbf{Q}^{(k)} dz, \ \mathbf{\Gamma}_{\gamma\eta} = \int_{-h}^{+h} \mathbf{Q}^{(k)} \mathbf{\Lambda}_{\eta}^{(k)} dz, \ \mathbf{\Gamma}_{\eta} = \int_{-h}^{+h} \mathbf{\Lambda}_{\eta}^{(k)T} \mathbf{Q}^{(k)} \mathbf{\Lambda}_{\eta}^{(k)} dz \tag{2.38}$$

By replacing the strain measures and ZZ amplitudes of Eqs.(2.10)-(2.13) with shear angles, Eq.(2.17) into Eq.(2.23), as the internal strain energy, and using the expression for the external work in Eq.(2.24), the equilibrium for the total virtual work, Eq.(2.22) can be obtained in its expanded form. The Euler-Lagrange equations and related Dirichlet

(Γ_D) or Neumann (Γ_σ) boundary conditions are obtained by taking integral by parts of the associated virtual work statement, Eqs.(2.22)-(2.25) to relieve the virtual generalized displacements $(\delta u, \delta v, \delta w, \delta\theta_1, \delta\theta_2, \delta\lambda_1, \delta\lambda_2)$ of any differentiation, which results in:

$$\begin{aligned}
&\delta u: \quad P_{11,1} + P_{12,2} = 0 \\
&\delta v: \quad P_{12,1} + P_{22,2} = 0 \\
&\delta w: \quad S_{1z,1} + S_{2z,2} + q_0 = 0 \\
&\delta\theta_1: \quad M^b_{11,1} + M^b_{12,2} - S_{1z} = 0 \\
&\delta\theta_2: \quad M^b_{12,1} + M^b_{2,2} - S_{2z} = 0 \\
&\delta\lambda_1: \quad M^\varphi_{11,1} + M^\varphi_{12,2} - S^\varphi_{1z} - S^\phi_1 = 0 \\
&\delta\lambda_2: \quad M^\varphi_{21,1} + M^\varphi_{2,2} - S^\varphi_{2z} - S^\phi_2 = 0
\end{aligned} \tag{2.39}$$

with

$$\chi = \bar{\chi}(\chi = u, v, w, \theta_1, \theta_2, \lambda_1, \lambda_2) \text{ on } \Gamma_D \tag{2.40}$$

$$\begin{bmatrix} P_{11} & P_{12} \\ P_{12} & P_{22} \\ S_{1z} & S_{2z} \end{bmatrix} \begin{Bmatrix} n_1 \\ n_2 \end{Bmatrix} = \begin{Bmatrix} P_{1z} \\ P_{2z} \\ S_{zn} \end{Bmatrix} \tag{2.41}$$

$$\begin{bmatrix} M^b_{11} & M^b_{12} \\ M^b_{12} & M^b_{22} \\ M^\phi_{11} & M^\phi_{12} \\ M^\phi_{21} & M^\phi_{22} \end{bmatrix} \begin{Bmatrix} n_1 \\ n_2 \end{Bmatrix} = \begin{Bmatrix} M^b_{1n} \\ M^b_{2n} \\ M^\phi_{1n} \\ M^\phi_{2n} \end{Bmatrix} \text{ on } \Gamma_\sigma \tag{2.42}$$

where the vectors, $\begin{bmatrix} P_{1z} & P_{2z} & S_{zn} \end{bmatrix}$ and $\begin{bmatrix} M^b_{1n} & M^b_{2n} & M^\phi_{1n} & M^\phi_{2n} \end{bmatrix}$ are representing the forces and moments acting on the laminate, and $\begin{bmatrix} n_1 & n_2 \end{bmatrix} \equiv \begin{bmatrix} \cos(x_1, n) & \cos(x_2, n) \end{bmatrix}$ are the direction cosines of the normal outward vector on the periphery edge of the mid-plane, (Fig. 2-1).

2.3 The three-node shear-locking free triangular RZT element (RZT3C)

To solve the RZT governing equations, FE method is employed using a locking-free triangular element. Shear locking is the stiffer behavior of linear elements due to the inappropriate capturing of non-disappearing transverse shear strains while exposed to out-of-plane bending. Among methods to avoid shear locking some can be listed as the reduced and selective integration techniques [216–218], the constrained assumed strain field [219–221], the discrete Kirchhoff technique [219,222–225], the discrete shear gap method, DSG, [226], strain-based FE formulation [227], the independent interpolation of the shear strains to separate the bending and shear deformation energy [228–234]. Additionally, the utilization of anisoparametric interpolation with full integration which does not remove the constraints over the strain energy terms, which is also used here, is another effective method that prevents shear locking [235–239]. To overcome the shear-locking of the laminated composite plate element with curvilinear fibers, an anisoparametric three-node constrained RZT plate element with seven unknown kinematic variables has been implemented. The advantageous parts of picking the three-node triangle RZT element can be listed as: availability of modelling sophisticated structures, shear-locking free and ease of implementation of the constrained RZT3C element in comparison with the unconstrained element. The latter one is due to the compatibility of the adjacent elements in their nodes, all having the same number of displacements DOF. Besides, the eliminated mid-nodes in the selected element enhance computational efficiency. In the appendix of this thesis, the process element mid-node elimination from the six-node triangle element to obtain the RZT3C element and developing its associated linear anisoparametric shape function and strain-displacement matrices is provided.

2.3.1 Implementation of the three-node triangle RZT element

Fig. 2-3 shows the schematic of the implemented triangle RZT element. As can be seen, the local element coordinate system consists of three orthogonal axes (x, y, z) in the centroid of the mid-plane of the element and the element level kinematic variables of RZT can be summarized in the vector form as $\mathbf{u}_i^e \equiv [u_i \; v_i \; w_i \; \theta_{xi} \; \theta_{yi} \; \lambda_{xi} \; \lambda_{yi}]^{\mathrm{T}} \quad (i = 1, 2, 3)$. The linear area-parametric interpolations of the in-plane translations, the bending rotations $\theta_\alpha (\alpha = 1, 2)$, and the amplitude of ZZ rotations $\lambda_\alpha (\alpha = 1, 2)$ can be readily written in a compact matrix representation using a general element shape function matrix $\mathbf{N}^e$ which can be summarized as the following expression [239]:

$$\mathbf{u} = \begin{bmatrix} \mathbf{N}_1^e & \mathbf{N}_2^e & \mathbf{N}_3^e \end{bmatrix} \begin{Bmatrix} \mathbf{u}_1^e \\ \mathbf{u}_2^e \\ \mathbf{u}_3^e \end{Bmatrix} \equiv \mathbf{N}^e \mathbf{u}^e \tag{2.43}$$

Following the replacement of Eq.(2.43) in Eqs.(2.10)-(2.13) and Eq.(2.17), RZT strain measures can be explicitly expressed as:

$$\boldsymbol{\omega} = \begin{bmatrix} \mathbf{B}_1^e & \mathbf{B}_2^e & \mathbf{B}_3^e \end{bmatrix} \begin{Bmatrix} \mathbf{u}_1^e \\ \mathbf{u}_2^e \\ \mathbf{u}_3^e \end{Bmatrix} \equiv \mathbf{B}^e \mathbf{u}^e \tag{2.44}$$

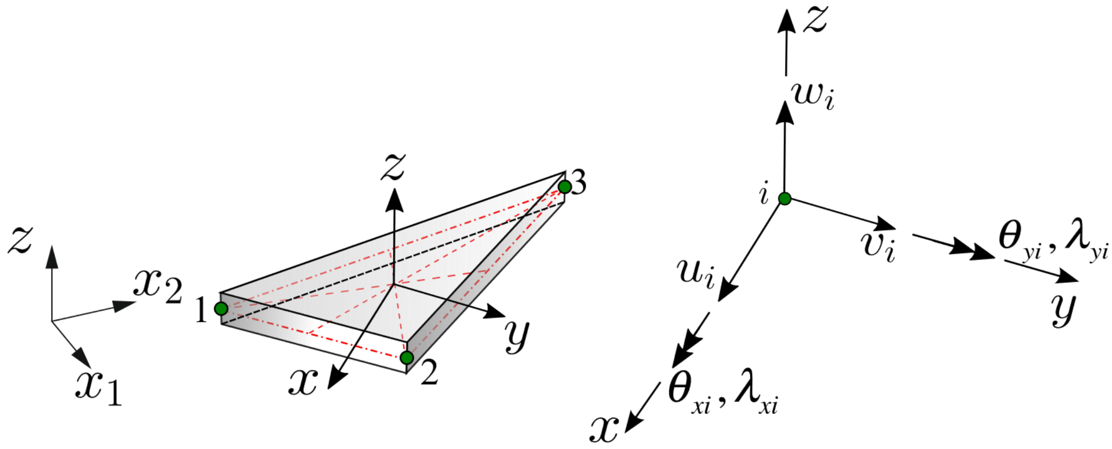

(a) (b)

Fig. 2-3 Three-node triangle RZT element, depicted in the global and local coordinate systems, with the nodal DOF in the local reference system.

where $\mathbf{B}^e$ matrix contains the components of the derivatives of the shape functions which are utilized for relating the strains to displacements. For more comprehensive details, the reader is enticed to refer to the Ref. [89]. To calculate the element stiffness matrix, it is necessary to solve and rewrite the principal of virtual work in Eq.(2.22) for the variation of $\mathbf{u}^e$ respectively. The element-level equilibrium equation from the mentioned substitutions will then take the form as the following:

$$\mathbf{k}^e \mathbf{u}^e = \mathbf{f}^e \tag{2.45}$$

where $\mathbf{k}^e$ is the element stiffness, and can be explicitly shown with the following expression as:

$$\mathbf{k}^e = \int \mathbf{B}^{e^T} \mathbf{D} \mathbf{B}^e dA \tag{2.46}$$

and $\mathbf{f}^e$, the element force vector due to the normal distributed load caused by $q(\boldsymbol{x})$ is defined as:

$$\mathbf{f}^e = \int \left(\mathbf{M}^e\right)^T q_0 dA \tag{2.47}$$

where vector $\mathbf{M}^e$ contains the components of the third row of the shape function matrix $\mathbf{N}^e$ in Eq.(2.43). To predict the overall behavior of the laminate, the assembly of the local stiffnesses and forces to their global matrices are as follows:

$$\Xi = \underset{i=1}{\overset{nel}{\Omega}} \xi^e \quad \left(\Xi = \mathbf{K}, \mathbf{U}, \mathbf{F}; \quad \xi = \mathbf{k}, \mathbf{u}, \mathbf{f} \right) \tag{2.48}$$

where the operator Ω assembles the element-wise stiffness, displacement, and force to their corresponding components of global matrices as the following expression to apply the prescribed boundary conditions for the problem.

$$\mathbf{KU} = \mathbf{F} \tag{2.49}$$

2.4 Stress recovery

RZT provides accurate predictions of the state of strains and stresses in the physical domain. Even though the through the thickness transverse shear stresses predicted in RZT are piecewise constant, they lack the traction continuity for the adjacent laminae due to the inherent displacement-based trait of RZT [6,152]. Therefore, for the sake of precise modeling in this research, the inter-laminar discontinuity problem in transverse shear stresses' distribution with RZT is obtained by integrating in-plane stresses in 3D elasticity Cauchy's equilibrium equations in the thickness direction. For the quasistatic problem without the presence of body forces, the 3D stress equilibrium equations are:

$$\sigma_{ij,j} = 0 \quad (i, j = 1, 2, z) \tag{2.50}$$

The dummy index j represents Einstein's summation convention where differentiation has been performed. At the present study with plane-stress assumption, the in-plane stresses, $\boldsymbol{\sigma}^{(k)}$, are computed from the RZT constitutive relations as in Eq.(2.19). Transverse shear stresses, τ_{1z}, τ_{2z}, however, are computed by taking integration of Cauchy's equilibrium equations along the thickness direction as:

$$\tau_{iz}^{(k)}(\mathbf{x}, z) = C_\alpha{}^{(k)}(\mathbf{x}) - \int_{z_b{}^{(k)}}^{z} \left(\sigma_{i1,1}^{(k)} + \tau_{i2,2}^{(k)} \right) dz \quad (i, \alpha = 1, 2) \tag{2.51}$$

where and $C_\alpha^{(k)}(\mathbf{x})$ are the transverse stresses in $\mathbf{x}$ directions respectively at the bottom of the $k^{(th)}$ lamina. Herein, due to spatial variation of Hooke's coefficients for composite structures with curvilinear fiber path, $C_\alpha{}^{(k)}(\mathbf{x})$ vary spatially and must be calculated separately for every material point over the mid-plane domain by enforcing the transverse shear stress condition at the bounding surfaces of the laminate to be zero.

2.5 The enhancement of the RZT3C formulation to FG materials

This section discusses the enhancement of the RZT formulation presented in the preceding sections of this chapter for the laminates with curvilinear fibers to multi-layered composite plates incorporating FG materials and curvilinear fiber reinforcements in their layers. The enhanced formulation will be used with the three-node plate element formulation to perform static analyses.

2.5.1 Kinematics, and zigzag relations for FG laminates reinforced with curvilinear fibers

Fig. 2-4 depicts a multi-layer plate with a uniform total thickness of $2h$, and N bonded linearly elastic FG material and/or orthotropic curvilinear fiber-reinforced layers. The effective mechanical properties throughout the laminate are distributed both by the FG material and the curvilinear fiber-reinforced layers. As the reference, an orthogonal coordinate system (x_1, x_2, z) is taken at the center of plate's middle reference plane, mid-plane placed on the $\mathbf{x}$-plane, $\mathbf{x} = (x_1, x_2)$. The z axis ranges between $-h$ and h defines the thickness coordinate, and each layer is having constant thickness through the entire plate.

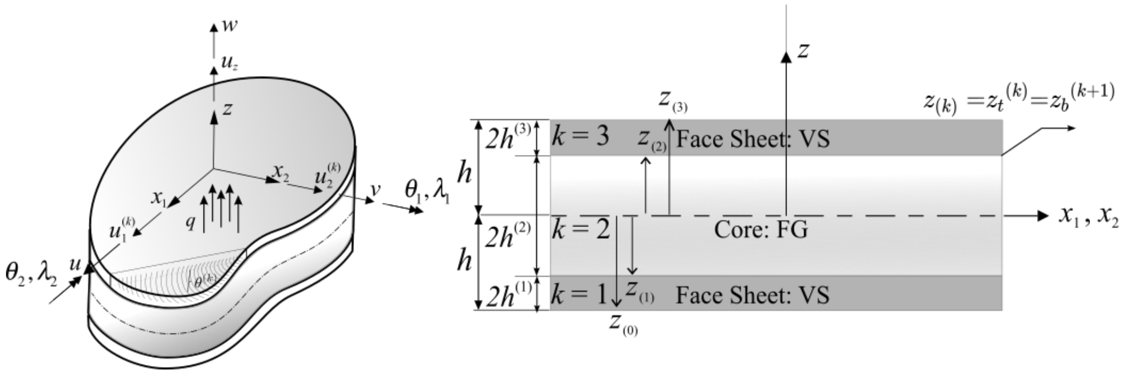

Fig. 2-4 The RZT kinematics and notation for a three-layer laminated SP with an FG material core layer and curvilinear fiber reinforced face sheets (skins).

The superscript k denotes the k^{th} layer, whereas the subscript k denotes the k^{th} interface between the layers k and $(k+1)$. Transverse pressure is applied on the top surface of the plate, and it is constrained on the peripheral edges against rigid body motion (Fig. 2-4). To define the displacement field of a point in the domain of an FG material laminated plate with curvilinear fibers, RZT kinematics are used. Therefore, the displacement vector components are obtained by superimposing the FSDT kinematics as the displacement of the entire laminate and a layer-wise correlation of the planar displacements as the scaled contribution of each single thickness ply, representing the global and local responses, respectively. Thus, the displacement filed can be written as:

$$\mathbf{u}^{(k)}(\mathbf{x},z)=\mathbf{u}_G(\mathbf{x},z)+\mathbf{u}_L^{(k)}(\mathbf{x},z) \tag{2.52}$$

$$\mathbf{u}_G^{(k)}(\mathbf{x},z)=\mathbf{u}(\mathbf{x})+z\boldsymbol{\theta}^{(k)}(\mathbf{x}) \tag{2.53}$$

$$\mathbf{u}(\mathbf{x})=[u(\mathbf{x}) \quad v(\mathbf{x}) \quad w(\mathbf{x})]^T \tag{2.54}$$

$$\mathbf{u}_L^{(k)}(\mathbf{x},z)=\left[\phi_1^{(k)}(\mathbf{x},z)\lambda_1(\mathbf{x}) \quad \phi_2^{(k)}(\mathbf{x},z)\lambda_2(\mathbf{x}) \quad 0\right]^T \tag{2.55}$$

where the uniform constant planar displacements $u(\mathbf{x})$, and $v(\mathbf{x})$ are along the positive x_1 and x_2 directions. $w(\mathbf{x})$ denotes the laminate's transverse deflection, which is constant throughout its thickness.

Furthermore, the components of $\boldsymbol{\theta}^{(k)}(\mathbf{x},z)=\left[\theta_1^{(k)}(\mathbf{x}) \quad \theta_2^{(k)}(\mathbf{x}) \quad 0\right]^T$ are the average bending rotations which are positive as illustrated in Fig. 2-4. The average bending rotations have a continuous linear contribution along the laminate's thickness. Also, the global field of displacement, $\mathbf{u}_G^{(k)}$ has a linear continuous first derivative, with respect to the thickness direction. The local displacement field, $\mathbf{u}_L^{(k)}(\mathbf{x},z)$ accounts for the ZZ cross-sectional distortions by coupling $\phi_i^{(k)}(\mathbf{x},z)\,(i=1,2)$, the ZZ functions, and their amplitudes $\lambda_i \equiv \lambda_i(\mathbf{x})\,(i=1,2)$. The ZZ cross-sectional distortions, added to the planar displacements, are non-linearly continuous through the thickness direction. Nonetheless, their first derivatives show a jumping behavior in the interlaminar space of the attached layers. It is clear that if $\mathbf{u}_L^{(k)}(\mathbf{x},z)$ is set equal to zero, the RZT theory is downgraded to its specific case, FSDT. Thus, the RZT displacement field is characterized by seven kinematic variables for any number of layers and can compactly be written in the form as $\mathbf{u}=[u\ v\ w\ \theta_1\ \theta_2\ \lambda_1\ \lambda_2]^T$. The refined ZZ functions' variation for the k^{th} ply can be defined as:

$$\begin{aligned}\phi_i^{(k)}(\mathbf{x},z)&=\left(z+h\right)\left(\frac{G_i(\mathbf{x},z)}{\bar{\mathrm{Q}}_{ii}^{(k)}(\mathbf{x},z)}-1\right)\\&+\sum_{j=2}^{k}2h^{(j-1)}\left(\frac{G_i(\mathbf{x},z)}{\bar{Q}_{ii}^{(k)}(\mathbf{x},z)}-\frac{G_i(\mathbf{x},z)}{\bar{Q}_{ii}^{(j-1)}(\mathbf{x},z)}\right)\quad(i=1,2;k=1,\ldots,N)\end{aligned} \tag{2.56}$$

where $\bar{Q}_{ii}^{(k)}(\mathbf{x},z)\ (i=1,2)$ denotes the reduced transformed transverse shear stiffnesses of each FG ply, which are also functions of through-the-thickness direction due to the gradation of the material, and they are expressed as the following:

$$\begin{Bmatrix} \bar{Q}_{11}^{(k)}(\mathbf{x},z) \\ \bar{Q}_{22}^{(k)}(\mathbf{x},z) \end{Bmatrix} = \begin{Bmatrix} Q_{11}^{(k)}(z)\cos^2\theta^{(k)}(\mathbf{x}) + Q_{22}^{(k)}(z)\sin^2\theta^{(k)}(\mathbf{x}) \\ Q_{22}^{(k)}(z)\cos^2\theta^{(k)}(\mathbf{x}) + Q_{11}^{(k)}(z)\sin^2\theta^{(k)}(\mathbf{x}) \end{Bmatrix} \tag{2.57}$$

Eq.(2.57) employs the variable $\theta^{(k)}(\mathbf{x})$ to represent the curvilinear fiber angle at a specific location $\mathbf{x}=(x_1,x_2)$ within the corresponding layer, as depicted in Fig. 2-5. Therefore, the transformed transverse shear stiffness terms, $\bar{Q}_{ii}^{(k)}(\mathbf{x},z)\ (i=1,2)$ become dependent on the in-plane coordinates $\mathbf{x}=(x_1,x_2)$ due to the variation of the curved fiber angle across those coordinates. Hence, for the case of the plane-stress condition, the derivates of the ZZ functions should be taken into account with respect to the in-plane coordinates for the definition of strains, unlike the original form of the RZT. Moreover, the $Q_{ii}^{(k)}(z)\ (i=1,2)$ terms show the transverse shear moduli of the k^{th} ply, and their values are continuously being regulated by a grading function in a homogenization model such as power-law and rule of mixture. That is, changes in the volume fraction according to a certain profile of the lead to continuous variations of the elasticity moduli terms through the thickness of FG laminae. As a result of these factors, the ZZ functions become non-linear piecewise functions of all spatial coordinates.

Since the ZZ function values at the plate's bounding faces must be equal to zero, it can be written:

$$\phi_i^{(k)}(\mathbf{x},z) = \phi_i^{(k)}(\mathbf{x},z) = 0\ \left(i=1,2; k=1,N; z=\pm h\right) \tag{2.58}$$

The $G_i(\mathbf{x},z)\left(i=1,2\right)$ terms in Eqs.(2.56) and (2.59) represent the weighted mean transverse shear moduli of the corresponding ply level coefficients, $\bar{\mathrm{Q}}_{ii}^{(k)}(\mathbf{x},z)$. The weighted average shear moduli for the FG material with curvilinear fiber reinforcement similar to the ZZ functions are also functions of all spatial directions. Using a partial thickness-wise continuity condition on transverse shear stresses, the slopes of the ZZ functions are expressed as:

$$b_i^{(k)}(\mathbf{x},z) \equiv \phi_{i,z}^{(k)}(\mathbf{x},z) = \frac{G_i(\mathbf{x},z)}{\bar{\mathrm{Q}}_{ii}^{(k)}(\mathbf{x},z)} - 1\ (i=1,2;\ k=\ldots,\ N) \tag{2.59}$$

For FG material plies, due to the non-linear dependence of the ZZ functions on the thickness-wise direction, z, $b_i^{(k)}(\mathbf{x},z)$ are piecewise functions having non-constant value along the thickness of each individual ply. Based on Eq.(2.58), it can be inferred that the ZZ slopes will also take zero values on the bottom and top surfaces of the laminate, and its thickness-wise integration will take the following form:

$$\int_{-h}^{h} b_i^{(k)}(\mathbf{x},z)dz = 0 \quad (i=1,2) \tag{2.60}$$

Therefore, by replacing Eq.(2.59) in Eq.(2.60), weighted mean transverse shear stiffness is obtained as:

$$G_i(\mathbf{x},z) = \left(\frac{1}{2h} \sum_{k=1}^{N} \int_{z^{(k)}}^{z^{(k+1)}} \frac{dz}{\bar{Q}_{ii}^{(k)}(\mathbf{x},z)} \right)^{-1} \quad (i=1,2) \tag{2.61}$$

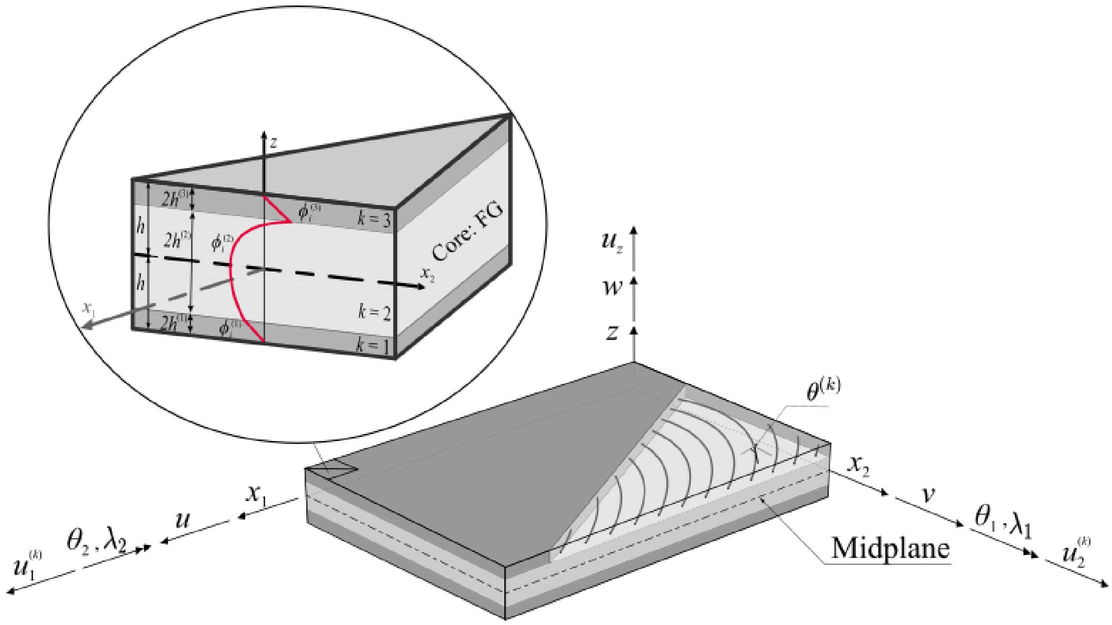

Fig. 2-5 The curvilinear fiber path and the thickness-wise change of the non-linear RZT ZZ function for the FG material laminate.

The derivation procedure, the relations for the strain-displacements, and stresses of the k^{th} FG/orthotropic ply with curvilinear fibers are the same as Eqs.(2.9)-(2.21). Analogously, the relations from the virtual work principle for the stiffness matrix associated with the strain measures as well as the Euler-Lagrange equations, and related Dirichlet or Neumann boundary conditions are the same with Eqs.(2.22)-(2.42). Therefore, for conciseness these equations have not been repeated here. Furthermore, for the discretization of the domain of the FG material composite laminate, the RZT3C element can be implemented in the same as presented previously in this chapter. Herein, the enhanced RZT formulation for the FG material laminates also provides only a general average estimation of the transverse shear stresses and to obtain the components of the stresses continuously the stress recovery procedure has to be applied as presented.

3 IMPLEMENTATION OF SHEAR-LOCKING-FREE TRIANGULAR REFINED ZIGZAG ELEMENT FOR STRUCTURAL ANALYSIS OF MULTILAYERED PLATES WITH CURVILINEAR FIBERS

3.1 Overview

Modeling and analysis of curvilinear FRCs is quite challenging in terms of accuracy and computational cost owing to their VS. In this chapter, the accuracy, and increased capabilities of the developed model in this thesis are verified by conducting comprehensive numerical investigations on various benchmark cases from the literature for curvilinear fiber reinforced laminates with various geometries, lamination sequences, and materials.

The first test case is a three-layered sandwich plate with VS face sheets which had been solved by the higher-order CUF and MZZF, and isogeometric formulations in the literature. In the second test case, as well as the effect of change in curvilinear fiber orientation, the change in span-to thickness ratio has also been investigated for a VS rectangular plate. This test case had been investigated by the higher-order GUF and isogemetric formulations. Additionally, a VS circular plate is selected for investigation of the capability of the proposed formulation in predicting the structural behavior of the non-rectangular geometries. Therefore, the acquired strain and stress results are compared and extensively validated with those of high-fidelity 3-D ANSYS models as well as high-order theories and three-dimensional elasticity solutions available in the literature. The aim of solving these cases with the provided formulations is to demonstrate that properly formulated and implemented RZT can offer correct estimations of displacements, strains, and stress thorough-the-thickness direction of VS composites. Also, it is shown in this chapter that the correct predictions of stresses by the proposed RZT model results in successful stress recovery procedure based on Cauchy's equilibrium equations for the transverse-shear stresses [152].

Moreover, the tabulated data obtained for the comparison of CPU runtimes for various elements is given in this chapter. Such a comparison shows that the implementation of three-node triangle RZT element formulation which had not been adopted for the static analysis of VSCLs before is effectively keeping the computational cost to its minimum level, without any extra degree of freedom and scarification of the numerical accuracy.

3.2 A three-layer sandwich plate with curvilinear fibers

A laminate with the dimensions of $a = b = 1.5m$, representing a three-layer Sandwich Structure with curvilinear fibers, is analyzed under a uniform pressure of $p_n = 10\ kPa$ with fully clamped boundary conditions as depicted in Fig. 2-1. The SP is made of glass-epoxy face sheets and an isotropic soft (foam) core with the thicknesses of $h_s = 0.02$ and $h_c = 0.06$, respectively. Accordingly, the span-to-thickness ratio of the laminate is computed as $\rho = a/(2h_s + h_c) = 15$, hence resulting in a moderately thick plate. The mechanical properties of the constituent materials are listed in Table 3-1. This problem is a well-known benchmark case solved by various researchers to test the capabilities of new continuum mechanics approaches against accurately predicting the bending behavior of a given composite structure. For instance, Tornabene et al. [142] utilized CUF with MZZF, and various higher order functions to interpolate the thickness displacement field for both LW and ESL approaches where the GDQ method was used for solution. They showed that inclusion of ZZ functions such as MZZF is necessary to capture the through-the-thickness ZZ behavior of sandwich structures with a soft core [142]. Therefore, this challenging test case is revisited herein to validate and demonstrate the bending of capability of enhanced RZT formulation for VS sandwich structures. The curvilinear paths for the reinforcing fibers in the face sheets are defined as:

$$\theta^{(1)} = \xi \sin\left(\pi\left(x/a + 0.5\right)\right),\ \theta^{(3)} = \theta^{(1)} + 90 \tag{3.1}$$

where $\theta^{(1)}$ and $\theta^{(3)}$ are sinusoidally varying fiber angles within the entire domain for the first and third plies, respectively, and the symbol ξ represents the maximum value of all fiber angles in the domain.

To evaluate the predictive capability of the proposed formulation herein, through the thickness variation of stress, strains, and displacements are studied for various maximum fiber angles, $\xi = 15, 30, 45, 60$, but the results are succinctly presented for only upper and lower bounds of these angles.

3.2.1 The curvilinear fiber path impact on distribution of displacements

As shown in Fig. 3-1, the through-the-thickness variation of in-plane displacements exhibits a highly ZZ trend due to the presence of relatively thick and soft core, which results in a sharp transition of stiffness between face sheets and core. It is notable from

Fig. 3-1 that the trend of the ZZ deformation mechanism of sandwich structures is negligibly affected by the presence of curvilinear fiber within the face sheet. Nevertheless, the change in the maximum angle of the curvilinear fibers from 15 to 60 degrees conspicuously alters the in-plane displacement values at bounding surfaces of the sandwich structures. This behavior is reflected as a shift of the ZZ displacement in Fig. 3-1.

Table 3-1 The mechanical properties of the materials for various cases.

Material	Elastic Moduli [GPa]	Poisson's Ratios	Shear Moduli [GPa]
Glass-epoxy	$E_1 = 53.78$, $E_2 = 17.93$, $E_3 = 17.93$	$\nu_{12} = 0.25$, $\nu_{13} = 0.25$, $\nu_{23} = 0.34$	$G_{12} = 8.96$, $G_{13} = 8.96$, $G_{23} = 3.45$
Foam	$E = 0.232$	$\nu = 0.2$	$G = 0.0966$
Carbon-epoxy	$E_1 = 137.9$, $E_2 = 8.96$, $E_3 = 8.96$	$\nu_{12} = 0.3$, $\nu_{13} = 0.3$, $\nu_{23} = 0.49$	$G_{12} = 7.1$, $G_{13} = 7.1$, $G_{23} = 6.21$

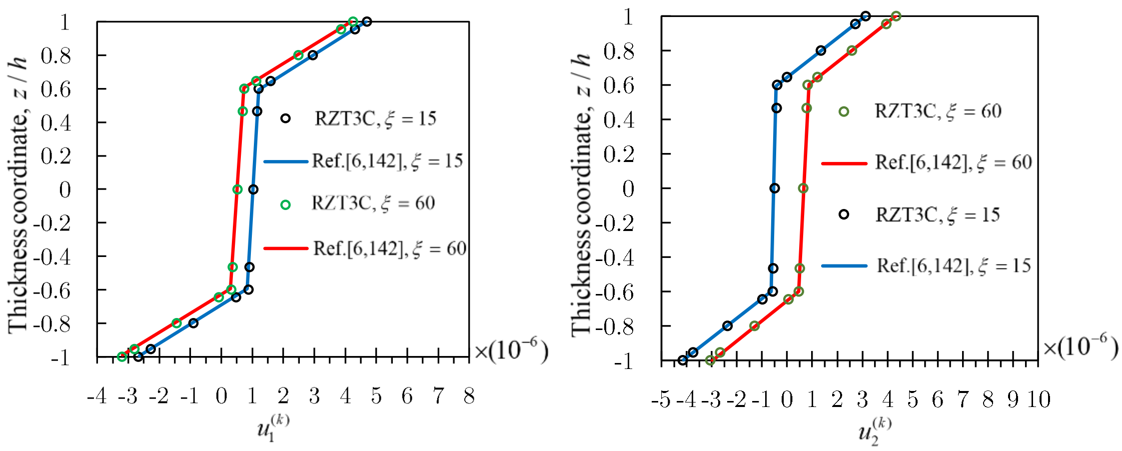

(a) (b)

Fig. 3-1 The variation of the through the thickness planar displacements (a) $u_1^{(k)}$, and (b) $u_2^{(k)}$ for the SP.

Capturing such complex deformation mechanisms is of great importance for design and optimization of sandwich structures with curvilinear fiber architecture; therefore, a robust and computationally efficient solution is required. The present RZT FE formulation addresses this need as demonstrated in Fig. 3-1, where the presented formulation captures the physics with an almost excellent accuracy as compared to the results of the solid FE model or high-order theories [6,142]. In addition, solid elements are known to be computationally demanding, thus limiting their applicability to complex large-scale structures with optimization process. On the other hand, our formulation can solve this problem more efficiently thanks to the low number of degree-of-freedom required per node.

3.2.2 The comparison of CPU runtime

As mentioned in the first chapter, the curvilinear fiber path modelling entails a relatively dense mesh regardless of the theory being used; therefore, for a fixed number of elements in the mesh, the size of global stiffness matrix becomes direct function of single independent variable, i.e., degree-of-freedom per node. Given the fact that the degree-of-freedom per node in higher-order deformation theories is two or more times greater than that of first-order deformation theory and/or RZT, the size of the resultant global stiffness matrix obtained using lower-order theories is much smaller than that of higher-order theories for the same discretization. Thus, the CPU time required to take the inverse of RZT global stiffness matrix is rather small compared to higher-order theories. Apart from efficiency against the high-order theories, the CPU runtime results obtained from RZT and solid FE analysis for the extreme case of $\xi = 60$ are compared in Table 3-2 for various mesh resolutions. For a fair comparison, the resolution of the mesh is kept the same as four cross triangles in one square for both 3D continuum and RZT3C and the resolution of four smaller squares contained in a larger square as the same size of the resolution in the previous two cases for the Quad-RZT4 elements to satisfy the continuity of the curvilinear fiber in the three cases.

Also, the computer used in this comparison has the following hardware capacity: Intel(R) Core(TM) i7-8750H CPU @ 2.20GHz with 32.0 GB installed RAM, and 64-bit Windows operating system. Note that the number of DOF of the solid element is three per node whereas the number of DOF of RZT elements is seven per node. On the other hand, for the solid element modelling, the thickness coordinate of the face sheets divided by 2 elements and core material thickness is discretized by 6 elements. As listed in Table 3-2, thanks to the lower number of total DOF (i.e., resulting in a smaller size of stiffness matrix), RZT3C becomes much more computationally preferable compared to the solid and Quad-RZT4 elements for all the in-plane mesh resolutions.

Table 3-2 The comparison of CPU runtime for various finite elements.

Element Type	Total Element Number	Total Node Number	Total DOF	MATLAB Solution Time (sec)
3D Solid Finite Element	$35\times35\times4\times10$	27731	83193	7.371
	$40\times40\times4\times10$	36091	108273	8.643
	$45\times45\times4\times10$	45551	136653	10.752
	$50\times50\times4\times10$	56111	168333	12.568
RZT3C	$35\times35\times4$	2521	17647	0.485
	$40\times40\times4$	3281	22967	0.642
	$45\times45\times4$	4141	28987	0.897
	$50\times50\times4$	5101	35707	1.189
Quad-RZT4	$35\times35\times4$	5041	35287	1.170
	$40\times40\times4$	6561	45927	2.535
	$45\times45\times4$	8281	57967	4.10
	$50\times50\times4$	10201	71407	5.845

3.2.3 The curvilinear fiber path impact on distribution of stresses

The stress variation along the thickness coordinate should be computed accurately for design of VSCL composites. To verify the accuracy of the present RZT element for stress predictions, the results of the in-plane and transverse-shear stress components are compared with those of literature obtained using high-order theories and/or solid elements in Figs.3-2 and 3-3, respectively. As it is seen from these graphs, the present low-order RZT element can attain almost identical variations of through-the-thickness in-plane stresses produced by continuum FE formulation. From a physical point of view, the in-plane stress along x_1-coordinate experiences a larger variation when the value of the ξ increases at the top ply. This mechanical behavior is because the larger the maximum fiber angle, the higher the spatial gradient of the fiber path will be, which reduces the number of fibers aligned along x_1-coordinate. Therefore, the stiffness of the sandwich structure at the top ply gets relatively smaller as the maximum fiber angle increases, which leads to a higher strain/stress accumulation within the top ply. Since the extreme fiber angle design case, $\xi = 60$, requires high-mesh resolution to be able resolve the spatial variation of the curvilinear fiber reinforcement, the use of solid elements will obviously be computationally expensive. Consequently, it will naturally not be preferred as compared to computationally more efficient lower-order RZT approach, which can provide the same order of accuracy as demonstrated in Figs.3-2 and 3-3.

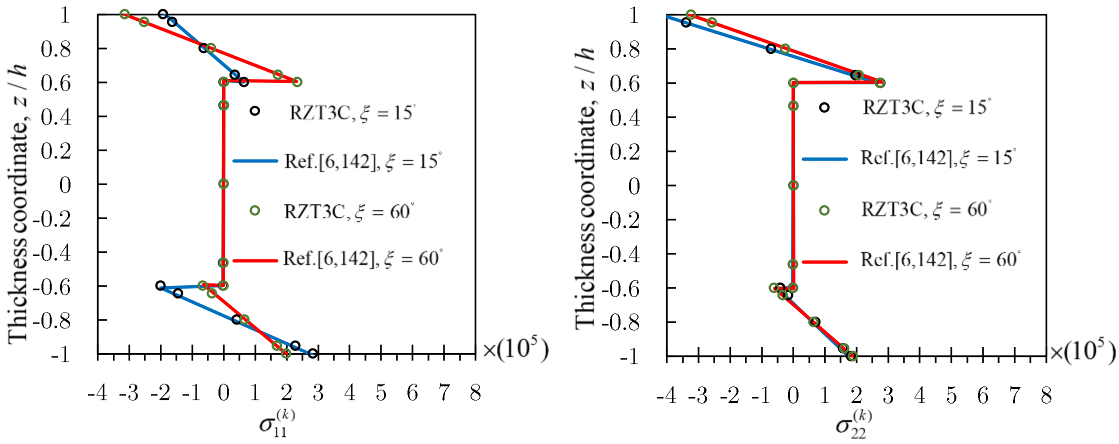

(a) (b)

Fig. 3-2 The variation of the through the thickness planar stresses (a) $\sigma_{11}^{(k)}$, and (b) $\sigma_{22}^{(k)}$ for the SP.

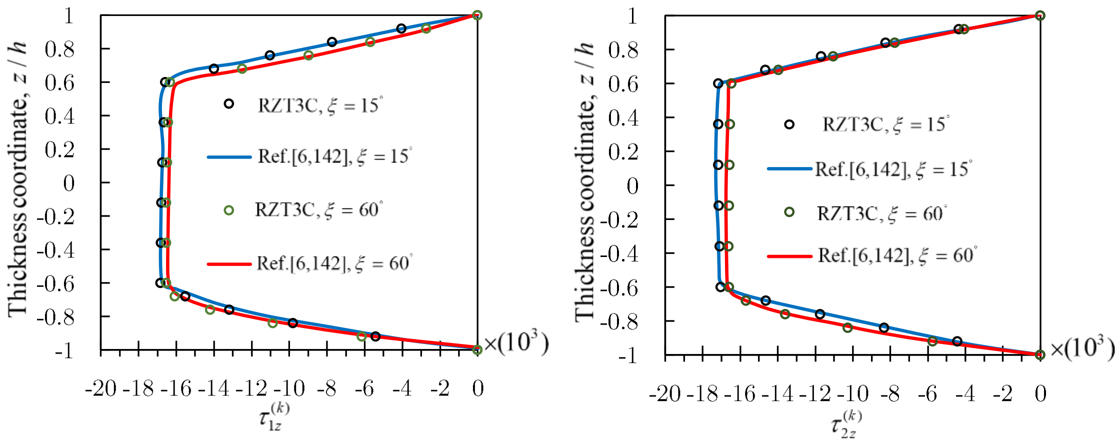

(a) (b)

Fig. 3-3 The variation of the through the thickness transverse shear stresses (a) ${\tau_{1z}}^{(k)}$, and (b) ${\tau_{2z}}^{(k)}$ for SP.

Considering the capability of the RZT3C element for curvilinear fiber reinforced composite designs, this element can be a potential candidate for its implementation into commercial FE packages such as ANSYS, ABAQUS, etc. In addition to in-plane stress accuracy, the presented RZT3C element can provide highly accurate transverse-shear stress distribution along the thickness of coordinate of sandwich structures with curvilinear fiber-reinforced face sheets as depicted in Fig. 3-3. This through-the-thickness stress variation is not affected by the gradient of the curvilinear fibers due to absorption of the shear stress within the thick and soft core. The effect of curvilinear fiber angles on transverse-shear stress variation will be investigated in the next test cases.

3.3 A two-layer curvilinear fiber reinforced square plate under a uniform pressure

The second case is a square laminate with two carbon-fiber reinforced plies having curvilinear fiber orientation. The mechanical properties of carbon/epoxy are given in Table 3-1. The edge size of the plate is $a = 1m$ and the thickness of both layers are equal and varies in accordance with selected span-to-thickness ratios of 10, 25, and 40. The geometry of plate is defined in a global rectangular Cartesian coordinate system (x_1, x_2, z) with its origin located at the left bottom corner of the plate. All edges of the plate are fully clamped and a uniformly pressure of $q_z = -10KN/m^2$ is applied on the top surface of the laminate. The VS is defined by the curvilinear fiber angle in each ply as [147]:

$$\theta^{(k)} = \left((\theta_1^{(k)} - \theta_0^{(k)}) \left| 2\bar{x}_1 - 1 \right| + \theta_0^{(k)} \right) \quad (k = 1, 2) \tag{3.2}$$

where $\bar{x}_1 = x_1 / a$ is the normalized coordinate and $\theta_i^{(k)}$ $(i = 0,1)$ is the upper/lower bounds of the fiber angles defined for the first and second layers as $\left(\theta_0^{(1)}, \theta_1^{(1)}\right) = \left(90, 90 - \phi\right)$ and $\left(\theta_0^{(2)}, \theta_1^{(2)}\right) = \left(0, \phi\right)$, respectively, where the parameter, ϕ, controls the angle of the fiber orientation on the bounding edges of plate within each ply. Among the investigated values of $\phi = 0, 15, 30, 45$, the through-the-thickness variations of mechanical responses calculated for the upper and lower bounds of the parameter, $\phi = 0, 45$ are presented for conciseness. All the presented results are calculated at the in-plane coordinate of the laminate, $x_i = a/4$ $(i = 1, 2)$.

3.3.1 The through-the-thickness variation of the displacements

Fig. 3-4 shows the variation of displacement components along the thickness coordinate of the laminate for case $\phi = 0, 45$, $a/2h = 10$. In Fig. 3-4a, there is a slight variation in the slope of in-plane displacement from the bottom to the top layers. The slope of u_1

displacements within the top layers is about 10% larger than that of the bottom layer. This can be attributed to the lower stiffness of the bottom layer since the stiffness along the x_1 -axis in bottom layer is less than the top one due to the variable fiber placement adopted. On the other hand, an inverse behavior is observed for the u_2 displacements as shown in Fig. 3-4b, where the displacement slope change is predicted 25% from bottom to the top plies. Both of in-plane displacements obtained from our solution are almost identical to those of the other theories in Figs. 3-4a and b, revealing that RZT3C element can capture the essential mechanical response highly curvilinear fiber reinforced moderately thick laminates.

In Fig. 3-4c, the comparison between the two extreme fiber orientation cases, $\phi = 0, 45$, indicates that when the fibers are straight, i.e., $\phi = 0$ corresponding to cross ply (0/90), the u_1 displacements is less affected by the asymmetry of the plies than that of highly curvilinear case, $\phi = 45$. To elaborate further, the displacement in the neutral plane shifts to a higher value if the fibers are curvilinear as shown in Fig. 3-4c due higher asymmetry of fiber alignments, which results in a lower membrane stiffness of the laminate but higher bending stiffness. Furthermore, in Fig. 3-4d, the deflection variation computed along the thickness coordinate is constant, which corresponds to the average of a nonlinear distribution that may be obtained from a 3D continuum solution. Specifically, upon comparing the reference average deflections of high-order theories with our predictions, almost excellent match between results can be observed, thereby proving the high accuracy of the RZT3C element.

3.3.2 The significance of curvilinear fiber path: distribution of in-plane and transverse shear stresses

To be able to reveal the capability of the present approach in terms of predicting other design parameters accurately, Fig. 3-5 presents the variation of the through-the-thickness normal in-plane and transverse-shear stresses as a function of different fiber orientations, $\phi = 0$ and $\phi = 45$, for the span-to-thickness ratio of $a/2h = 25$. As can be seen from Figs.3-5a and b that the curvilinear fiber placement reduces and balances the stress gradient along thickness direction causing the laminate to behave like a quasi-isotropic structure. As for the straight fiber placement ($\phi = 0$), the inverse behavior of bottom/top-plies' stress distribution observed in Fig. 3-5b with respect to ones in Fig. 3-5a is associated with the 90 degrees shift between fiber orientations within the corresponding plies.

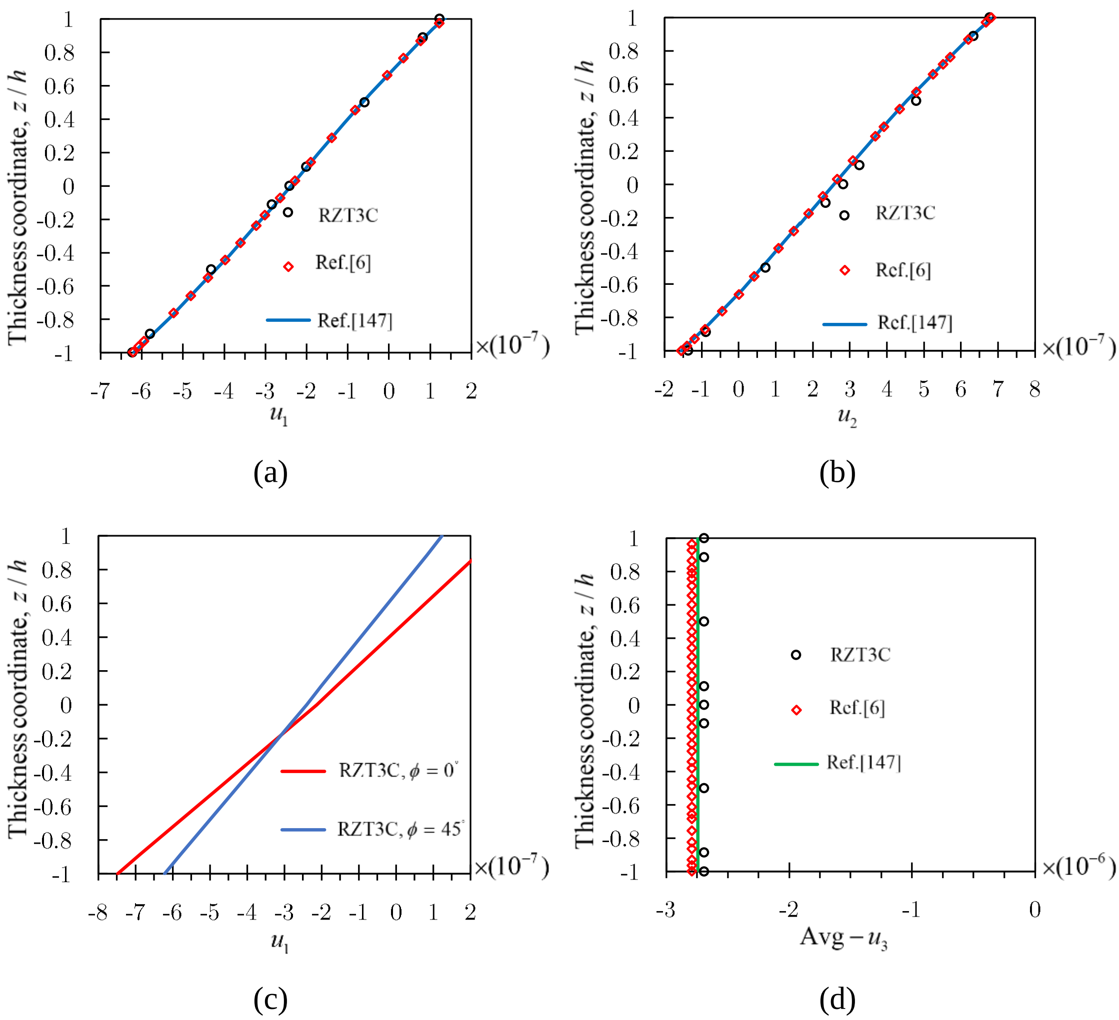

Fig. 3-4 The through-the-thickness variation of the planar displacements , $u_1^{(k)}$, $u_2^{(k)}$ and the transverse displacement, $u_3^{(k)}$ for square plate, $\phi = 0, 45, a/2h = 10$.

This flipped stress variation as well as the balanced stress variation for curvilinear fiber placement are captured almost perfectly by using RZT3C element as compared to the reference solutions obtained by high-order theories or solid element solution [6]. As seen from Figs.3-5c and d, the transverse-shear stress (i.e., obtained from Cauchy's equilibrium equations) for curvilinear fiber cases increases because of a decrease in the in-plane normal stress levels when switching from straight ($\phi = 0$) to curvilinear ($\phi = 45$) fiber placements. Remarkably, the rise in the transverse-shear stress is much smaller than the reduction in in-plane stress levels, thus resulting in a reduced equivalent (von Mises) stress. Hence, the curvilinear fiber placements provide a higher stiffness albeit the increase in the transverse-shear stress. This mechanical response is well captured by the RZT3C element along the thickness coordinate of the laminate as compared with the reference solutions given in the literature [6,147], revealing superior accuracy of the present approach.

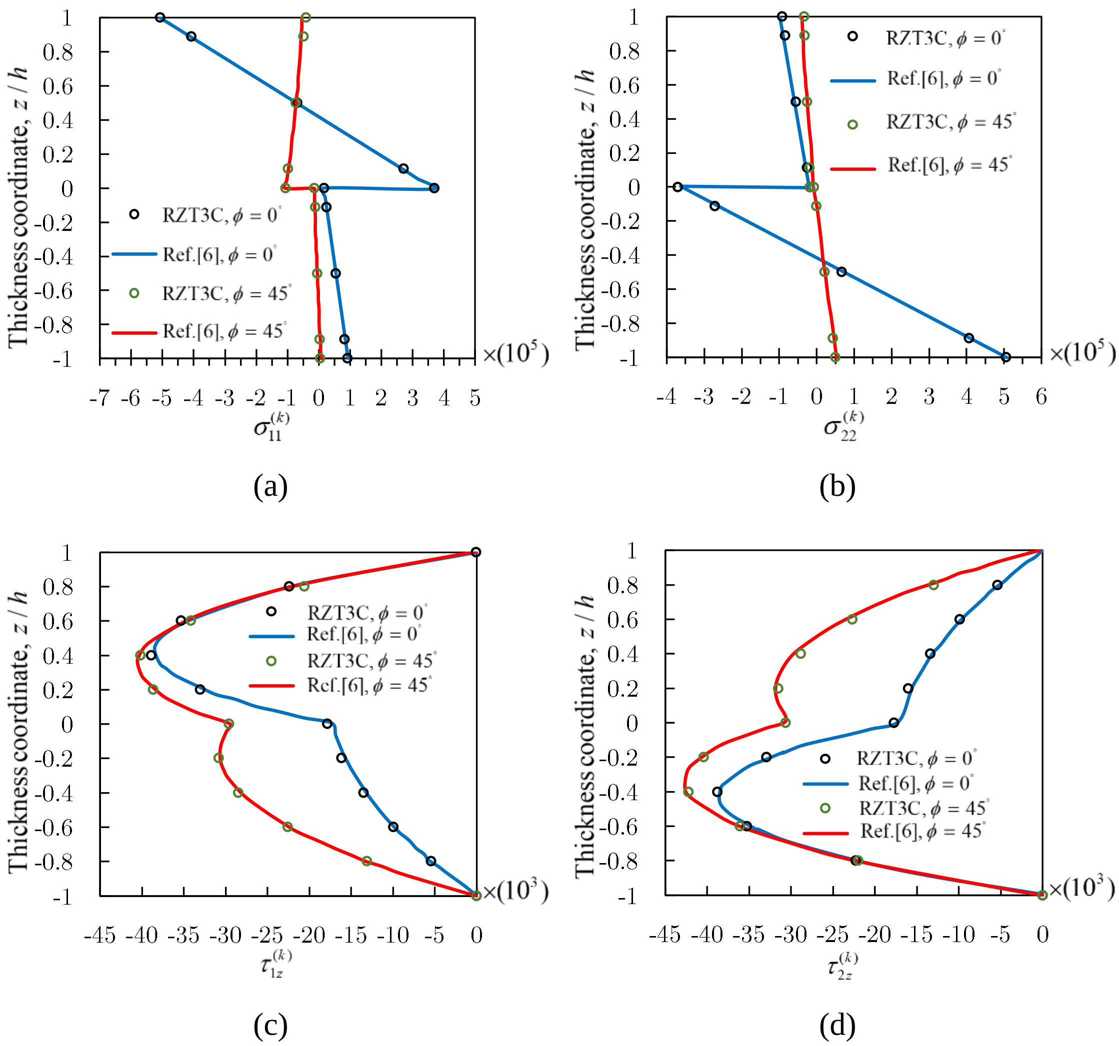

Fig. 3-5 The comparison of the through the thickness variation of the in-plane normal and transverse shear stresses, $\sigma_{11}{}^{(k)}, \sigma_{22}{}^{(k)}$, and $\tau_{1z}{}^{(k)}, \tau_{2z}{}^{(k)}$ for square plate, $\phi = 0, 45$, $a/2h = 25$.

3.3.3 The influence of span-to-thickness ratio on distribution of stresses

To further verify the accuracy of the proposed methodology, the in-plane and transverse-shear stress results are compared for two different span-to-thickness ratios of the curvilinear fiber reinforced laminates in Fig. 3-6. Note that, for conciseness of this case study, the stress results are only presented for x_2 coordinate. Expectedly, both stress magnitudes increase as the plate thickness is reduced. Also, the linear trend of stress distribution tends to become nonlinear for decreasing span-to-thickness ratio of the laminate. As for curvilinear fiber reinforcement, such a behavior is captured well by using our present methodology in a linear trend, which is comparably precise with respect to the results produced by higher-order theories [6,147]. This indicates that the extra kinematic variables (associated with thickness-stretching effects) used to derive higher-order theories becomes insignificant for obtaining accurate through-the-thickness distribution of in-plane/transverse-shear stresses as the laminate gets thinner (higher span-to-thickness ratio). Thus, the results produced by the proposed formulation converge to the predictions of the higher-order theories as can be observed in Fig. 3-6.

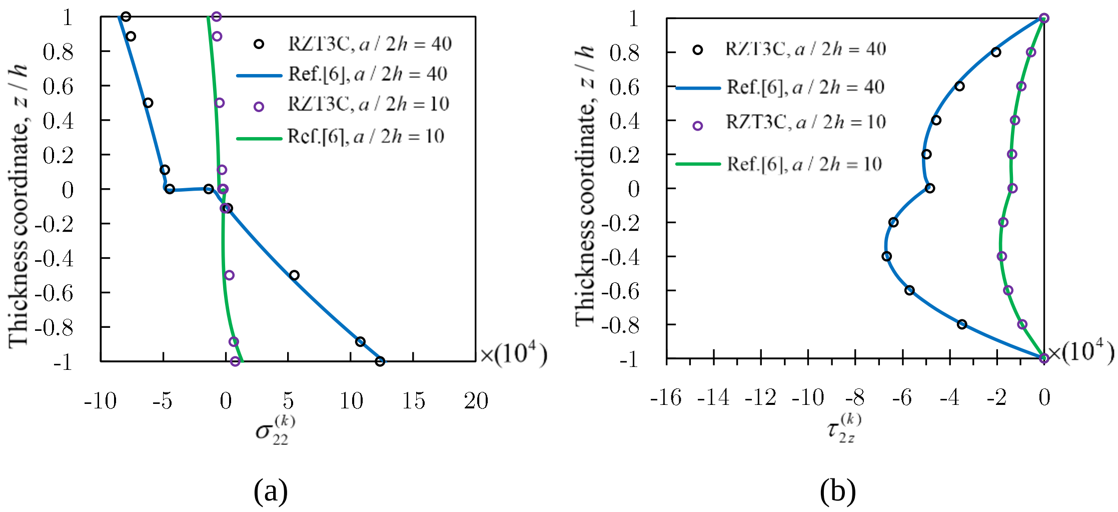

Fig. 3-6 The comparison of the through the thickness variation of the in-plane normal and transverse shear stresses, ${\sigma_{22}}^{(k)}$, and ${\tau_{2z}}^{(k)}$ for square plate, $\phi = 45, a/2h = 10, 40$

3.3.4 The comparison of the contours of stresses

Furthermore, for full-field verification of RZT3C results, the stress contours are compared in Fig. 3-7. As can be seen from these contour plots, in-plane stresses obtained from RZT3C analysis are almost indistinguishable from those generated by higher-order theories [6]. Hence, it can be concluded that the enhanced RZT formulation in this paper can be used as a viable and accurate modelling platform for structural analysis of complex curvilinear-fiber-reinforced composite structures.

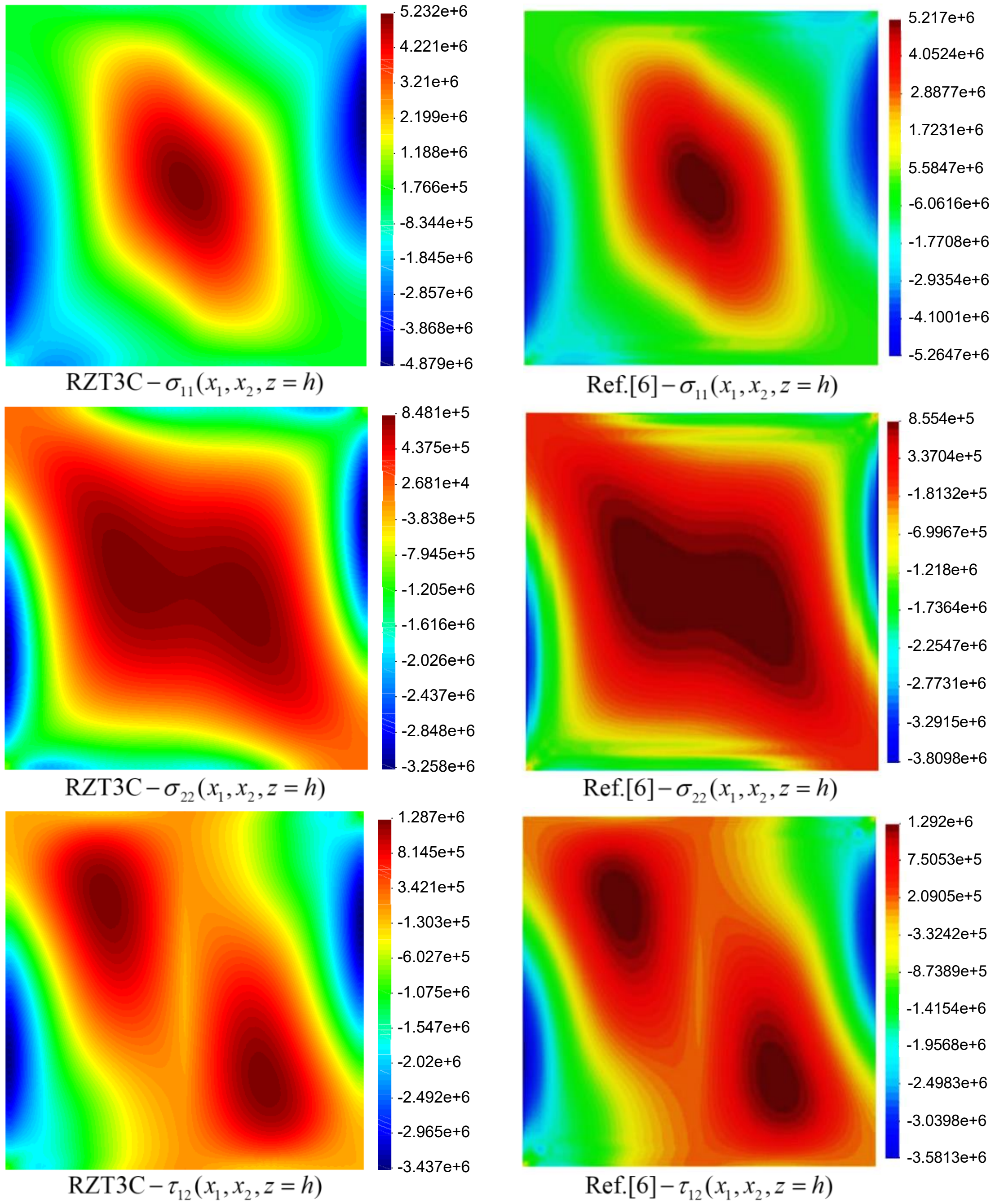

Fig. 3-7 The comparison of the contours obtained for normal and transverse shear stresses, $\sigma_{11}^{(k)}, \sigma_{22}^{(k)}$, and $\tau_{12}^{(k)}$ for square plate, $\phi = 45, a/2h = 40$.

3.4 The double layered curvilinear fiber laminated circular plate

The third case aims to demonstrate the capability of the proposed approach for modelling nonrectangular geometries where the curvilinear fiber placements need to conform the boundaries of the structural topology with a more complex pattern. To this end, a circular plate with two plies having curvilinear fiber orientations is modelled with fully clamped boundary condition under uniform transverse pressure of $q_z(z=h)=-10[KPa]$. The circular laminate is made of carbon fiber epoxy plies with identical thickness and has a radius of $r=0.5\,[m]$. The mechanical properties of carbon fiber reinforced epoxy composite are the same as the previous case study. Curvilinear fiber paths are described by the mathematical relation of $y^{(k=1)}=x^2$ for the first layer and $y^{(k=2)}=x^4$ for the second layer of the circular plate. Through the thickness variations of displacements and stresses are computed and presented at the position of $(r,\theta)=(0.25m,45^\circ)$ for different span-to-thickness ratios, i.e., $r/2h=10,15,$ and 20.

3.4.1 The correlation between span-to-thickness ratio and distribution of displacements

Figs. 3-8a and b compare the variation of in-plane displacements along the thickness direction for all the span-to-thickness ratios. Herein, the displacements vary linearly along the thickness coordinate. This is because there is an almost negligible effect of material transition between the plies on the deformation of the laminate. This physical behavior can be attributed to the smoothness and closeness of the fiber angles between the plies at the point of interest. Furthermore, the u_1 displacement is nearly zero at the neutral axis whereas the u_2 displacement has a finite value at the reference plate. This indicates that the curvilinear laminate exhibits a higher membrane response along the x_2-direction due to the lower number of curvilinear fibers aligned along x_2-direction than x_1-direction for which the membrane response is negligible. Moreover, for thicker plates, the slope of both in-plane displacements becomes shallower since the deflection variation with respect to x_1 and x_2 coordinates decreases. As for the deflection predictions, we present average values of transverse deflection along the thickness coordinate in Fig. 3-8c. Overall, displacement components are estimated with almost the same values as the reference 3D continuum solutions (i.e., obtained using ANSYS Solid185 element). This reveals that RZT3C element is capable of accurately modeling the mechanical response of moderately thick circular plates which are reinforced by curvilinear fibers.

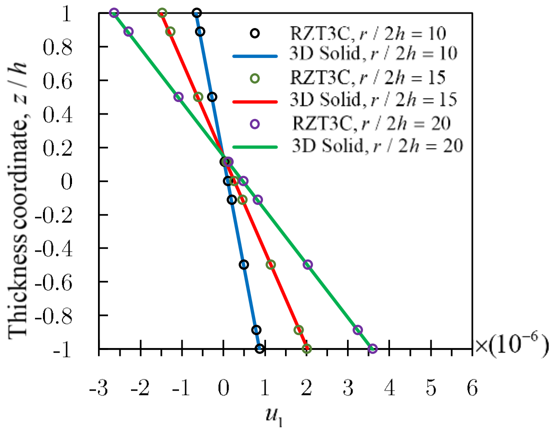

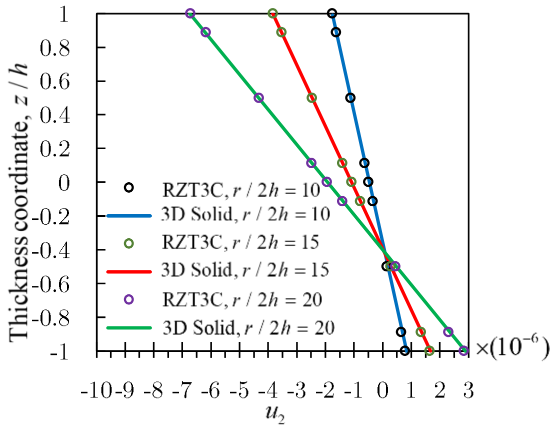

(a) (b)

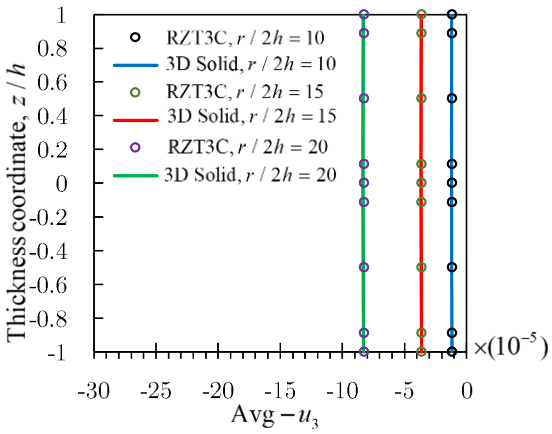

(c)

Fig. 3-8 Comparison of the through the thickness distribution of in-plane and transverse displacement results for circular plate, $r/2h = 10, 15, 20$.

3.4.2 The correlation between span-to-thickness ratio and distribution of stresses

Fig. 3-9 presents the through-the-thickness variation of in-plane and transverse stresses. In these graphs, the RZT3C formulation can capture identical stress variations along the thickness of the circular plate for a variety of span-to-thickness ratios. The perfect match between the computed normal stresses and the reference solutions clearly indicates that RZT3C element can take the first derivate of displacements accurately for a non-rectangular geometry. In addition, the RZT3C element can predict continuous transverse-shear stresses along the thickness coordinate of the circular plate as shown in Figs.3-9c and d. Expressively, the RZT3C results yield almost identically precise results of the ANSYS Solid185 element. This accuracy level lends itself to the efficient applicability of RZT3C approach for optimizing curvilinear fiber angles even for non-rectangular geometries. Overall, it can be concluded that RZT3C is a viable and accurate ESL approach for computing displacements and stresses of thin/moderately thick geometries of multi-layered composite and sandwich structures with curvilinear fibers.

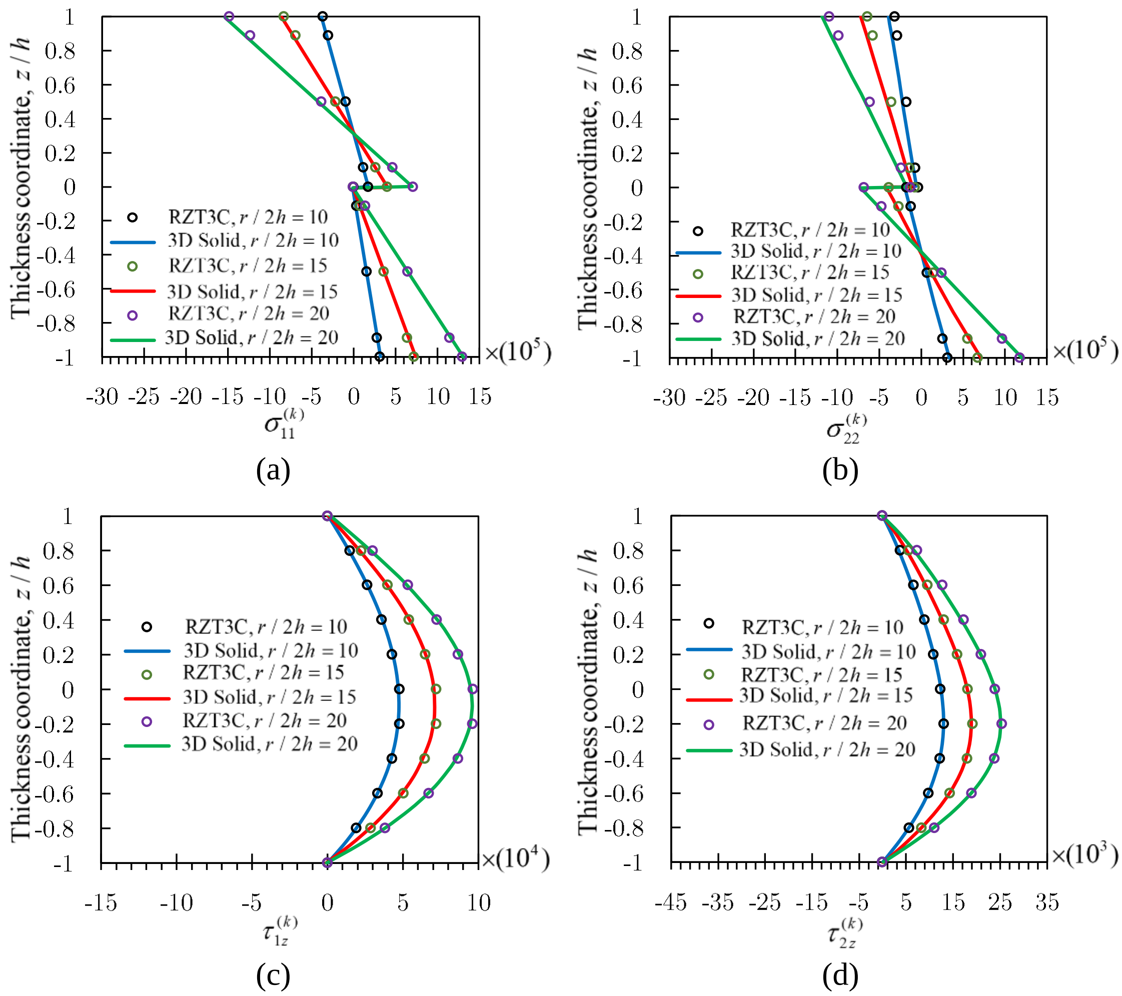

Fig. 3-9 Comparison of the in-plane and transverse shear stresses for circular plate, $r/2h = 10, 15, 20$.

4 STRUCTURAL ANALYSIS OF SANDWICH PLATES WITH VARIABLE STIFFNESS COMPOSITE SKINS AND FUNCTIONALLY GRADED CORES USING REFINED ZIGZAG THEORY

4.1 Overview

This chapter presents, for the first time in literature, the structural analysis of SPs made of FG core and curvilinear fiber-reinforced skins. The combination of continuous thickness-wise variation in the volume fraction of compositional constituents in the core, and the variation of curvilinear fiber angle with respect to the planar coordinates in the skins causes a more controlled stiffness variability in these structures. To model complex FG material systems with curvilinear fiber reinforcements accurately, an RZT-based ESL structural model (enhanced RZT3C formulation) was provided in the second chapter of this thesis. For simplicity and computational efficiency, the model adopts the shear-locking free three-node triangular RZT element which has not been reported to be utilized in any earlier research for structural analysis of FG sandwich laminates. This chapter comprehensively investigates several benchmark problems numerically with the objective of demonstrating the accuracy and boosted potential of the proposed model in evaluating the structural behavior of the laminates consisting of FG and VS layers.

Due to the lack of case studies on SPs with FG cores with curvilinear fiber-reinforced skins in literature, the enhanced RZT3C formulation is first verified by solving two existing benchmark problems for SPs with FG cores and UD fiber reinforced skins [207,240]. Two additional test cases are presented and numerically modeled as SPs that curved-fiber reinforced skins overlay the FG core. The first case in the latter group involves further extending the existing benchmark problem in refs. [6,142,241]. In this study, the isotropic homogeneous core of the SP with VS skins is replaced with an FG one. Also, the last case is designed to investigate an SP with a non-rectangular shape, an FG core, and curvilinear fiber-reinforced skins, utilizing the enhanced RZT formulation. To confirm the accuracy of the generated results for the latter group, they are compared with the results of Ansys 3D model solutions. It is shown that the proposed model accurately captures the results of the reference solutions for all the test cases. As a result, the enhanced RZT3C formulation shows adequate accuracy, and flexibility in dealing with complex combinations of design variables of the laminates incorporating both VS and FG layers. This makes the model to be robustly and reliably utilized as an analysis module compatible with optimization frameworks.

4.2 The equivalent mechanical properties of FG cores

As discussed in the first chapter of this thesis, FG materials are created by the continuous variation of multi-phase materials' constituents under a certain gradient profile. This profile determines the distribution of non-uniform macro properties of the FG plies [55]. Also, in chapter one, several homogenization models were shortly listed and introduced as methods of estimating the equivalent properties of the FG materials. In this chapter, the specific adaptation of power law function and law of mixtures to FG SP layers to estimate the equivalent mechanical properties is presented as follows. For the rectangular SP with an FG material core and orthotopic skins reinforced by unidirectional/curvilinear fibers as shown in Fig. 4-1, the x_1, and x_2 axes of the orthogonal coordinate system define the mid-plane. Also, the normal axis of the mid-plane defines the thickness coordinate.

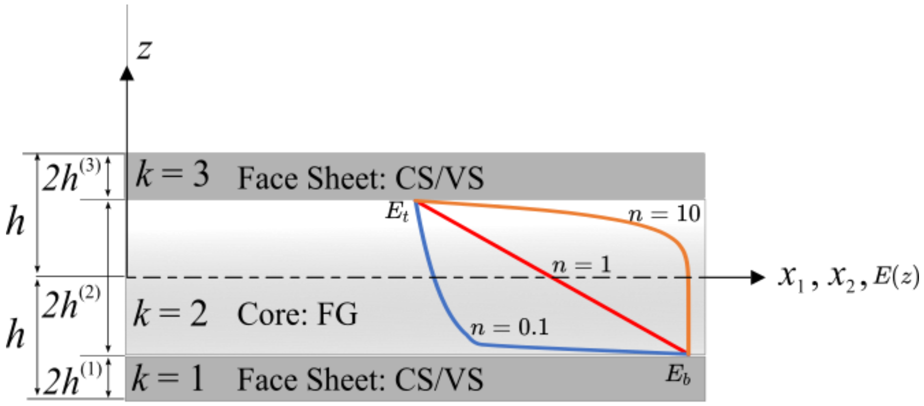

Fig. 4-1 The configuration of an SP with FG material core with CS/VS face sheets.

Based on the performance requirements, the mechanical properties of the top and bottom skins differ from those of the core. Table 4-1 lists the properties of materials used in the benchmark problems and test cases presented in this chapter. For the FG core, the thickness-wise variation of Young's modulus $E(z)$ follows the relation:

$$E(z) = (E_t - E_b)V(z) + E_b \tag{4.1}$$

$$V(z) = \left(\frac{z - z_b}{z_t - z_b} \right)^n \tag{4.2}$$

$$E(z) = 2G(z)\left(1+\nu\right) \tag{4.3}$$

where z_b and z_t denote the thickness coordinates, and E_b and E_t are the elasticity moduli at the bottom and top of FG material layer (core) respectively. The CG exponent or index CGI, n , regulates the material variation in the FG core, and ranges between 0.1 to 10 for the test cases presented in this chapter.

As is seen in Fig. 4-1 , for $E_b > E_t$, the CGI of 10, and 0.1 result in a stiffer and softer FG material core respectively. The Poisson's ratio, ν , is assumed to be constant along the core thickness as its variation has proven to be negligible [71]. Due to material gradient within the FG core, the shear modulus, which is directly related to the elasticity modulus, becomes dependent on the thickness. Results in this chapter describe the impact of tailoring the FG material on distribution of displacement/strains and stresses.

Table 4-1 The mechanical properties for the materials used in the test cases.

Material	**Elasticity Moduli [GPa]**	**Poisson's Ratios**	**Shear Moduli [GPa]**
Glass epoxy	$E_1 = 53.78$, $E_2 = 17.93$, $E_3 = 17.93$	$\nu_{12} = 0.25$, $\nu_{23} = 0.34$	$G_{12} = 8.96$, $G_{13} = 8.96$, $G_{23} = 3.45$
Foam-VS composite	$E = 0.232$	$\nu = 0.2$	$G = 0.0966$
Foam- UD composite	$E = 0.104$	$\nu = 0.3$	$G = 0.04$
Carbon epoxy	$E_1 = 157.9$, $E_2 = 9.584$, $E_3 = 9.584$	$\nu_{12} = 0.32$, $\nu_{13} = 0.32$, $\nu_{23} = 0.49$	$G_{12} = 5.930$, $G_{13} = 5.930$, $G_{23} = 3.227$

4.3 A three-layer cantilever SP with FG core and UD fiber skins

A three-layer laminated SP with the dimensions of $a = b = 1m$ is analyzed under uniform pressure of $p_n = 1\ MPa$ and fully clamped boundary condition on a single edge. The skins are made of UD carbon fiber-reinforced epoxy resin system, and the core is an FG soft foam material. The equivalent material properties of the FG core are calculated based on mixture rule given in Eqs.(4.1)-(4.3). The mean of the elasticity moduli of the top and bottom surfaces of FG core ($E_t = 0.0208\,GPa$ and $E_b = 0.1872\,GPa$, respectively) is equivalent to the elasticity modulus of a homogeneous isotropic foam. The CGI, n in Eq.(4.2) controls the material variation by taking values ranging from 0.1 (soft) to 10 (stiff). The thickness of top and bottom face sheets are identical with the value of

$h_s = 0.01$, and the core has the thickness of $h_c = 0.08$. The span-to-depth ratio (STD) of the laminate is calculated as $\rho = a / 2h = 5$, which corresponds to a thick plate. The orientations of the stacked laminae are $[0/0/0]$. Boundary conditions along $x_1 = 0$ for cross-ply and uniaxial laminate are as follows $u = v = w = \theta_x = \theta_y = \lambda_x = \lambda_y = 0$. In this benchmark problem, the thickness-wise stress distribution is studied for the isotropic homogenous core and the FG material core with various CGIs, $n = 0.1, 1,$ and 10. To compare results obtained by the proposed approach of this thesis with the those of literature, the stress components are presented in a dimensionless form as:

$$\bar{\sigma}_{11} = \frac{(2h)^2}{p_n a^2} \sigma_{11}, \bar{\sigma}_{1z} = \frac{2h}{p_n a} \sigma_{1z} \tag{4.4}$$

4.3.1 The relationship between the compositional gradient of the FG core and variation of stresses

Figs. 4-2 and 4-3 show the variation of in-plane and transverse shear stresses of the cantilevered FG-SP across the thickness. To illustrate the effect of the of clamped boundary condition on the stress distribution, the data is collected from a near-clamp position, namely, $(x_1, x_2, z) \equiv (0.2m, 0.5m, z)$. The computed thickness-wise stress data are compared with the results of 3D solid elements, and the PD-RZT solutions available in the literature [207]. As shown in Fig. 4-2, ZZ pattern in the thickness-wise in-plane stress distribution is owing to the abrupt change in the material properties at the interface between thick and soft core and the face sheet. It is noticeable from Fig. 4-2a that if the CGI is set to be unity, the ZZ pattern is nearly identical to that of the SP with isotropic homogeneous core. This behavior can be attributed to the uniform distribution of the stiffness along the thickness of the FG material core. However, the outer surfaces of the face sheets and the interface between the core and the face sheets experience a slightly higher level of in-plane stress for the FG-SP than for SP with the isotropic homogenous core. FG-SP with $n = 1$ exhibits less stiff behavior than the SP with a CS core. Therefore, FG core undergoes higher deformation thereby leading to an increase in the values of the in-plane stress.

Nonetheless, as shown in Fig. 4-2b, the change from $n = 0.1$ to 10 conspicuously alters the values of the in-plane normal stresses at the interfaces between the core and the face sheet as well as the bounding surfaces of SP. Upon raising the value of n from 0.1 to 10, the core stiffness increases, which naturally reduces magnitude of stress/strain therein. It is seen that the presented model's results show quite good congruence with results of 3D FEM and PD-RZT [207]. It should be stated that the accurate and computationally efficient calculation of deformation fields is rather critical for the design and optimization of FG sandwich structures. The RZT3C formulation of this study outperforms higher order or non-local particle-based solutions in terms of computational efficiency.

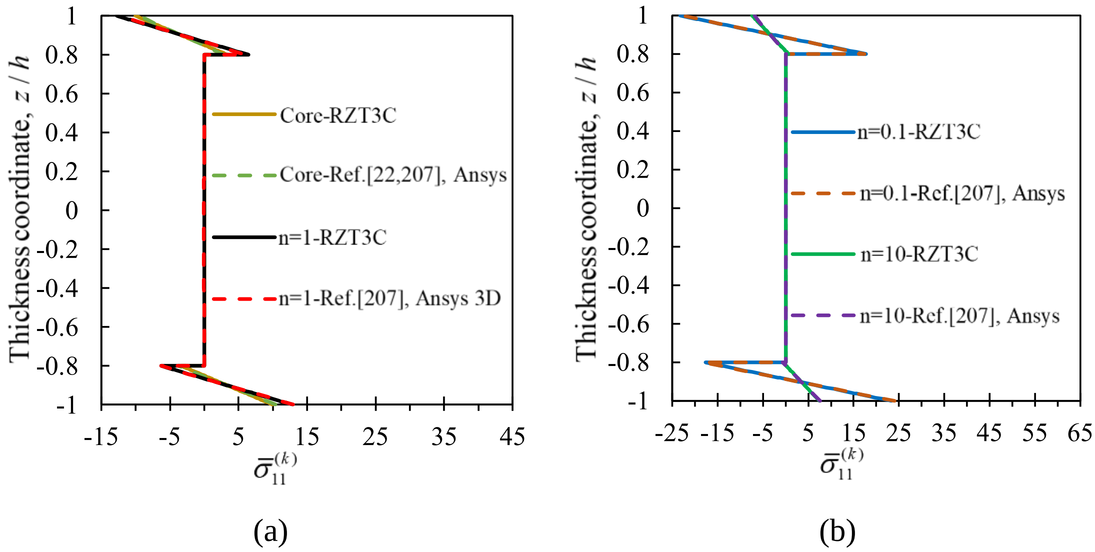

Fig. 4-2 The thickness-wise variation of the normalized in-plane stress, $\bar{\sigma}_{11}^{(k)}$, for the FG material core cantilevered SP.

To further verify the current RZT formulation, Figs. 4-3a and b compare the transverse components of the shear stress for the isotropic homogenous core and FG material cores with various CGIs with the results of literature obtained using PD-RZT theories and/or solid elements. Both figures demonstrate that the enhanced RZT3C formulation can well match results of reference solutions in literature and 3D solid elements solution. As can be seen in Fig. 4-3a, for $n=1$, the transverse shear stress gradually decreases from bottom to top of the FG core due to the higher stiffness at the bottom of the FG core whereas it does not change for SP with an isotropic homogenous core. It is noted that the normalized transverse shear stresses become maximum in the skins of SP as expected. Referring to Fig. 4-3b, the transverse shear stress values within the core and interfaces of core and face sheets for $n=0.1$ are smaller than those for $n=10$. An inverse relation holds for the face sheets since the FG core with lower stiffness value ($n=0.1$) experiences larger deformation thereby leading to notably higher values of transverse shear stresses in the skins. The overall results clearly reveal that on tailoring the material properties of FG core, the magnitudes of both axial stresses and transverse shear stresses at the interfaces between the core and face sheets as well as within the face sheets can be significantly reduced. This is quite important to design and manufacture delamination resistant SPs.

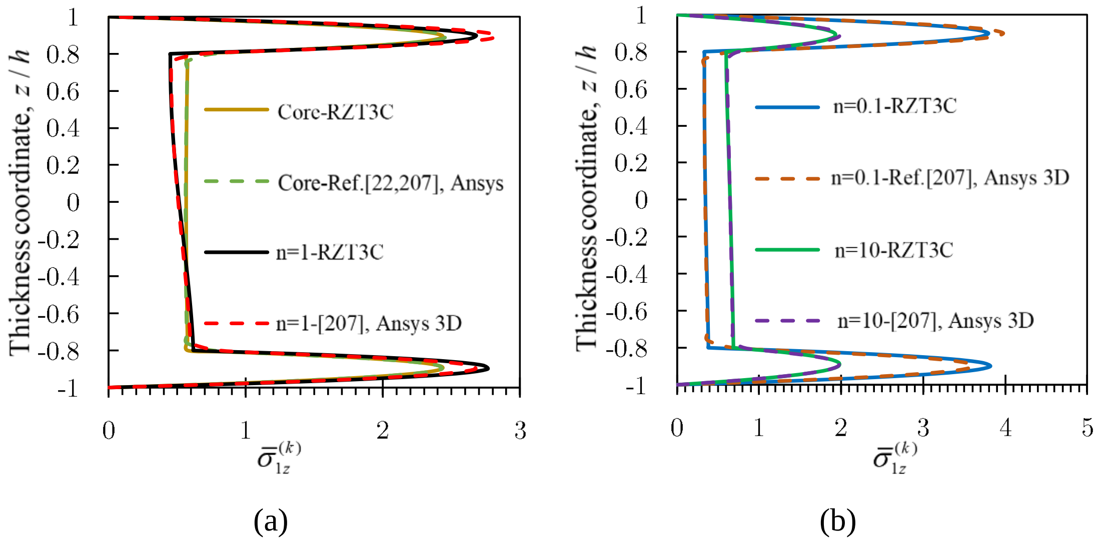

Fig. 4-3 The thickness-wise variation of the normalized transverse shear stresses, $\bar{\sigma}_{1z}^{(k)}$, for the FG material core cantilevered SP.

4.4 A seven-layer simply supported SP: FG material core and UD fiber reinforced skins

The second problem involves a symmetrical square SP made of an FG core material and multi-ply UD Carbon fiber-reinforced epoxy matrix face sheets. The ply orientation scheme of the face sheet is $[0^{\circ}, 90^{\circ}, 0^{\circ}, \bar{0}^{\circ}]_s$. The dimensions of plate edges are $a = b = 1m$ with the total laminate thickness of $2h = 0.2m$. Each skin is composed of three equal-thickness orthotropic plies and has the total thickness of $2h_s = 0.02m$. The schematic of the simply supported SP is shown in Fig. 4-4. The stiffness of FG core with identical mechanical properties at its bottom and top to those used in the previous benchmark problem is varied along the thickness coordinate of the laminate by selecting a CG exponent ranging from 0.1 to 10 in Eqs.(4.1)-(4.3). A uniform bivariate sinusoidal pressure of $p_n = 1\ MPa$ is applied to the top surface of the laminate in accordance with the following relation:

$$P = P_n \sin(\pi x_1/a)\sin(\pi x_2/b) \quad (0 \le x_1 \le a, 0 \le x_2 \le b) \tag{4.5}$$

The kinematic constraints for simply supported edges across the $x_1 = 0$ and $x_1 = a$ are as:

$$v = w = \theta_x = \lambda_x = 0 \tag{4.6}$$

and along the $x_2 = 0$ and $x_2 = b$ are as:

$$u = w = \theta_y = \lambda_y = 0 \tag{4.7}$$

The thickness wise stress distributions are evaluated against the results of the 3D FEM and reference solutions [207,240] at three different locations in Fig. 4-4 as $A(x_1, x_2) \equiv (0.5a, 0.5b)$, $D(x_1, x_2) \equiv (0.75a, 0.5b)$, and $E(x_1, x_2) \equiv (0.5a, 0.75b)$. For simplifying the comparison, the stress components are written in dimensionless as $(\bar{\sigma}_{11}, \bar{\sigma}_{1z}, \bar{\sigma}_{2z}) = (2h/P_n a)(\sigma_{11}, \sigma_{1z}, \sigma_{2z})$.

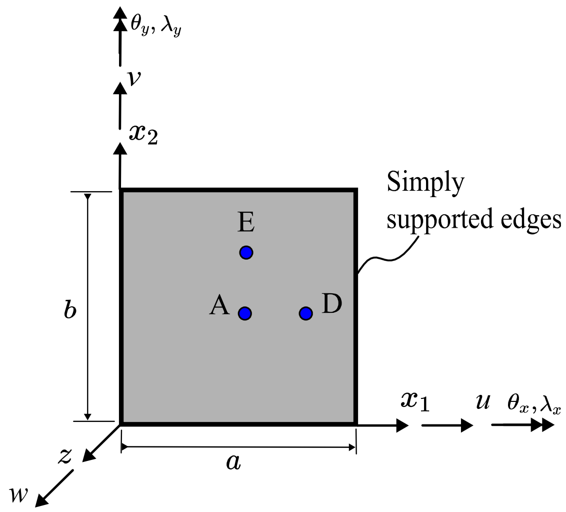

Fig. 4-4 Simply supported FG-SP.

4.4.1 The FG core's compositional gradient role: in-plane stresses

Fig. 4-5 presents the variation of in-plane stresses along the thickness of the laminate at point A. The significant difference in material properties between the core and the skins results in a noticeable ZZ transition. Based on the stress distributions given in Figs. 4-5a and c, the in-plane stress profile of the laminate with the FG core of $n = 1$ is slightly greater than the one with the isotropic homogeneous core at the interfaces. This is because the softer FG core with ($n = 1$) undergoes higher degree of bending deformation. The fact that the current computational approach can capture such as minuscule difference between FG core of $n = 1$ and isotropic homogeneous core is an indication of accuracy and sensitivity of presented formulation. By varying n from 0.1 to 10, the stress gradient between the core and face sheets in the thickness direction is reduced since stress magnitude of face sheet approaches to that of FG core as can be seen in 4-5b and d. This leads to quasi-isotropic structure-like response in the FG sandwich panel. As can be concluded from these two figures, the results are in very good agreement with both PD-RZT [207] or solid element solutions.

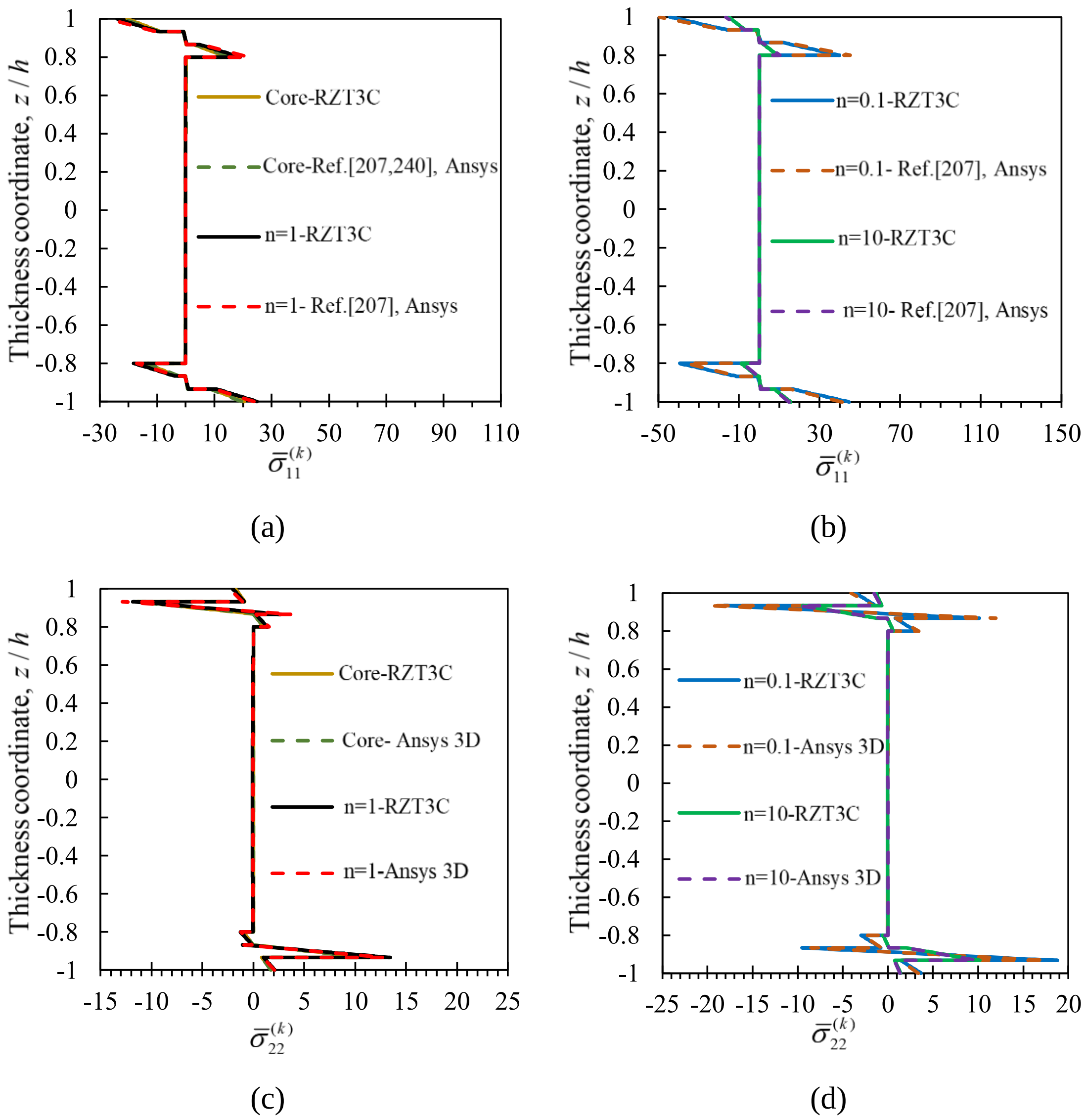

Fig. 4-5 The thickness-wise variation of the normalized in-plane stresses, $\bar{\sigma}_{11}{}^{(k)}$ and $\bar{\sigma}_{22}{}^{(k)}$, at point A.

4.4.2 The FG core's compositional gradient role: transverse shear stresses

Figs. 4-6 and 4-7 compare the transverse shear stresses for SPs with an isotropic core and FG cores with various CG exponents. The transverse shear stress reaches its maximum within the domain of the skins of the SP. Additionally, as the stiff material phase in the FG core increases with the increase of n from 0.1 to 10, the skins experience lower levels of shear stress. Indeed, the higher the stiffness of the FG material, the lower the magnitude of bending strain/deformation and stress. However, the stiffer constituent in the FG core increases stress not only in the core but also in the core-skins interfaces.

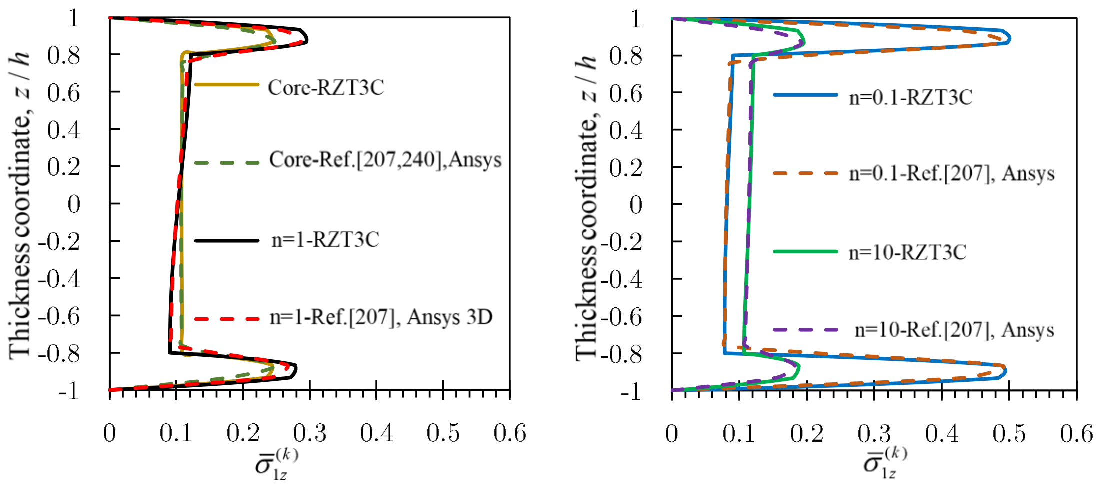

(a) (b)

Fig. 4-6 The thickness-wise variation of the normalized transverse shear stresses, $\bar{\sigma}_{1z}{}^{(k)}$, at point D.

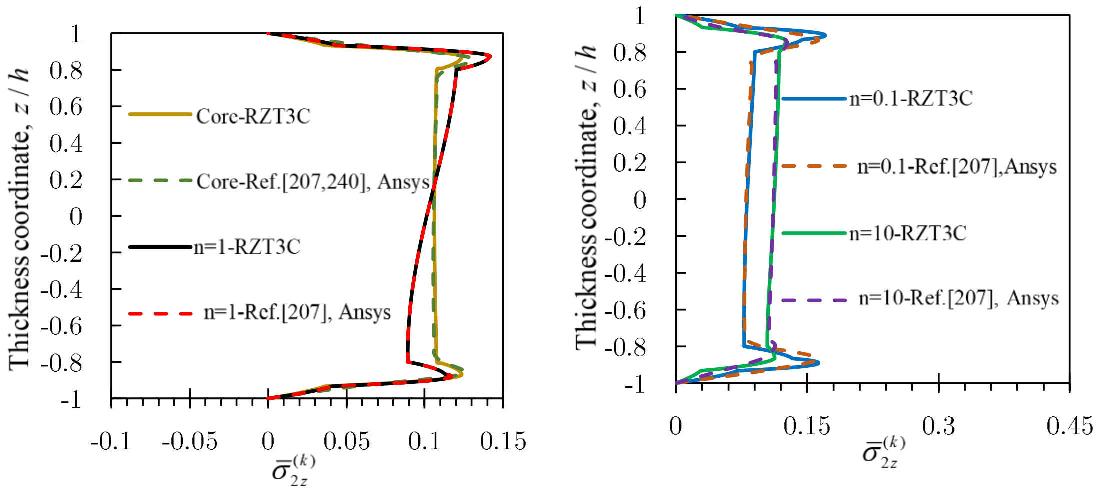

(a) (b)

Fig. 4-7 The thickness-wise variation of the normalized and transverse shear stresses, $\bar{\sigma}_{2z}{}^{(k)}$, at point E.

The opposite reaction of the skins and the FG material core is attributed to the increase in stiffness of the FG material core and decrease in the strain of the skins. Thus, by adjusting the material properties of the core, the level of the transverse shear stress at the interface between the core and the skins can clearly be minimized. It should be stated that the standard RZT formulation can only render average values for transverse shear stresses and fails to ensure their continuity at plies interfaces. However, the current formulation can predict transverse stress components as accurately as PD-RZT and 3D continuum solutions by utilizing posteriori stress recovery approach obtained from Cauchy's equilibrium. These findings confirm that the utilization of small number of kinematic variables in the current formulation does not impair the accuracy of in-plane normal and shear stresses.

4.5 A three-layer fully clamped rectangular SP: FG material core and curvilinear fiber reinforced skins

So far, FG sandwich panels with UD fiber reinforced orthotropic skins have been investigated as benchmark problems. Here, as the third example, the FG material core SPs with curvilinear fiber reinforcement (VS skins) will be studied to demonstrate the accuracy of the enhanced RZT3C formulation in predicting the bending behavior of FG-SP plate with VS skins.

Upon using appropriate curvilinear fiber orientations in the skins, the mechanical behavior of the FG-SP can be tailored to meet the technical requirements of specific applications. That is, the continuous variation of the elasticity modulus of the core material along the thickness direction as well as the in-plane variation of fiber angle in the skins enables steering stress fields along the desired directions. To this end, a three-layer FG-SP composed of FG foam core and curvilinear glass fiber-reinforced epoxy skins is modeled under fully clamped boundary conditions and subjected to uniform normal pressure of $p_n(\mathbf{x}, z = h) = 10\ kPa$. The laminate is illustrated in Fig. 2-5 and has the side dimensions of $a = b = 1.5m$. Both skins have the thickness of $h_s = 0.01m$ and the thickness of the core is $h_c = 0.03m$, resulting in a span-to-thickness ratio of $\rho = a/2h = 15$. The FG core is graded along its thickness direction so that the mean of the elasticity modulus at the top ($E_t = 0.0464\,GPa$) and the bottom ($E_b = 0.4176\,GPa$) is equal to that of the homogeneous isotropic foam core as given in Table 4-1. The mechanical properties of a material point within FG material core are controlled according to the power-law rule in Eqs.(4.1)-(4.3). That is, varying CG exponent, n from 0.1 to 10 makes the FG material core stiffer.

To generate the curvilinear fiber path within the skins, the following mathematical relation is utilized.

$$\theta^{(1)} = \phi \sin\left(\pi\left(x_1 / a + 0.5\right)\right),\ \theta^{(3)} = \theta^{(1)} + 90 \tag{4.8}$$

Here, $\theta^{(1)}$ and $\theta^{(3)}$ denote the fiber orientation at any material point in the bottom and top skins, respectively, defined according to reference point located at the left bottom corner of the plate. ϕ is a coefficient which controls the magnitude of fiber angle in the ply. For this test case, thickness-wise distribution of the displacements, strains and stress are studied for $n = 0.1, 1, 10$ and $\phi = 15^\circ, 60^\circ$ at $(x_1, x_2) \equiv (0.25a, 0.25b)$.

4.5.1 The FG core's compositional gradient contribution to variation of displacements

Fig. 4-8 illustrates the thickness-wise variation of displacement components of the FG-SP for different n values and $\phi = 60^\circ$. As can be seen from Figs.4-8a and b, the thickness-wise variations of in-plane displacements follow a non-linear ZZ trend due to the presence of the FG material core. On the other hand, this trend is linear for the CS soft core. Furthermore, it is seen that the higher stiffness of the FG material core at the bottom surface as well as the curved fiber orientation in the lower skin prevent the abrupt variation in the in-plane displacements while moving from core to the bottom skin. However, this trend is severe between the top of FG core and the top skin. The reason why both bottom and top interface behave differently is associated with large difference in the stiffness values therein. Also, as the value of n increases, the thickness-wise variation of the in-plane displacements decreases owing to the increased stiffness of the FG material core, which reduces bending of FG-SP.

As for transverse displacements, FG-SP plates can have larger and smaller absolute displacement values than isotropic homogenous core depending on CGI value. For example, FG-SP is softer than SP isotropic homogenous core for $n = 0.1$ and 1. This can be utilized to be able to tailor bending behavior of FG-SP system. The results of the current RZT3C formulation are in very good agreement with that of simulations based on the Ansys 3D continuum element.

4.5.2 The FG core's compositional gradient contribution to variation of in-plane normal and shear stresses

The thickness-wise variations of in-plane normal and shear stresses are displayed in Fig. 4-9 for the FG material core with different CGIs $n = 0.1, 1, 10$ and the isotropic homogeneous core, at a constant value of $\phi = 60^{\circ}$.

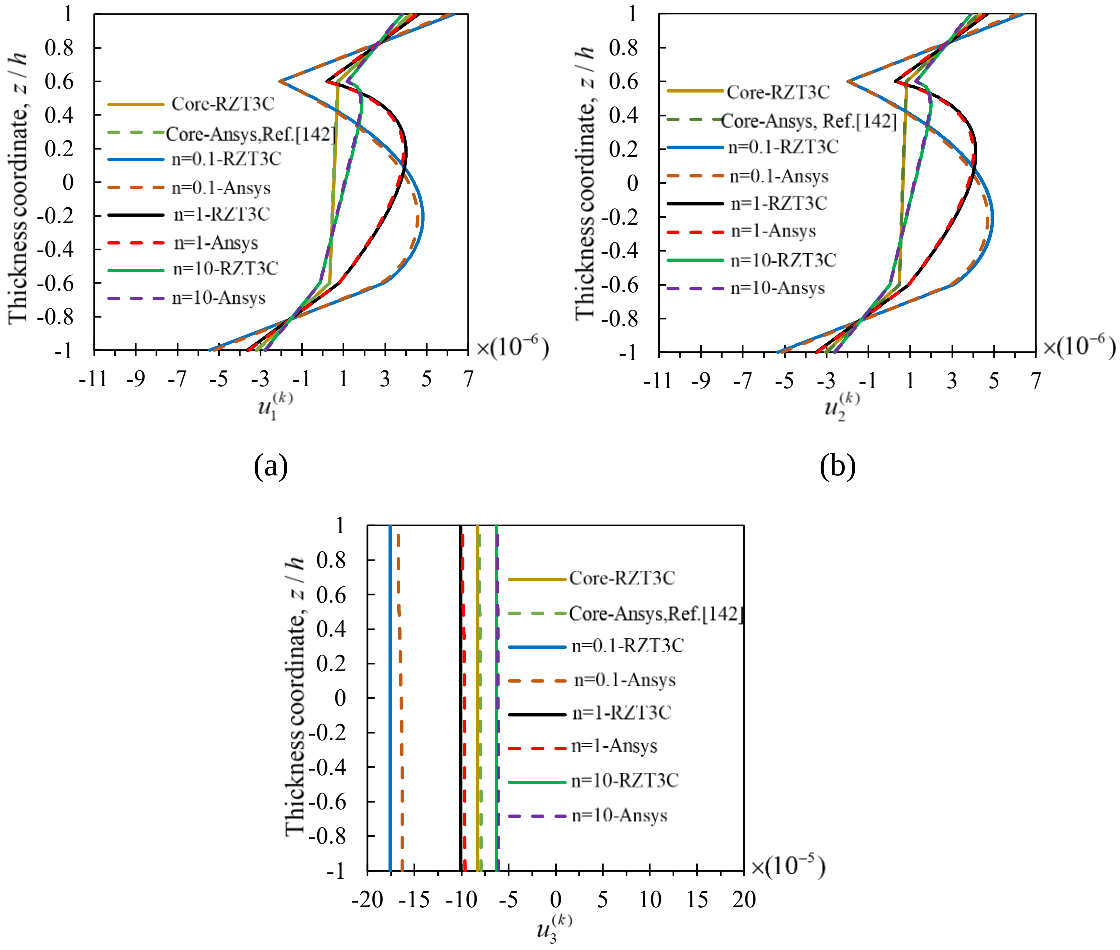

(a) (b)

(c)

Fig. 4-8 The thickness-wise variation of the in-plane, and transverse displacements $u_1^{(k)}, u_2^{(k)}$ and $u_3^{(k)}$ for the FG-SP for $\phi = 60^{\circ}$.

As illustrated in Figs. 4-9a and c, the profiles of the in-plane normal and shear stress for $n = 1$ are nearly identical to those for the isotropic homogeneous core due to the evenly distributed stiffness of the FG material core throughout the thickness. In these graphs, the increase in the in-plane normal and shear stress values at the core-skin interface for $n = 1$ is associated with greater bending deformation of FG-SP than SP with homogeneous core. Additionally, as shown in Figs. 4-9b and d, the increase in the CGI from $n = 0.1$ to 10 results in a stiffer laminate which better resists against bending and thus lead to lower level of strain/stress values in both skins and core-skin interfaces. Furthermore, for all cases given in Fig. 4-9, the magnitude of in-plane normal and shear stress variation for the bottom skin is smaller than the top one due to higher spatial concentration of curvilinear fiber in the bottom skin in the x_1 direction.

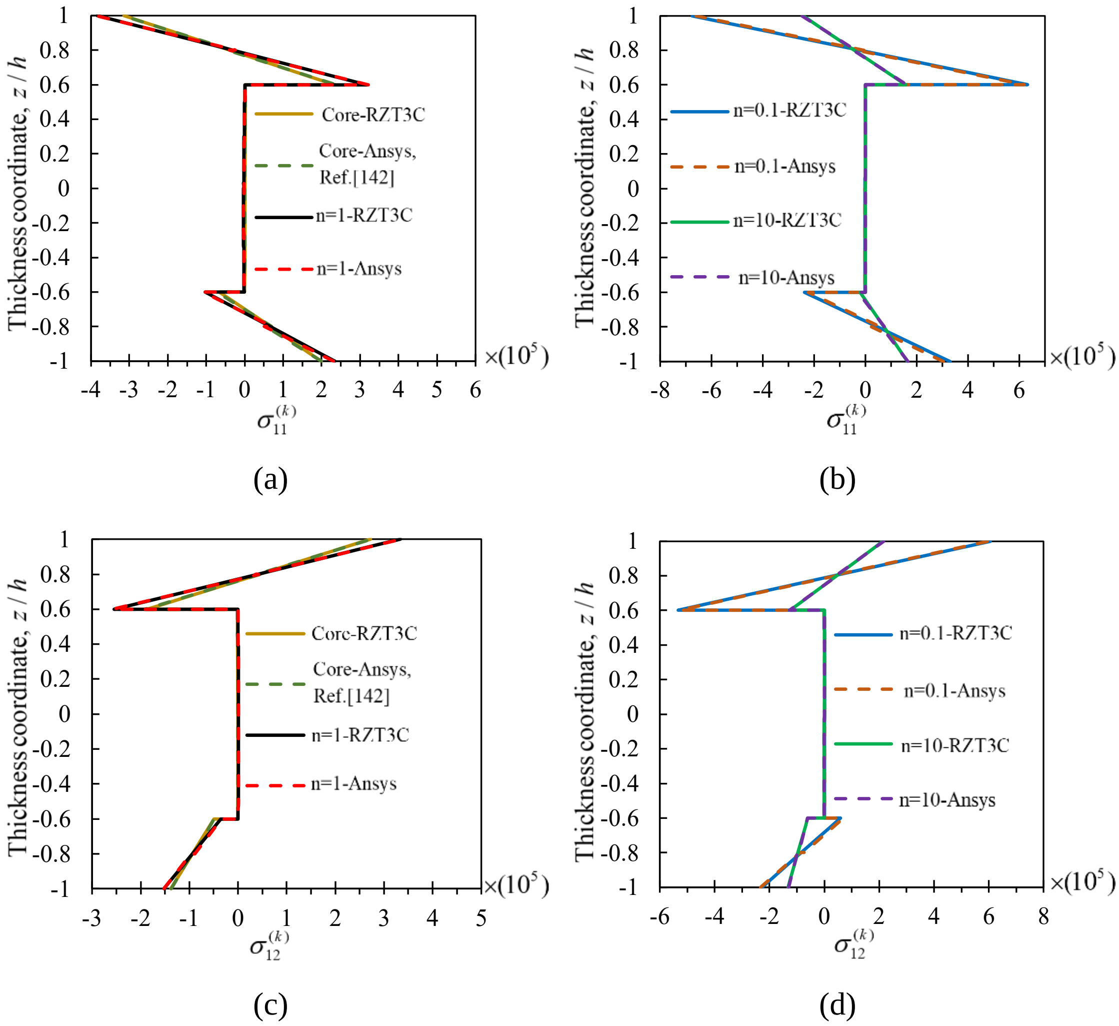

Fig. 4-9 The thickness-wise variation of planar normal and shear stresses, $\sigma_{11}^{(k)}$ and $\sigma_{12}^{(k)}$, for the FG-SP for $\phi = 60^\circ$.

4.5.3 The FG core's compositional gradient and the variation of transverse shear stresses

Fig. 4-10 presents thickness-wise comparisons of the transverse shear stresses for the homogenous isotropic core and FG material core with various CGIs. As seen from Fig. 4-10a, both FG-SP with $n = 1$ and SP with isotropic core have nearly identical thickness-wise variation of the transverse shear stress as expected. However, for $n=0.1$ and $n=10$, transverse shear stress variations given in Fig. 4-10b are notably different from each other. To be exact, within the core and core-skin interface, transverse shear stress value for $n=0.1$ is lower due to reduced stiffness of the core. Yet, in the bottom skin, it is larger due to soft core and stiffer bottom skin as a result of curvilinear fiber. Unlike previous benchmark problems for $n=0.1$, there is no reflection symmetry in transverse shear stress along the thickness direction with respect to mid-plane due to the asymmetry in fiber orientations in both bottom and top skins. As for $n=10$, due to the greater stiffness of the FG core which dominantly bears the transverse shear stress, there exists similar pattern of stress distribution in both skins. In passing, it is valuable to note that the results are well verified with that of 3D Ansys solutions.

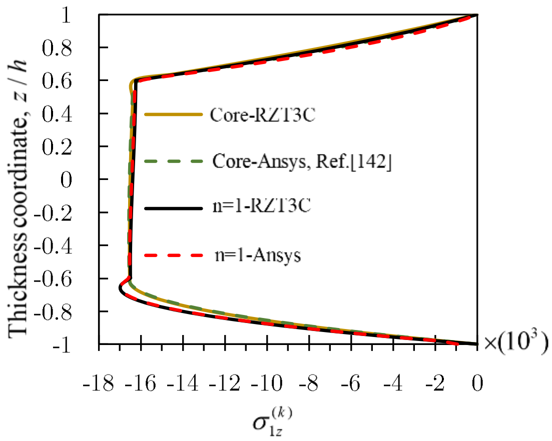

(a)

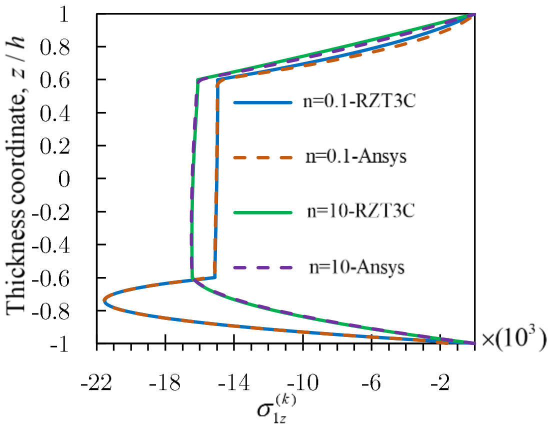

(b)

Fig. 4-10 The thickness-wise variation of transverse shear stress, $\sigma_{1z}^{(k)}$, for the FG-SP for $\phi=60^{\circ}$.

To investigate the effect of curvilinear fiber placement on the thickness-wise variation of displacements and stresses of the FG-SP, results for the maximum fiber angles of $\phi=15^{\circ}$ and $\phi=60^{\circ}$ in the subsequent discussion for $n=0.1$, and 10 are going to be presented.

4.5.4 The curvilinear fiber path influence on the profiles of in-plane displacements

Fig. 4-11 illustrates that the variation of the maximum curvilinear fiber angle from $\phi=15^{\circ}$ to $\phi=60^{\circ}$ causes a shift in the through-thickness displacement from right to left, resulting in a decrease in displacement magnitude at the bottom skin and an increase in magnitude at the top skin's outer surfaces for both CG exponents, $n = 0.1$ and 10. However, this change does not affect the non-linear ZZ trend of the displacements in x_2 direction. To present the results more concisely, the upcoming discussions will only depict the results for the CG exponent $n = 0.1$ since the change in the maximum curvilinear fiber angle exhibits similar behavior for both exponents.

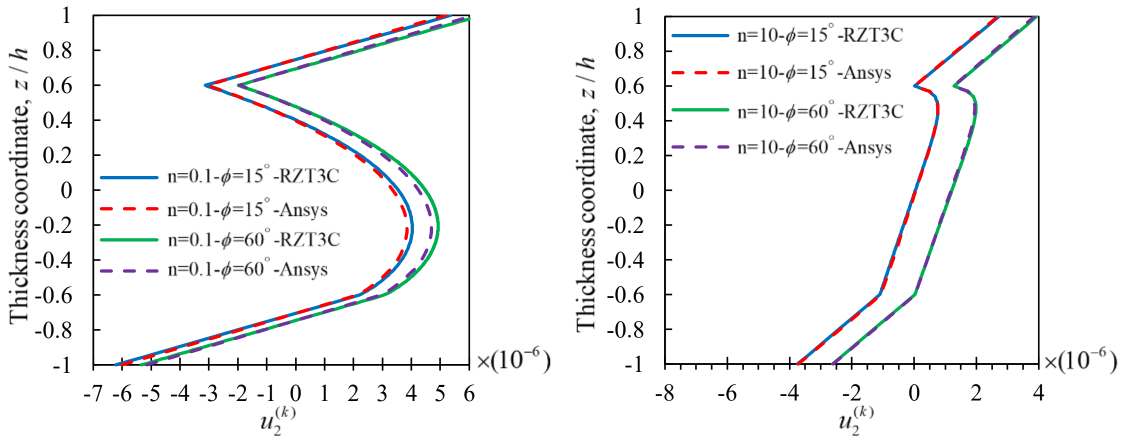

Fig. 4-11 The thickness-wise variation of the in-plane displacement, $u_2^{(k)}$ for the FG-SP for $\phi = 15^\circ, 60^\circ$, and $n = 0.1, 10$.

4.5.5 The curvilinear fiber path influence on the profiles of stresses

Figs. 4-12 and 4-13 show the thickness-wise profiles of the in-plane normal, shear, and transverse shear stresses for curvilinear fiber angle magnitudes of $\phi = 15^\circ$, and $\phi = 60^\circ$, with a CG exponent, $n = 0.1$. Notably, as ϕ increases from 15° to 60°, the in-plane stress in x_1 direction is reduced for the bottom skin, while the opposite effect is observed for the top skin. This behavior is explained by the decreased and increased stiffness due to the spatial curvilinear fiber concentration at the bottom and top skins in x_1 direction, respectively. For a deeper understanding of this mechanical response, the reader may refer to the reference article [6], which contains the curvilinear fiber pattern for the isotropic homogeneous core case of this problem. Fig. 4-12b further shows that the top skin’s spatial concentration of fibers in x_2 direction for both maximum curvilinear fiber angles result in increased stiffness and higher in-plane stress as compared to the bottom skin. In Fig. 4-12b, almost identical through-the-thickness stress distribution for both curvilinear fiber angles reveal the increased overall stiffness of the laminate. Furthermore, as illustrated in Fig. 4-13a, the extreme curvilinear fiber angle magnitude of $\phi = 60^{\circ}$ results in a larger range of in-plane shear stress variation in the upper skin. This behavior is not observed in the lower skin due to higher stiffness of the FG core at its bottom.

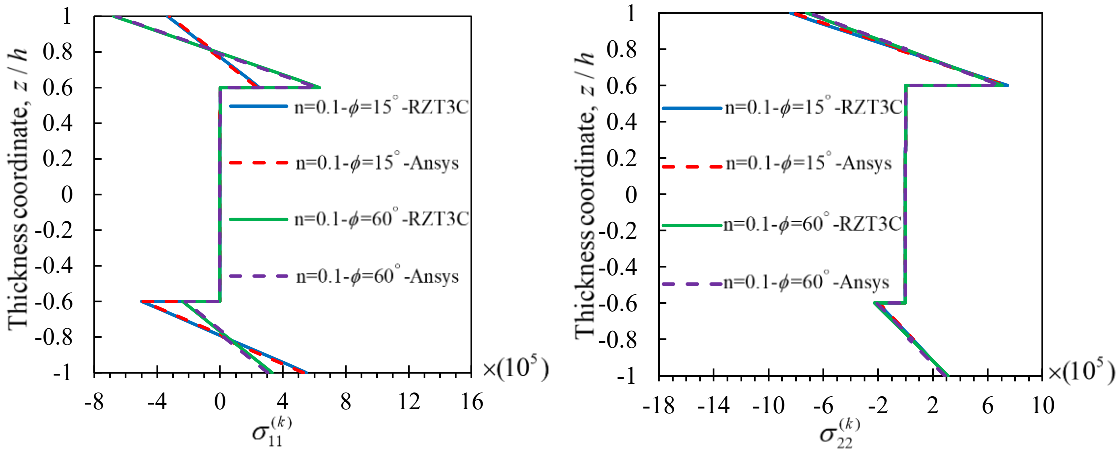

(a) (b)

Fig. 4-12 The thickness-wise variation of the in-plane normal stresses, $\sigma_{11}^{(k)}$ and $\sigma_{22}^{(k)}$, for the FG-SP for $\phi = 15^{\circ}$ and 60°, and $n = 0.1$.

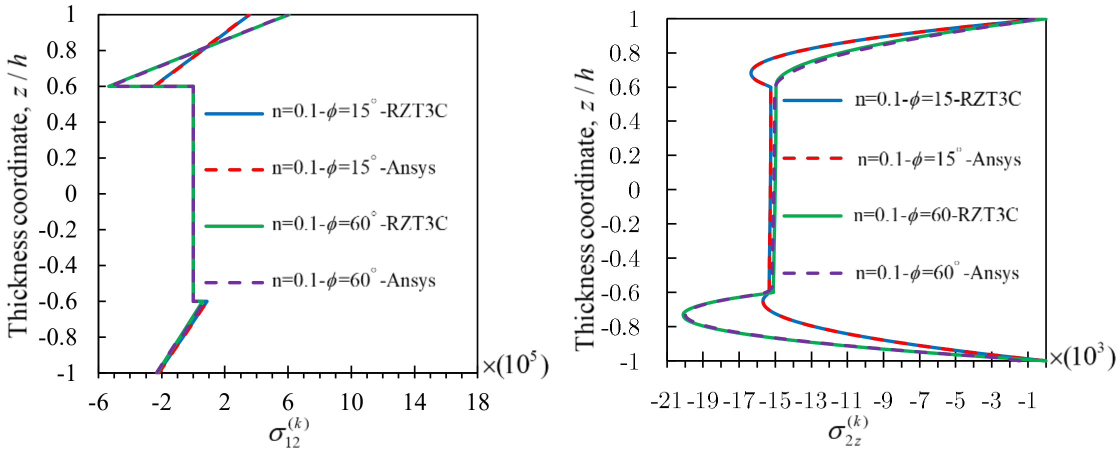

(a) (b)

Fig. 4-13 The thickness-wise variation of the in-plane and transverse shear stresses, $\sigma_{12}^{(k)}$ and $\sigma_{2z}^{(k)}$, for the FG-SP for $\phi = 15^{\circ}$ and 60°, and $n = 0.1$.

For both magnitudes of the curvilinear fiber angle, the transverse shear stress variation exhibits no change in the soft FG material core due to shear stress absorption (Fig. 4-13b). However, the different patterns of the curvilinear fibers have resulted in reflection asymmetry of the transverse shear stress with a greater magnitude in the bottom. It is seen that as the magnitude of fiber angle increases, the gradient of fiber angle becomes larger and greater asymmetry is observed therein. Therefore, it is critical to tailor the stress fields in the plies and interlaminar space of the FG-SPs to prevent failure, as extensively discussed in this thesis. The low-order enhanced RZT3C formulation demonstrates exceptional accuracy in capturing the effects of both the curvilinear fiber path and material gradation, generating identical thickness-wise distributions of stresses, as the 3D continuum elements.

4.6 A three-layer fully clamped circular SP: FG material core with curvilinear fiber reinforced skins

The fourth case considers a three-layer circular FG material core SP with orthotropic VS face sheets. The plate has a specified radius of $r_0 = 0.5\,[m]$ and a total thickness of $2h = 0.05$, resulting in span-to-thickness ratio of $r_0/2h = 10$. Both skins are of the same thickness with $2h_s = 0.01m$, and the thickness of the FG material core is defined with $2h_c = 0.03m$. The skins are composed of glass fiber-reinforced epoxy, and the core is made of two distinct components similar to the FG material soft core in the previous problem. Specifically, the elasticity modulus of the FG material core is graded along its thickness, with elasticity modulus values at the top and bottom equal to those in the preceding case study problem. The through-the-thickness variation of the mechanical properties of the FG material core is similarly governed by the power-law used in the previous test cases. To achieve VS in the face sheets of the laminate, fibers' orientation is determined through the following mathematical relation.

$$\theta^{(1)} = \phi \sin\left(\pi\left(r\cos\left(\theta\right) + 0.5\right) + 0.5\right),\ \theta^{(3)} = \theta^{(1)} + 90 \tag{4.9}$$

where the polar coordinate system is positioned at the centroid of the circular SP, and $\theta^{(1)}$, and $\theta^{(3)}$ are representing the fiber orientation within the bottom and top skins respectively. The symbol ϕ, as in the previous problem, represents the maximum curvilinear fiber angle magnitude and takes the same values. The laminate is subjected to uniform sinusoidal transverse pressure based on the following relation:

$$q = q_0 \sin\left(\frac{\pi}{2}\left|\frac{r - r_0}{r_0}\right|\right) \tag{4.10}$$

where the magnitude is defined as $q_0 = 10\,[KPa]$. Eight distinct cases are investigated by altering the magnitude of the curvilinear fiber angle for the different CG exponent values of the soft FG and constant elastic modulus isotropic cores. Fig. 4-14 concisely depicts the curvilinear patterns of the fibers in the skins of the circular SP for the extreme values of $\phi = 15^\circ$, and $\phi = 60^\circ$ for clarity.

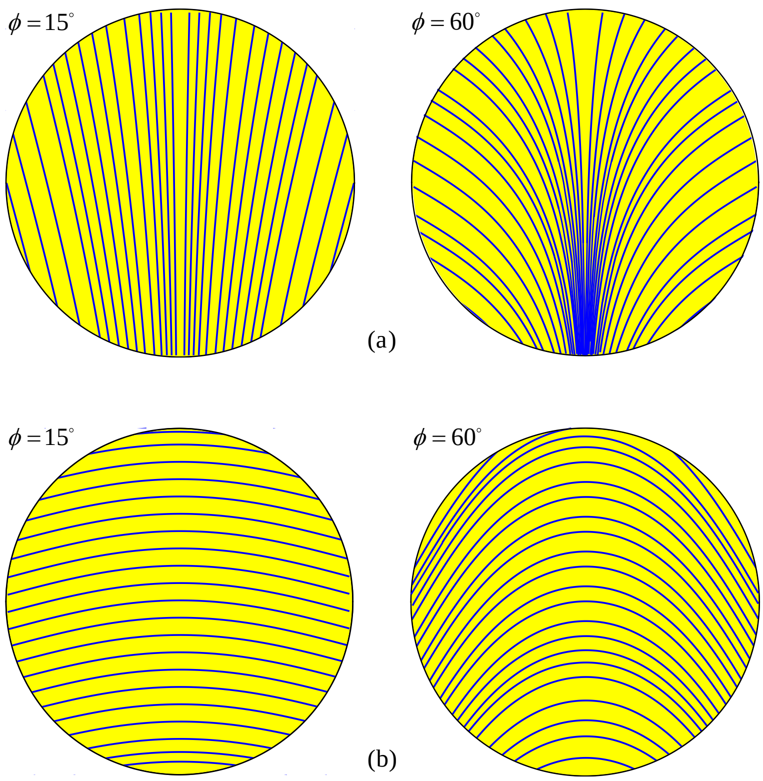

Fig. 4-14 Different variations of fibers' patterns in both the (a) top and (b) bottom skins of the circular FG-SP.

The thickness-wise variations of displacements and stresses are computed at the position of $(r, \theta) = (0.25\,[m], 45^\circ)$. For brevity, the results for the curvilinear fiber angle magnitude of $\phi = 15^\circ$ versus different CG exponents of the FG core will be presented first. Subsequently, to investigate the impact of changing the magnitude of the curvilinear fiber angle, the CGI will be kept constant at $n = 10$ for varying curvilinear fiber angle magnitude of $\phi = 15^\circ$, and $\phi = 60^\circ$.

4.6.1 The effect of FG core's compositional gradient on displacements

Fig. 4-15 compares the thickness-wise variation of displacement components for different n values of the FG core and isotropic homogenous soft core with $\phi = 15^\circ$. Consistent with the previous problem, Figs. 4-15a and b show that that in-plane displacements vary non-linearly along the thickness for the FG core with non-zero values of n and unequal elastic modulus at cores bottom and top. However, the constant value of the elastic modulus in the core (isotropic soft core) results in a linear profile of variation. Moreover, the increased stiffness of the FG core reduces the extent of the non-linearity in thickness-wise variation of in-plane displacements in the core, which is associated with the fact that stiff core resists bending deformation. Thus, the physical position of the neutral plane experiences a smaller shift. It is observed that the magnitude of in-plane displacements is higher for the skins because of being placed far from the neutral plane and naturally experiencing more bend deformation. Nonetheless, the increase in the stiffness of the FG core reduces the magnitude of deformation in the outer surfaces of the skins.

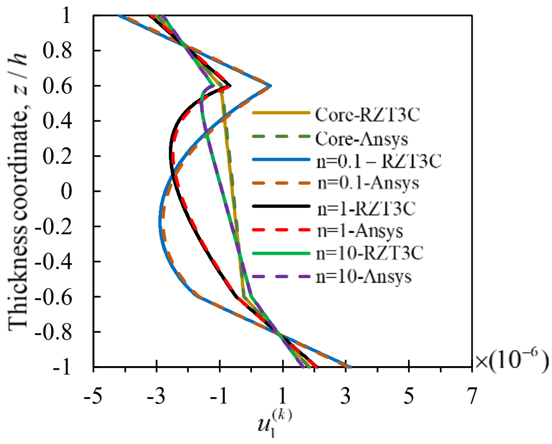

(a)

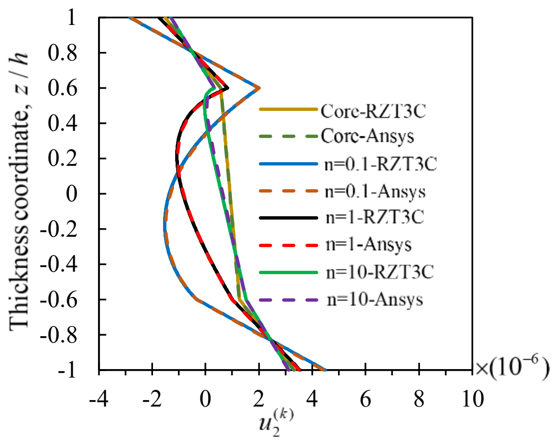

(b)

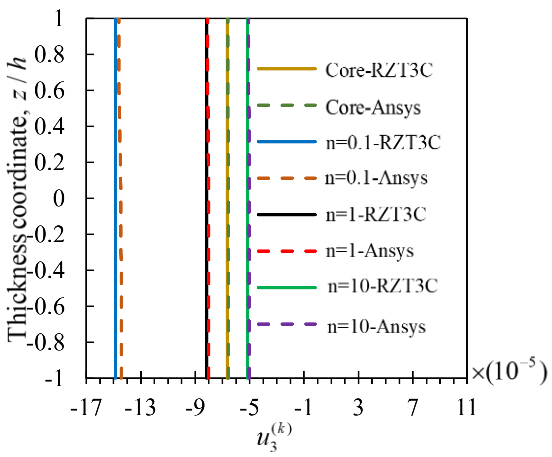

(c)

Fig. 4-15 The thickness-wise variation of the in-plane, and transverse displacements, $u_1^{(k)}, u_2^{(k)}$ and $u_3^{(k)}$, for the circular FG-SP for $\phi = 15^\circ$.

In Figs. 4-15a and b, the stiffer FG core at the bottom results in a smoother transition of in-plane displacements at its interface with the bottom skin owing to the gradual transition of stiffness. This can mitigate the displacement difference between the adjacent layers of FG composite structures during bending. In Fig. 4-15c, the thickness-wise variation of the transverse deflection of the FG-SP is shown. The results indicate that for $n = 0.1$ and $n = 1$, the FG core is softer than the isotropic homogeneous core, whereas for $n = 10$, it is stiffer and bends less. The consistency between the linear and constant transverse deflection variations obtained by the enhanced RZT3C formulation and 3D solid FEM analysis provides two important remarks. For sandwich structures with moderately thick and soft FG material cores, the inclusion of higher-order and stretching terms in the kinematic fields is not necessary. The efficiency and accuracy of the enhanced RZT3C model is not affected by the change of geometry of the laminate.

4.6.2 The effect of FG core's compositional gradient on stresses

Fig. 4-16 presents the variation of in-plane normal, shear, and transverse shear stresses for the circular SP along the thickness direction. Fig. 4-16a shows that when the core is linearly graded along its thickness, $n = 1$, there is a minor increase in the normal in-plane stress value on the outer surfaces of both skins. This increase is attributed to the weaker resistance of softer FG material core against bending than the homogeneous isotropic one. Additionally, the interlaminar stress between the core and the top skin increases for $n = 1$ whereas the one between the core and the bottom skin decreases down to nearly zero. This reduction in the interlaminar stress can be explained such that in the bottom face sheet, fibers are mainly aligned along the x_1 direction. Thus, the stiffness of the bottom skin approaches that of the FG core at their interface (pure epoxy stiffness). Furthermore, the thickness-wise stress variation in all graphs of Fig. 4-16 is unequal for the bottom and top skins for all n values. For instance, in Fig. 4-16a, the variation of the in-plane stress in x_2 direction is greater for the top skin than the bottom skin regardless of the core being an isotropic or an FG material. This disparity is due to the asymmetry in the spatial gradient of curvilinear fibers in both VS skins, which affects the stiffness. In Fig. 4-16b it is demonstrated that increasing n from 0.1 to 10 results in a decrease in the magnitude of the in-plane stress in the core-skins interface, and the skins. This behavior is associated with the increased stiffness of the FG core, leading to a reduced bending deformation. However, as seen in Fig. 4-16c, increasing n does not always consistently result in a reduction in the value of the stress variation. The exponent $n = 10$ almost gives identical in-plane stress variation as that of $n = 0.1$ in the upper skin-core interface and skin, and only causes a reduction in the values of the shear stress at the bottom skin-core interface and skin. This response relates to the redistribution of the loads due to the increased stiffness of skins which makes various CG profiles of the core less significant for this case. The extent to which an increased stiffness in one skin in a specific direction can affect the redistribution of loads depends on the loading conditions and the structural geometry of the laminate.

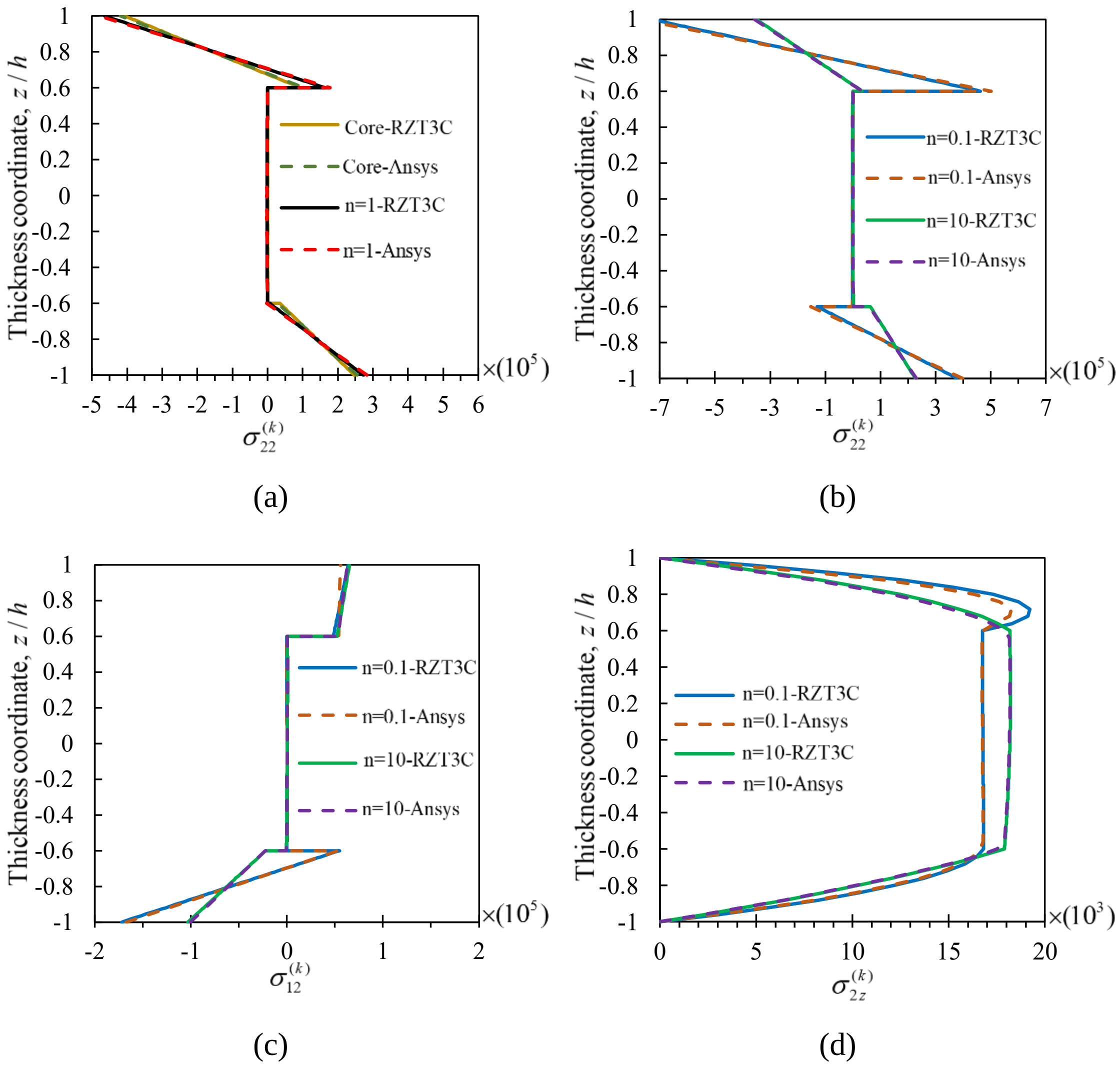

Fig. 4-16 The thickness-wise variation of the planar normal and shear stresses, $\sigma_{22}^{(k)}$ and $\sigma_{12}^{(k)}$, and transverse shear stress, $\sigma_{2z}^{(k)}$, for the circular FG-SP for $\phi = 15^\circ$.

As a result, this observation highlights the potential limitations of using stiffer FG cores, which may not always adequately reduce the stress in the desired VS skin(s) in equilibrium with other stresses. Therefore, there exists a persisting requirement for a reliable and accurate analysis tool such as the enhanced RZT3C formulation. Fig. 4-16d shows the thickness-wise distribution of the transverse shear stress for CGIs of $n = 0.1$, and 10. As is seen, by increasing n from 0.1 to 10, the magnitude of the transverse stress in the FG core and the core-skin interfaces increases owing to the increased stiffness of the core. For $n=10$, the stiff FG core bears the bending deformation and uniformly transmits the transverse shear stress, leading to a reflection symmetry in transverse shear stress. However, for $n=0.1$, the profile of stiffness gradient of the FG core in the thickness direction affects the load transfer mechanism and distribution of stresses within the SP. This gives rise to a stress peak in the upper skin. It is worth noting that all structural analysis results of enhanced RZT3C and 3D solid elements are in good agreement for the non-rectangular FG-SPs as well.

4.6.3 The effect of curvilinear fiber path on stresses

To investigate the effect of curvilinear fiber path on stresses, Fig. 4-17 presents the thickness-wise variation of the in-plane normal, shear, and transverse shear stresses, for the circular FG-SP for $n=10$ and fiber angle magnitudes of $\phi=15^{\circ}$, and 60°. As shown in Fig. 4-17a, by increasing ϕ from 15° to 60°, the in-plane stress values at the outer surfaces of both skins as well as the skin-core interfaces shift due to the change in the stiffness of the skins. That is, the increased spatial concentration of fibers in the x_1 direction for the top skin leads to lesser strain and in turn lowers the stress variation in this direction. As for the bottom skin, the opposite behavior is observed. In Fig. 4-17b, by shifting from $\phi=15^{\circ}$ to 60°, the in-plane stress values at outer surfaces of the top and bottom skins decreases and increases respectively because of the decreased and increased stiffness as the magnitude of the curvilinear fiber angle increases. However, this shift only reduces the interlaminar stress value between the upper skin and the core, with almost no change in the bottom core-skin interface. This behavior is associated with the stiffer bottom of the FG core and increased stiffness of the lower skin in x_2 direction. Fig. 4-17c yields the thickness-wise variation of the in-plane shear stress for fiber orientation magnitudes of $\phi=15^{\circ}$ and $\phi=60^{\circ}$. It is seen that as ϕ rises, the magnitude of the shear stress between the FG material core and the skins increases. Additionally, the rise in the fiber angle magnitude escalates the shear stress within the bottom skin whereas it decreases the shear stress for the top skin towards the outer surface. Evidently, the contrasting increase in the stiffnesses of the top and bottom skins in x_1 and x_2 directions redistribute the shear stress to maintain the equilibrium state in the FG-SP.

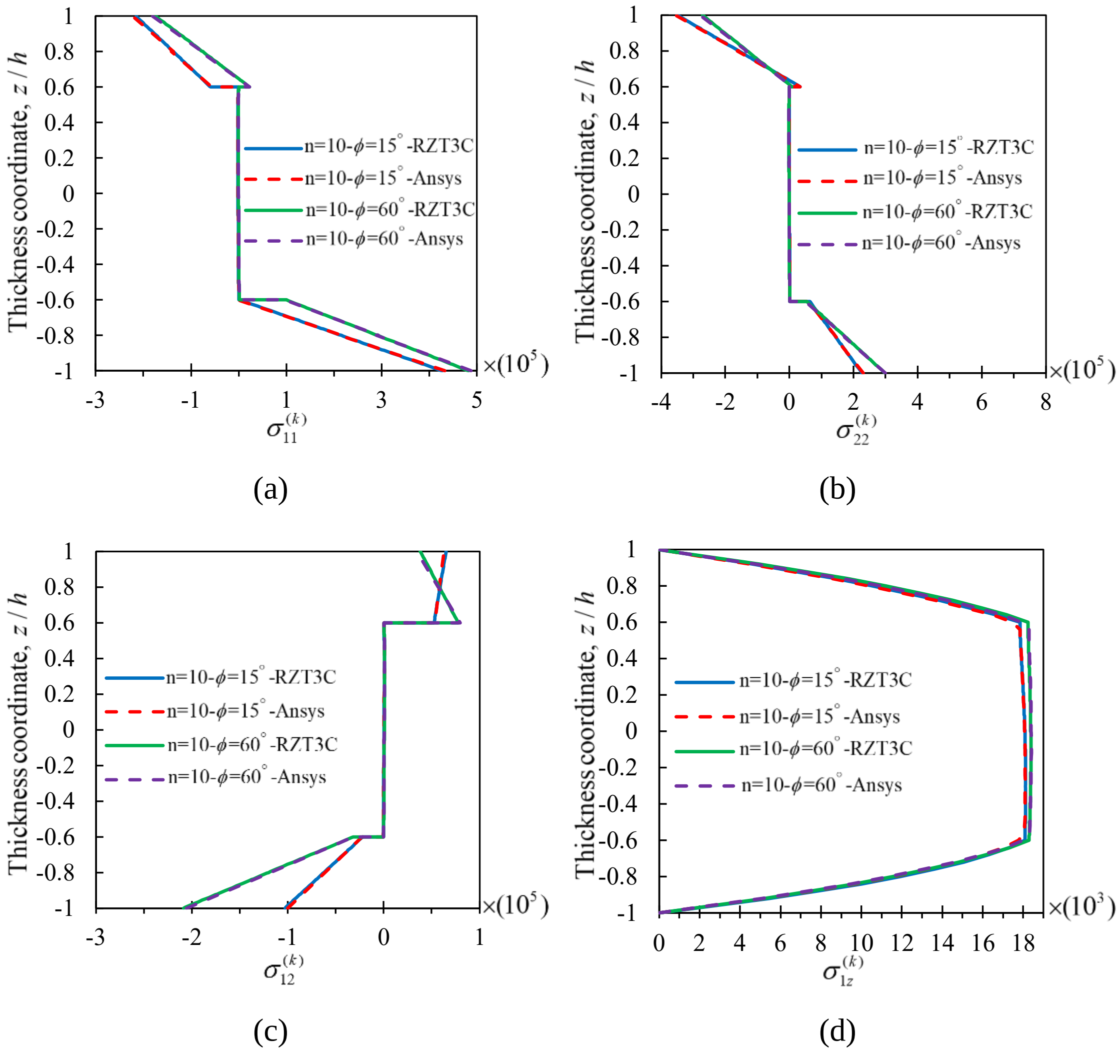

Fig. 4-17 The thickness-wise variation of the in-plane normal and shear stresses, $\sigma_{11}^{(k)}$, $\sigma_{22}^{(k)}$ and $\sigma_{12}^{(k)}$, and the transverse shear stress, $\sigma_{1z}^{(k)}$, for the circular FG-SP with $n=10$.

Notably, for $\phi=15^{\circ}$, the in-plane shear stress has much smaller thickness wise gradient. Fig. 4-17d, shows the thickness-wise variation of transverse shear stresses for fiber angle magnitudes of $\phi=15^{\circ}$ and 60°. As seen, the thickness-wise profiles of the transverse shear stresses are not notably affected by the change in fiber angle magnitude. This is because the thick and stiff FG core ($n=10$) effectively withstands the bending load and thus, the FG-SP does not undergo significant bending deformation in the skins. Essentially, the effect of change in fiber angle magnitude on transverse shear stresses is obscured. According to what has been discussed so far, modifying the material gradation and/or fiber orientation can allow for the desired strain/stress distribution in multiple directions of the FG core composite SPs with VS skins. To control the specified parameters, a robust analytical formulation with the admissible accuracy level and computing efficiency is required. The enhanced RZT3C for FG material laminates is an efficient and precise ESL method capable of computing strains and stresses of multi-ply FG composite sandwich structures, combining the curvilinear fibers, and FG material plies to obtain the most preferable properties.

5 SUMMARY AND CONCLUSIONS

VSCLs and FG material systems are usually tailored to present admissible mechanical properties while preserving the integrity during their lifetime. Obtaining optimally tailored VSCLs and FG material structures necessitates the use of accurate and computationally efficient modeling approaches. Therefore, the present thesis focuses on the development and evaluation of a numerical tool that is accurate and computationally efficient for the structural modeling of VSCLs and FG materials. To this end, the RZT which employs a small number of kinematic variables (seven) is adopted as the foundation of this research. In this study, a single layer model based on revising and reformulating the original RZT formulation is presented to dramatically reduce the computational cost without losing numerical accuracy. In the model for incorporating the curvilinear fiber angle variation in the VS layers, the in-plane derivatives of the ZZ functions are considered in the calculation of strains. Also, to add to the capability of the model to effectively evaluate the thickness-wise distribution of displacements and stresses of FG-SPs, with FG cores/layers and VS skins, the formulation of the model is enhanced to incorporate linear/non-linear ZZ functions. To the purpose of this enhancement, the RZT ZZ functions in the model with incorporation of curvilinear fibers, are upgraded to account also for continuous thickness-wise variation of the FG materials in the FG layers. Furthermore, in this study a three-node shear-locking free triangular FE (RZT3C) is developed in an in-house MATLAB code for the static analysis of thin and moderately thick laminated composite plates and FG-SPs accommodating straight/curvilinear fibers and FG materials in their layers/skins. This element is implemented for the first time in literature for curvilinear FRCs and multilayered FG material structures.

To investigate the capability of the proposed approach for predicting displacements and stresses throughout the 3D laminates, several benchmark problems with different geometries, lamination sequences, materials, curvilinear fiber paths, and grading profiles of FG material are analyzed. The computed results by RZT3C formulation are carefully compared against the numerical solutions of higher-order plate theories available in literature as well as those of the 3D FE implementation. According to the numerical results, the following conclusions can be drawn:

- The proposed enhancements in the RZT formulation promote the model to be capable of analyzing plate structures with UD or curvilinear fiber reinforcements, as well as functionally graded material properties in the in/out of plane directions for the separate or same layer(s).
- The proper selection of the right curvilinear fiber path as well as the grading profile or the combination of the two can mitigate the undesirable mechanical properties in the composites and sandwich laminates with VS/FG layers to be more stable.
- The proposed model with the RZT3C element is an essential, effective, and robust tool due to the utilization of linear thickness-wise expansion for the kinematics model for the in-plane displacements and a constant one for transverse deflection.
- Due to using the RZT as the baseline, the developed model is also consistent with the virtual work principle. This principle directly yields equilibrium equations and boundary conditions.
- The kinematic variables of the proposed model with the RZT3C element are independent of the number of layers in the laminate. As a result, it has a consistent computational cost and efficiency. However, this does not hold true for 3D solid and LW elements and becomes larger with the increase in the number of layers.
- Based on the accurate results obtained without the use of any shear correction factors, the contribution of the ZZ functions to the kinematics, as well as their derivatives to the strain-displacement relations, serve to reach the same level of accuracy as those of higher-order kinematics, LW, or other counterpart theories.
- For multilayered composite and SPs with FG layers, the continuous non-linear ZZ functions account locally for cross-section distortions when coupled by the amplitudes. Therefore, the model can capture the non-linear piecewise distributions of in-plane displacements with linear thickness-wise expansion kinematics in the absence of higher-order terms.
- The model due to relying on RZT kinematics is suitable to be efficiently implemented as an C^0 FEM method with shear-locking free elements such as RZT3C and avoids predicting faulty over-stiff behavior during bending of laminates with VS/FG layers.
- Compared to elements with four or more nodes, with its seven degrees of freedom per node, the 3-node triangular element minimizes the size of the global stiffness

matrix and force vector employed in FEM solution. As a result, the implementation of RZT3C element becomes computationally simpler.

- Consistent with kinematic assumptions of RZT theory, the presented model lacks the C^0 continuity condition for transverse shear stresses, τ_{1z}, τ_{2z} at layers' interfaces, and offers only piecewise average values of these stresses within each layer of the laminate along the thickness direction. To address this issue, continuous transverse shear stresses are reconstructed in a posteriori stress recovery technique by employing Cauchy's equilibrium equations. Upon the utilization of this technique for thin and moderately thick laminates with curvilinear fibers and/or FG material layers, accurate results for the distribution of transverse shear stresses are obtained even with the employment of linear expansion of the kinematics, with RZT3C element.
- The major weakness of the model lies in its lack of higher-order kinematic terms. As a result, the present approach captures physically non-linear displacements as linear for highly thick curvilinear fiber-reinforced composites. For the case of extremely thick FG plates, albeit the consideration of non-linear ZZ functions, the model might erroneously capture the non-linear variations of displacements along the thickness of FG-SPs. Hence, the formulation of the presented model needs to be extended to enable observing accurate nonlinear variations of the displacement throughout the thickness of highly thick VSCL and FG laminated structures. Nonetheless, even in the presence of this limitation the presented model with the RZ3C element can by far effectively and accurately predict the global response of the structure on an average basis.

In light of the concluding remarks above, the presented model in this study with the RZT3C element performs as a viable structural composite and FG material modelling platform and it can be conveniently implemented in commercial FE analysis software packages. This implementation is essential for effectively analyzing displacement, strain, and stresses during the optimization process of laminated composites and sandwich structures containing curvilinear fiber pattern as well as the FG material in their layers. Therefore, the utilization of the present model with the RZT3C element can serve to be replaced by other complex higher-order methods in the literature. This is essential to optimally find the most suitable curvilinear fiber path and grading profiles of materials for the VSCLs and FG laminated structures to increase their stiffness-to-weight ratio.

6 FURTURE WORK

As for the future work, the following is briefly the list of possible research which can be conducted by using the current study as the base.

- The employment of the proposed model to an optimization platform such as the genetic algorithm to obtain the most suitable VS/FG design parameters. This is important to achieve high-performance multi-stable structures without failure, especially in that the non-uniform stress distribution should be steered with curvilinear fibers and/or FG material.
- The implementation of the proposed model for vibration and structural analysis of multi-layered VS and FG shell and stiffened structures and conducting accuracy analysis for various plate and shell elements.
- The incorporation of the isogeometric formulation to the proposed formulation to ensure the continuity of the curvilinear fiber path based on non-uniform rational spline interpolation functions (NURBS) as one of the significant manufacturing constraints of the VSCLs.
- The enhancement of the model by integrating a global stochastic model capable of probabilistic characterization of local defects along with a scaling technique to scale the properties of the defect area (local deterministic approach). This way gaps and overlaps and fiber misalignments in VSCLs, and material imperfections and porosity type defects in FG structures can be readily analyzed.
- The adoption of the RZT(m) formulation to the presented model to avoid the posteriori analysis step for obtaining the continuous non-linear distribution of the transverse shear stresses along the thickness of the laminate.
- The incorporation of non-linear Von Karman governing equations into the model in order to broaden the model's analysis span to geometric non-linearities in buckling and post-buckling analyses.
- The study of damped and free vibration of plate structures with the inclusion of VS, FG, and piezoelectric actuators embedded layers in the first step and extending the study to micro-plates.
- The implementation of the higher-order RZT theory to the proposed model to specifically attain accurate results for structural analysis of extremely thick VS and FG composite structures.

APPENDIX A

Herein, the elimination process of the mid-nodes (constrained) of the six-node RZT triangle element, shown in Fig. A.1, has been rederived for completeness.

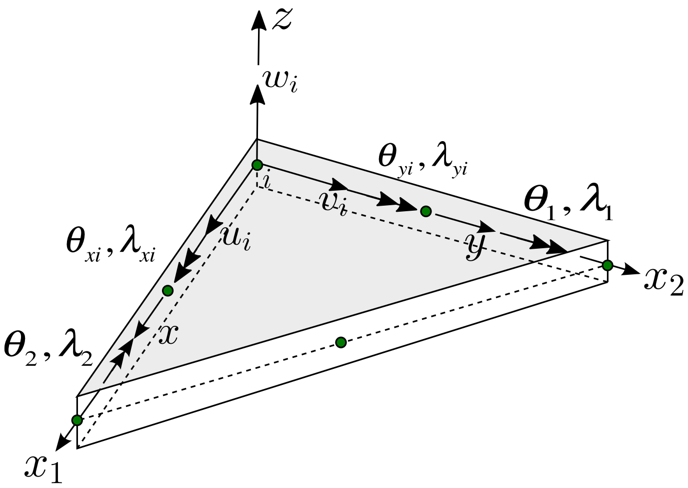

Fig. A.1 The six-node RZT triangle element.

$$u_1^{(k)}(\mathbf{x}, z) = u(\mathbf{x}) + z\theta_1(\mathbf{x}) \quad \text{(A.1)}$$

$$u_2^{(k)}(\mathbf{x}, z) = v(\mathbf{x}) + z\theta_2(\mathbf{x}) \quad \text{(A.2)}$$

$$\mathrm{u}_z(\mathbf{x}, z) = w \quad \text{(A.3)}$$

The set of FSDT kinematic relations in Eqs.(A.1)-(A.3) were enhanced by including the contribution of ZZ functions and their amplitudes as shown in Eqs.(2.1)-(2.3).

$$\theta_1(\mathbf{x}) = \theta_y(\mathbf{x}); \; \lambda_1(\mathbf{x}) = \lambda_y(\mathbf{x}) \quad \text{(A.4)}$$

$$\theta_2(\mathbf{x}) = -\theta_x(\mathbf{x}); \; \lambda_2(\mathbf{x}) = -\lambda_x(\mathbf{x}) \quad \text{(A.5)}$$

From the FSDT Eqs.(A.1)-(A.3), the transverse shear strain can be expressed as:

$$\gamma_{1z} = \frac{\partial w}{\partial x_1} + \frac{\partial u}{\partial z} \equiv \frac{\partial w}{\partial x_1} + \theta_y \quad \text{(A.6)}$$

Based on the RZT kinematics given in Eqs.(2.1)-(2.3), the strain measure η_1 can be defined as,

$$\eta_1 = \gamma_{1z} - \lambda_1 \quad \text{(A.7)}$$

and by replacing Eq.(A.4) and Eq.(A.6) into Eq.(A.7), the strain measure can be rewritten as:

$$\eta_1 = \frac{\partial w}{\partial x_1} + \theta_y - \lambda_y \tag{A.8}$$

Under the assumption of each edge of the 6-node triangle element can be separated into a 3-node bar element, the kinematic variables of the specified element can be interpolated as:

$$\Omega = \Omega_i \ N_i \tag{A.9}$$

$$\Omega = \Omega_1 (\frac{1}{2}\xi(\xi - 1)) + \Omega_2 (\frac{1}{2}\xi(\xi + 1)) + (1 - \xi^2)\Omega_{m12} \tag{A.10}$$

with $[\Omega = (w, \theta_y, \lambda_y),\ i = (1, \cdots, 3)]$ and $i = m_{12} = 3$ refers to the mid-point of the element. The variation of the transverse displacement with respect to x_1-direction in Eqs.(A.6)-(A.8) can be expressed using the chain rule as:

$$\frac{dw}{d\xi} = \xi w^{(1)} - \frac{1}{2} w^{(1)} + \xi w^{(2)} + \frac{1}{2} w^{(2)} - 2\xi w^{(m_{12})} \tag{A.11}$$

with the Jacobian of the isoparametric transformation from cartesian to natural coordinates as:

$$\frac{d\xi}{dx_1} = \frac{2}{L} \tag{A.12}$$

Applying the chain rule, the derivative of the transverse deflection with respect to x_1 axis can be written as:

$$\frac{dw}{dx_1} = \xi \left[\frac{2}{L} (w^{(1)} + w^{(2)} - 2w^{(m_{12})}) \right] + \frac{(w^{(2)} - w^{(1)})}{L} \tag{A.13}$$

Hence, using Eq.(A.9) and Eq.(A.13) the shear strain measure η_1 in Eq.(A.8) takes the form:

$$\begin{aligned} \eta_1 = & [\frac{(w^{(2)} - w^{(1)})}{L} + (\theta_y^{(m_{12})} - \lambda_y^{(m_{12})})] + \\ & [\frac{2}{L}(w^{(1)} + w^{(2)} - 2w^{(m_{12})}) + \frac{(\theta_y^{(2)} - \theta_y^{(1)} + \lambda_y^{(1)} - \lambda_y^{(2)})}{2}]\xi + \\ & (\frac{\theta_y^{(1)} + \theta_y^{(2)} - 2\theta_y^{(m_{12})} - \lambda_y^{(1)} - \lambda_y^{(2)} + 2\lambda_y^{(m_{12})}}{2})\xi^2 \end{aligned} \tag{A.14}$$

For very thin plates, aspect ratio higher than fifty, the shear strain measure in Eq.(A.14) vanishes and the discrepancy of the rotation functions θ_1, and θ_2 with λ_1, and λ_2 approach the slopes of transverse deflection [72]. Therefore, by setting constant, linear, and quadratic terms of ξ in Eq.(A.14), one can use the values of DOF in the corners' nodal points to express the values of side mid-nodes on the edges of the six-node triangular element. Such a strategy reduces the number of the nodes of the element from six to three and prevents the shear locking problem which occurs by miscalculating the bending curvature between the adjacent elements.

$$\frac{w^{(2)}-w^{(1)}}{L}=\lambda_y^{(m_{12})}-\theta_y^{(m_{12})} \tag{A.15}$$

$$w^{(m_{12})}=\frac{w^{(1)}+w^{(2)}}{2}+\frac{L_1^{(e)}}{8}[(\theta_y^{(2)}-\theta_y^{(1)})-(\lambda_y^{(2)}-\lambda_y^{(1)})] \tag{A.16}$$

and,

$$\theta_y^{(m_{12})}-\lambda_y^{(m_{12})}=\left(\frac{\theta_y^{(1)}+\theta_y^{(2)}-(\lambda_y^{(1)}+\lambda_y^{(2)})}{2}\right) \tag{A.17}$$

with $L_1^{(e)}=x_1^{(2)}-x_1^{(1)}$. If the same procedure from Eqs.(A.6)-(A.17) is repeated for the other direction by defining γ_{2z}, and η_2, the mid-node transverse deflection, $w^{(m_{13})}$ can be expressed as:

$$w^{(m_{13})}=\frac{w^{(1)}+w^{(3)}}{2}+\frac{L_2^{(e)}}{8}[(\theta_x^{(1)}-\theta_x^{(1)})-(\lambda_x^{(1)}-\lambda_x^{(3)})] \tag{A.18}$$

with $L_2^{(e)}=x_2^{(1)}-x_2^{(3)}$. By comparing Eq.(A.16) and Eq.(A.18), the general form of the transverse deflection of the side mid-points of the six-node triangular can be expressed in terms its values on the corner nodes as:

$$\begin{aligned} w^{(m_{ab})}=\frac{w^{(a)}+w^{(b)}}{2}+\frac{(x_1^{(b)}-x_1^{(a)})}{8}[(\theta_y^{(b)}-\theta_y^{(a)})-(\lambda_y^{(b)}-\lambda_y^{(a)})] \\ -\frac{(x_2^{(b)}-x_2^{(a)})}{8}[(\theta_x^{(b)}-\theta_x^{(a)})-(\lambda_x^{(b)}-\lambda_x^{(a)})] \end{aligned} \tag{A.19}$$

The transverse displacement field of the six-node triangular element can be interpolated using the area parametric coordinates and quadratic shape functions as:

$$w=w_i\,N_i \quad , \ (i=1,\cdots,6) \tag{A.20}$$

$$\begin{aligned} w=\left[(2L_1-1)L_1\right]w_1+\left[(2L_2-1)L_2\right]w_2+\left[(2L_2-1)L_3\right]w_3+\cdots \\ \cdots+(4L_1L_2)w_{m_{12}}+(4L_2L_3)w_{m_{23}}+(4L_3L_1)w_{m_{31}} \end{aligned} \tag{A.21}$$

Substituting Eq.(A.19) into Eq.(A.21), and applying the condition $L_1 + L_2 + L_3 = 1$, the anisoparametric constrained form of the transverse displacement field can be written in terms of the corner node kinematic variables as:

$$w = \sum_{i=1}^{3} [w_i L_i - (\theta_{xi} - \lambda_{xi}) L_{1i} + (\theta_{yi} - \lambda_{yi}) L_{2i}] \tag{A.22}$$

Thereby, the linear anisoparametric shape function matrix of the three-node constrained RZT element, takes the form below:

$$\mathbf{N}_i^{(e)} \equiv \begin{bmatrix} L_i & 0 & 0 & 0 & 0 & 0 & 0 \\ 0 & L_i & 0 & 0 & 0 & 0 & 0 \\ 0 & 0 & L_i & -L_{1i} & L_{2i} & L_{1i} & -L_{2i} \\ 0 & 0 & 0 & 0 & L_i & 0 & 0 \\ 0 & 0 & 0 & -L_i & 0 & 0 & 0 \\ 0 & 0 & 0 & 0 & 0 & 0 & L_i \\ 0 & 0 & 0 & 0 & 0 & -L_i & 0 \end{bmatrix} \tag{A.23}$$

and the strain-displacement matrix, $\mathbf{B}_i^{(e)}$ associated with the three-node constrained anisoparametric triangle RZT element $(i = 1, ..., 3)$ is defined with the shape functions' derivatives of the element with respect to the planar coordinates, $\mathbf{x}$, as Eq.(A.24) where L_i , L_{1i} , L_{2i} are the shape functions of the three-node RZT element given in Ref.[89], and the operators, $(\bullet)_{,i} \equiv \partial(\bullet)/\partial x_i$ $(i = 1, 2)$, represent the partial derivatives in the planar coordinate directions, x_1 and x_2.

$$
\mathbf{B}_i^{(e)} \equiv \begin{bmatrix}
L_{i,1} & 0 & 0 & 0 & 0 & 0 & 0 \\
0 & L_{i,2} & 0 & 0 & 0 & 0 & 0 \\
L_{i,2} & L_{i,1} & 0 & 0 & 0 & 0 & 0 \\
0 & 0 & 0 & 0 & L_{i,1} & 0 & 0 \\
0 & 0 & 0 & -L_{i,2} & 0 & 0 & 0 \\
0 & 0 & 0 & -L_{i,1} & L_{i,2} & 0 & 0 \\
0 & 0 & 0 & 0 & 0 & 0 & L_{i,1} \\
0 & 0 & 0 & 0 & 0 & -L_{i,2} & 0 \\
0 & 0 & 0 & 0 & 0 & 0 & L_{i,2} \\
0 & 0 & 0 & 0 & 0 & -L_{i,1} & 0 \\
0 & 0 & L_{i,1} & -L_{1i,1} & L_{2i,1}+L_i & L_{1i,1} & -L_{2i,1} \\
0 & 0 & L_{i,2} & -L_i - L_{1i,2} & L_{2i,2} & L_{1i,2} & -L_{2i,2} \\
0 & 0 & 0 & 0 & 0 & 0 & L_i \\
0 & 0 & 0 & 0 & 0 & -L_i & 0
\end{bmatrix} \tag{A.24}
$$

REFERENCES

1. Yashas Gowda, T. G., Sanjay, M. R., Subrahmanya Bhat, K., Madhu, P., Senthamaraikannan, P., & Yogesha, B. (2018). Polymer matrix-natural fiber composites: An overview. Cogent Engineering, 5(1), 1446667.
2. Sherif, G., Chukov, D., Tcherdyntsev, V., & Torokhov, V. (2019). Effect of formation route on the mechanical properties of the polyethersulfone composites reinforced with glass fibers. Polymers, 11(8), 1364.
3. Rajak, D. K., Pagar, D. D., Menezes, P. L., & Linul, E. (2019). Fiber-reinforced polymer composites: Manufacturing, properties, and applications. Polymers, 11(10), 1667.
4. Chukov, D., Nematulloev, S., Torokhov, V., Stepashkin, A., Sherif, G., & Tcherdyntsev, V. (2019). Effect of carbon fiber surface modification on their interfacial interaction with polysulfone. Results in Physics, 15, 102634.
5. Chukov, D., Nematulloev, S., Zadorozhnyy, M., Tcherdyntsev, V., Stepashkin, A., & Zherebtsov, D. (2019). Structure, mechanical and thermal properties of polyphenylene sulfide and polysulfone impregnated carbon fiber composites. Polymers, 11(4), 684.
6. Hasim, K. A., & Kefal, A. (2021). Isogeometric static analysis of laminated plates with curvilinear fibers based on Refined Zigzag Theory. Composite Structures, 256, 113097.
7. Chung, D. D. (2010). Tailoring Composite Materials. Composite Materials: Science and Applications, 157-201.
8. Dirk, H. J. L., Ward, C., & Potter, K. D. (2012). The engineering aspects of automated prepreg layup: History, present and future. Composites Part B: Engineering, 43(3), 997-1009.
9. Kim, B. C., Weaver, P. M., & Potter, K. (2015). Computer aided modelling of variable angle tow composites manufactured by continuous tow shearing. Composite Structures, 129, 256-267.
10. Santarpia, E. (2020). A variable kinematic model for large deflection of functionally graded variable-stiffness composite laminates. University of California, San Diego.

11. Rivera, M. G., & Reddy, J. N. (2016). Stress analysis of functionally graded shells using a 7-parameter shell element. Mechanics Research Communications, 78, 60-70.
12. Tornabene, F., Fantuzzi, N., Bacciocchi, M., Viola, E., & Reddy, J. N. (2017). A numerical investigation on the natural frequencies of FGM sandwich shells with variable thickness by the local generalized differential quadrature method. Applied Sciences, 7(2), 131.
13. Naghavi, M., Sarrami-Foroushani, S., & Azhari, F. (2022). Bending analysis of functionally graded sandwich plates using the refined finite strip method. Journal of Sandwich Structures & Materials, 24(1), 448-483.
14. Gayen, D., Tiwari, R., & Chakraborty, D. (2019). Static and dynamic analyses of cracked functionally graded structural components: a review. Composites Part B: Engineering, 173, 106982.
15. Reddy, J. N., & Chin, C. D. (1998). Thermomechanical analysis of functionally graded cylinders and plates. Journal of thermal Stresses, 21(6), 593-626.
16. Ganapathi, M., Anirudh, B., Anant, C., & Polit, O. (2021). Dynamic characteristics of functionally graded graphene reinforced porous nanocomposite curved beams based on trigonometric shear deformation theory with thickness stretch effect. Mechanics of Advanced Materials and Structures, 28(7), 741-752.
17. Berggreen, C., & Hayman, B. (2020). Damage tolerance assessment of naval sandwich structures with face-core debonds. Advances in Thick Section Composite and Sandwich Structures: An Anthology of ONR-sponsored Research, 439-483.
18. Setoodeh, S., Abdalla, M. M., & Gürdal, Z. (2006). Design of variable–stiffness laminates using lamination parameters. Composites Part B: Engineering, 37(4-5), 301-309.
19. Murugan, S., & Friswell, M. I. (2013). Morphing wing flexible skins with curvilinear fiber composites. Composite Structures, 99, 69-75.
20. Hao, P., Wang, B., Tian, K., Liu, H., Wang, Y., Niu, F., & Zeng, D. (2017). Simultaneous buckling design of stiffened shells with multiple cutouts. Engineering Optimization, 49(7), 1116-1132.
21. Wang, W., Cheng, G., & Li, Q. (2013). Fast dynamic performance optimization of complicated beam-type structures based on two new reduced physical models. Engineering Optimization, 45(7), 835-850.

22. Tessler, A., Di Sciuva, M., & Gherlone, M. (2010). A consistent refinement of first-order shear deformation theory for laminated composite and sandwich plates using improved zigzag kinematics. Journal of Mechanics of Materials and Structures, 5(2), 341-367.
23. Tessler, A., Di Sciuva, M., & Gherlone, M. (2011). A homogeneous limit methodology and refinements of computationally efficient zigzag theory for homogeneous, laminated composite, and sandwich plates. Numerical Methods for Partial Differential Equations, 27(1), 208-229.
24. Tessler, A., DiSciuva, M., & Gherlone, M. (2007). Refinement of Timoshenko beam theory for composite and sandwich beams using zigzag kinematics (No. L-19411).
25. Tessler, A., & DiSciuva, M. (2010). Refined zigzag theory for homogeneous, laminated composite, and sandwich plates: a homogeneous limit methodology for zigzag function selection (No. NASA/TP-2010-216214).
26. Iurlaro, L., Gherlone, M., Di Sciuva, M., & Tessler, A. (2015). Refined Zigzag Theory for laminated composite and sandwich plates derived from Reissner's Mixed Variational Theorem. Composite Structures, 133, 809-817.
27. Tessler, A., DI SCIUVA, M., & Gherlone, M. (2008). A shear-deformation theory for composite and sandwich plates using improved zigzag kinematics. In Titolo volume non avvalorato (pp. 477-497). BHV Topping Ed., Civil Comp Press.
28. Tessler, A., Di Sciuva, M., & Gherlone, M. (2009). A refined zigzag beam theory for composite and sandwich beams. Journal of Composite Materials, 43(9), 1051-1081.
29. Zhang, Y., Tao, W., Zhang, Y., Tang, L., Gu, J., & Jiang, Z. (2018). Continuous carbon fiber/crosslinkable poly (ether ether ketone) laminated composites with outstanding mechanical properties, robust solvent resistance and excellent thermal stability. Composites Science and Technology, 165, 148-153.
30. Yudhanto, A., Wafai, H., Lubineau, G., Yaldiz, R., & Verghese, N. (2018). Characterizing the influence of matrix ductility on damage phenomenology in continuous fiber-reinforced thermoplastic laminates undergoing quasi-static indentation. Composite Structures, 186, 324-334.

31. Hou, Z., Tian, X., Zhang, J., Zheng, Z., Zhe, L., Li, D., ... & Polilov, A. N. (2021). Optimization design and 3D printing of curvilinear fiber reinforced variable stiffness composites. Composites Science and Technology, 201, 108502.
32. Song, Z., Ni, Y., & Cai, S. (2019). Fracture modes and hybrid toughening mechanisms in oscillated/twisted plywood structure. Acta biomaterialia, 91, 284-293.
33. Liu, J. L., Lee, H. P., & Tan, V. B. C. (2018). Failure mechanisms in bioinspired helicoidal laminates. Composites Science and Technology, 157, 99-106.
34. Quan, H., Yang, W., Schaible, E., Ritchie, R. O., & Meyers, M. A. (2018). Novel defense mechanisms in the armor of the scales of the "living fossil" coelacanth fish. Advanced Functional Materials, 28(46), 1804237.
35. Hao, P., Liu, D., Wang, Y., Liu, X., Wang, B., Li, G., & Feng, S. (2019). Design of manufacturable fiber path for variable-stiffness panels based on lamination parameters. Composite Structures, 219, 158-169.
36. Zhang, H., Yang, D., & Sheng, Y. (2018). Performance-driven 3D printing of continuous curved carbon fibre reinforced polymer composites: A preliminary numerical study. Composites Part B: Engineering, 151, 256-264.
37. Zhu, Y., Liu, J., Liu, D., Xu, H., Yan, C., Huang, B., & Hui, D. (2017). Fiber path optimization based on a family of curves in composite laminate with a center hole. Composites Part B: Engineering, 111, 91-102.
38. Setoodeh, S., Abdalla, M. M., IJsselmuiden, S. T., & Gürdal, Z. (2009). Design of variable-stiffness composite panels for maximum buckling load. Composite structures, 87(1), 109-117.
39. Nair, A. B., & Joseph, R. (2014). Eco-friendly bio-composites using natural rubber (NR) matrices and natural fiber reinforcements. In Chemistry, manufacture and applications of natural rubber (pp. 249-283). Woodhead Publishing.
40. Agarwal, B. D., Broutman, L. J., Agarwal, B. D., & Broutman, L. J. (1990). Analysis and performance of fiber composites Second edition. John Wiley & Sons.
41. Liew, K. M., Pan, Z., & Zhang, L. W. (2020). The recent progress of functionally graded CNT reinforced composites and structures. Science China Physics, Mechanics & Astronomy, 63(3), 234601.
42. Akhavan, H. (2015). Non-linear vibrations of tow placed variable stiffness composite laminates (Doctoral dissertation, Universidade do Porto (Portugal)).

43. Güldü, S. (2014). Analysis and optimization of cylindrical structures manufactured by automated fiber placement technique (Master's thesis, Middle East Technical University).
44. Hirai, T., & Chen, L. (1999, May). Recent and prospective development of functionally graded materials in Japan. In Materials science forum (Vol. 308, pp. 509-514). Trans Tech Publications Ltd.
45. Zhang, N., Khan, T., Guo, H., Shi, S., Zhong, W., & Zhang, W. (2019). Functionally graded materials: an overview of stability, buckling, and free vibration analysis. Advances in Materials Science and Engineering, 2019.
46. Watanabe, Y., & Sato, H. (2011). Review fabrication of functionally graded materials under a centrifugal force. Nanocomposites with unique properties and applications in medicine and industry, 133, 150.
47. Shen, H. S. (2016). Functionally graded materials: nonlinear analysis of plates and shells. CRC press.
48. Chakraverty, S., & Pradhan, K. K. (2016). Vibration of functionally graded beams and plates. Academic Press.
49. Udupa, G., Rao, S. S., & Gangadharan, K. V. (2014). Functionally graded composite materials: an overview. Procedia Materials Science, 5, 1291-1299.
50. Shi, Z. A., & Chen, Y. (2004). Functionally graded piezoelectric cantilever beam under load. Archive of Applied Mechanics, 74(3-4), 237-247.
51. Miyamoto, Y., Kaysser, W. A., Rabin, B. H., Kawasaki, A., & Ford, R. G. (Eds.). (2013). Functionally graded materials: design, processing and applications (Vol. 5). Springer Science & Business Media.
52. Sarangi, S. K. (2021). Modeling and Analysis of Smart Functionally Graded Structures. In Functionally Graded Materials (FGMs) (pp. 139-168). CRC Press.
53. Saleh, B., Jiang, J., Ma, A., Song, D., Yang, D., & Xu, Q. (2020). Review on the influence of different reinforcements on the microstructure and wear behavior of functionally graded aluminum matrix composites by centrifugal casting. Metals and Materials International, 26, 933-960.
54. Pandey, P.M., Rathee, S., Srivastava, M., & Jain, P.K. (Eds.). (2021). Functionally Graded Materials (FGMs): Fabrication, Properties, Applications, and Advancements (1st ed.). CRC Press.

55. Burlayenko, V. N. (2021). A continuum shell element in layerwise models for free vibration analysis of FGM sandwich panels. Continuum Mechanics and Thermodynamics, 33(4), 1385-1407.
56. Gibson, L. J., Ashby, M. F., Karam, G. N., Wegst, U., & Shercliff, H. R. (1995). The mechanical properties of natural materials. II. Microstructures for mechanical efficiency. Proceedings of the Royal Society of London. Series A: Mathematical and Physical Sciences, 450(1938), 141-162.
57. Mori, T., & Tanaka, K. (1973). Average stress in matrix and average elastic energy of materials with misfitting inclusions. Acta metallurgica, 21(5), 571-574.
58. Hill, R. (1965). A self-consistent mechanics of composite materials. Journal of the Mechanics and Physics of Solids, 13(4), 213-222.
59. Nemati, A. R., & Mahmoodabadi, M. J. (2020). Effect of micromechanical models on stability of functionally graded conical panels resting on Winkler–Pasternak foundation in various thermal environments. Archive of Applied Mechanics, 90(5), 883-915.
60. Shen, H. S., & Wang, Z. X. (2012). Assessment of Voigt and Mori–Tanaka models for vibration analysis of functionally graded plates. Composite Structures, 94(7), 2197-2208.
61. Benveniste, Y. (1987). A new approach to the application of Mori-Tanaka's theory in composite materials. Mechanics of materials, 6(2), 147-157.
62. Dai, L. H., Huang, Z. P., & Wang, R. (1998). A generalized self-consistent mori-tanaka scheme for prediction of the effective elastic moduli of hybrid multiphase particulate composites. Polymer composites, 19(5), 506-513.
63. Nemat-Nasser, S., & Hori, M. (2013). Micromechanics: overall properties of heterogeneous materials. Elsevier.
64. Amira, S. A. D. G. U. I. (2022). Modeling of Functionally Graded structures behavior Modélisation du comportement des structures en Matériaux Fonctionnellement Gradués (FGM) (Doctoral dissertation, Faculté des Sciences et de la technologie).
65. Voigt, W. (1889). Ueber die Beziehung zwischen den beiden Elasticitätsconstanten isotroper Körper. Annalen der physik, 274(12), 573-587.
66. Zaidi, M., Joshi, K. K., Shukla, A., & Cherinet, B. (2021, May). A review of the various modelling schemes of unidirectional functionally graded material structures. In AIP Conference Proceedings (Vol. 2341, No. 1). AIP Publishing.

67. Chi, S. H., & Chung, Y. L. (2006). Mechanical behavior of functionally graded material plates under transverse load—Part I: Analysis. International Journal of Solids and Structures, 43(13), 3657-3674.
68. Amandeep, A., & Padhee, S. S. (2018). Analysis of Functionally Graded Cylinders for Different Gradation Law under Coupled Thermo-Mechanical Loading. Asian Journal of Engineering and Applied Technology, 7(S2), 21-25.
69. Wakashima, K., Hirano, T., & Niino, M. (1990). Functionally Gradient Materials(Fgm) Architecture: A New Type of Ceramic-Metal Assemblage Designed for Hot Structural Components.
70. Bao, G., & Wang, L. (1995). Multiple cracking in functionally graded ceramic/metal coatings. International Journal of Solids and Structures, 32(19), 2853-2871.
71. Delale, F., & Erdogan, F. (1983). The crack problem for a nonhomogeneous plane, Journal of Applied Mechanics, 50(3), 609-614.
72. Reddy, J. N. (2003). Mechanics of laminated composite plates and shells: theory and analysis. CRC press.
73. Reissner, E. (1950). On a variational theorem in elasticity. Journal of Mathematics and Physics, 29(1-4), 90-95.
74. Almeida Jr, J. H. S., Bittrich, L., & Spickenheuer, A. (2020). Improving the open-hole tension characteristics with variable-axial composite laminates: Optimization, progressive damage modeling and experimental observations. Composites Science and Technology, 185, 107889.
75. Gürdal, Z., Tatting, B. F., & Wu, C. K. (2008). Variable stiffness composite panels: effects of stiffness variation on the in-plane and buckling response. Composites Part A: Applied Science and Manufacturing, 39(5), 911-922.
76. Blom, A. W., Stickler, P. B., & Gürdal, Z. (2010). Optimization of a composite cylinder under bending by tailoring stiffness properties in circumferential direction. Composites Part B: Engineering, 41(2), 157-165.
77. Huang, J., & Haftka, R. T. (2005). Optimization of fiber orientations near a hole for increased load-carrying capacity of composite laminates. Structural and Multidisciplinary Optimization, 30, 335-341.
78. IJsselmuiden, S., Abdalla, M., Setoodeh, S., & Gürdal, Z. (2008). Design of variable stiffness panels for maximum buckling load using lamination parameters. In 49th AIAA/ASME/ASCE/AHS/ASC Structures, Structural Dynamics, and

Materials Conference, 16th AIAA/ASME/AHS Adaptive Structures Conference, 10th AIAA Non-Deterministic Approaches Conference, 9th AIAA Gossamer Spacecraft Forum, 4th AIAA Multidisciplinary Design Optimization Specialists Conference (p. 2123).

79. Hyer, M. W. (1982). The room-temperature shapes of four-layer unsymmetric cross-ply laminates. Journal of Composite Materials, 16(4), 318-340.

80. Gurdal, Z., & Olmedo, R. (1993). In-plane response of laminates with spatially varying fiber orientations-variable stiffness concept. AIAA journal, 31(4), 751-758.

81. Masjedi, P. K., & Weaver, P. M. (2021). Variable stiffness composite beams subject to non-uniformly distributed loads: an analytical solution. Composite Structures, 256, 112975.

82. Günay, M. G., & Timarci, T. (2017). Static analysis of thin-walled laminated composite closed-section beams with variable stiffness. Composite structures, 182, 67-78.

83. Jegley, D., Tatting, B., & Gurdal, Z. (2003, April). Optimization of elastically tailored tow-placed plates with holes. In 44th AIAA/ASME/ASCE/AHS/ASC structures, structural dynamics, and materials conference (p. 1420).

84. Zhong, J., Zheng, Y., Chen, J., & Jing, Z. (2019). Variable-stiffness composite cylinder design under combined loadings by using the improved Kriging model. Acta Mechanica Sinica, 35, 201-211.

85. Rao, K. M., & Meyer-Piening, H. R. (1990). Analysis of thick laminated anisotropic composite plates by the finite element method. Composite Structures, 15(3), 185-213.

86. Loredo, A., d'Ottavio, M., Vidal, P., & Polit, O. (2019). A family of higher-order single layer plate models meeting Cz0-requirements for arbitrary laminates. Composite Structures, 225, 111146.

87. Abrate, S., & Di Sciuva, M. (2017). Equivalent single layer theories for composite and sandwich structures: A review. Composite Structures, 179, 482-494.

88. Barut, A., Madenci, E., Anderson, T., & Tessler, A. (2002). Equivalent single-layer theory for a complete stress field in sandwich panels under arbitrarily distributed loading. Composite Structures, 58(4), 483-495.

89. Versino, D., Gherlone, M., Mattone, M., Di Sciuva, M., & Tessler, A. (2013). C0 triangular elements based on the Refined Zigzag Theory for multilayer composite and sandwich plates. Composites Part B: Engineering, 44(1), 218-230.
90. Reissner, E. (1984). On a certain mixed variational theorem and a proposed application. International Journal for Numerical Methods in Engineering, 20(7), 1366-1368.
91. Liu, D., & Li, X. (1996). An overall view of laminate theories based on displacement hypothesis. Journal of composite materials, 30(14), 1539-1561.
92. Murakami, H. (1986). Laminated composite plate theory with improved in-plane responses. Journal of Applied Mechanics, 53(3), 661-666.
93. Ferreira, A. J. M. (2005). Analysis of composite plates using a layerwise theory and multiquadrics discretization. Mechanics of Advanced Materials and Structures, 12(2), 99-112.
94. Carrera, E. (1998). Evaluation of layerwise mixed theories for laminated plates analysis. AIAA journal, 36(5), 830-839.
95. Thai, C. H., Ferreira, A. J. M., Carrera, E., & Nguyen-Xuan, H. (2013). Isogeometric analysis of laminated composite and sandwich plates using a layerwise deformation theory. Composite Structures, 104, 196-214.
96. Ferreira, A. J. M., Fasshauer, G. E., Batra, R. C., & Rodrigues, J. D. (2008). Static deformations and vibration analysis of composite and sandwich plates using a layerwise theory and RBF-PS discretizations with optimal shape parameter. Composite structures, 86(4), 328-343.
97. Toledano, A., & Murakami, H. (1987). A composite plate theory for arbitrary laminate configurations, Journal of Applied Mechanics, 54(1), 181-189.
98. Thai, C. H., Ferreira, A. J. M., Abdel Wahab, M., & Nguyen-Xuan, H. (2016). A generalized layerwise higher-order shear deformation theory for laminated composite and sandwich plates based on isogeometric analysis. Acta Mechanica, 227(5), 1225-1250.
99. DI SCIUVA, M. (1984). A refinement of the transverse shear deformation theory for multilayered of orthotropic plates. Aerotecnica Missili e Spazio, (2), 84-92.
100. Averill, R. C., & Yip, Y. (1996). Thick beam theory and finite element model with zig-zag sublaminate approximations. AIAA journal, 34(8), 1627-1632.

101. Aitharaju, V. R., & Averill, R. C. (1999). C 0 zig-zag finite element for analysis of laminated composite beams. Journal of Engineering mechanics, 125(3), 323-330.
102. Kapuria, S., Dumir, P. C., & Ahmed, A. (2003). An efficient higher order zigzag theory for composite and sandwich beams subjected to thermal loading. International Journal of Solids and Structures, 40(24), 6613-6631.
103. Tornabene, F., Fantuzzi, N., & Bacciocchi, M. (2019). Refined shear deformation theories for laminated composite arches and beams with variable thickness: Natural frequency analysis. Engineering Analysis with Boundary Elements, 100, 24-47.
104. Carrera, E. (2001). Developments, ideas, and evaluations based upon Reissner's Mixed Variational Theorem in the modeling of multilayered plates and shells. Appl. Mech. Rev., 54(4), 301-329.
105. Antunes, A. M., Ribeiro, P., Rodrigues, J. D., & Akhavan, H. (2020). Modal analysis of a variable stiffness composite laminated plate with diverse boundary conditions: experiments and modelling. Composite Structures, 239, 111974.
106. Manickam, G., Bharath, A., Das, A. N., Chandra, A., & Barua, P. (2018). Thermal buckling behaviour of variable stiffness laminated composite plates. Materials Today Communications, 16, 142-151.
107. Reissner, E., & Stavsky, Y. (1961). Bending and stretching of certain types of heterogeneous aeolotropic elastic plates, Journal of Applied Mechanics, 28(3), 402-408.
108. Whitney, J. M., & Pagano, N. J. (1970). Shear deformation in heterogeneous anisotropic plates, 37(4), Journal of Applied Mechanics, 1031-1036.
109. Mindlin, R. (1951). Influence of rotatory inertia and shear on flexural motions of isotropic, elastic plates.
110. Jones, R. M. (1998). Mechanics of composite materials. CRC press.
111. Reissner, E. (1985). Reflections on the theory of elastic plates.
112. Noor, A. K., & Burton, W. S. (1989). Assessment of shear deformation theories for multilayered composite plates.
113. Librescu, L., Khdeir, A. A., & Reddy, J. N. (1987). A comprehensive analysis of the state of stress of elastic anisotropic flat plates using refined theories. Acta Mechanica, 70(1-4), 57-81.

114. Akhavan, H., & Ribeiro, P. (2011). Natural modes of vibration of variable stiffness composite laminates with curvilinear fibers. Composite Structures, 93(11), 3040-3047.
115. Groh, R. M. J., Weaver, P. M., White, S., Raju, G., & Wu, Z. (2013). A 2D equivalent single-layer formulation for the effect of transverse shear on laminated plates with curvilinear fibres. Composite Structures, 100, 464-478.
116. Akhavan, H., Ribeiro, P., & De Moura, M. F. S. F. (2013). Large deflection and stresses in variable stiffness composite laminates with curvilinear fibres. International Journal of Mechanical Sciences, 73, 14-26.
117. Reddy, J. N. (1987). A generalization of two-dimensional theories of laminated composite plates. Communications in applied numerical methods, 3(3), 173-180.
118. Pagani, A., & Sanchez-Majano, A. R. (2022). Influence of fiber misalignments on buckling performance of variable stiffness composites using layerwise models and random fields. Mechanics of Advanced Materials and Structures, 29(3), 384-399.
119. Raju, G., Wu, Z., & Weaver, P. M. (2015). Buckling and postbuckling of variable angle tow composite plates under in-plane shear loading. International Journal of Solids and Structures, 58, 270-287.
120. Diaz, J., Fagiano, C., Abdalla, M. M., Gürdal, Z., & Hernandez, S. (2012). A study of interlaminar stresses in variable stiffness plates. Composite Structures, 94(3), 1192-1199.
121. Yazdani, S., & Ribeiro, P. (2014). Geometrically non-linear static analysis of unsymmetric composite plates with curvilinear fibres: p-version layerwise approach. Composite Structures, 118, 74-85.
122. Fagiano, C., Abdalla, M. M., Kassapoglou, C., & Gürdal, Z. (2010). Interlaminar stress recovery for three-dimensional finite elements. Composites Science and Technology, 70(3), 530-538.
123. Demasi, L. (2013). Partially layer wise advanced zig zag and HSDT models based on the generalized unified formulation. Engineering Structures, 53, 63-91.
124. Piegl, L., & Tiller, W. (1996). The NURBS book. Springer Science & Business Media.
125. Pagani, A., Carrera, E., Augello, R., & Scano, D. (2021). Use of Lagrange polynomials to build refined theories for laminated beams, plates and shells. Composite Structures, 276, 114505.

126. Carrera, E. (2003). Historical review of zig-zag theories for multilayered plates and shells. Appl. Mech. Rev., 56(3), 287-308.
127. Di Sciuva, M. (1985). Development of an anisotropic, multilayered, shear-deformable rectangular plate element. Computers & structures, 21(4), 789-796.
128. Di Sciuva, M. (1986). Evaluation of some multilayered, shear-deformable plate elements. Computers & structures, 24(6), 845-854.
129. Di Sciuva, M. (1986). Bending, vibration and buckling of simply supported thick multilayered orthotropic plates: an evaluation of a new displacement model. Journal of Sound and Vibration, 105(3), 425-442.
130. Di Sciuva, M. (1992). Multilayered anisotropic plate models with continuous interlaminar stresses. Composite Structures, 22(3), 149-167.
131. Di Sciuva, M. (1987). An improved Shear-Deformation theory for moderately thick multilayered anisotropic shells and plates. Journal of Applied Mechanics, 54(3), 589–596.
132. Di Sciuva, M., Gherlone, M., & Librescu, L. (2002). Implications of damaged interfaces and of other non-classical effects on the load carrying capacity of multilayered composite shallow shells. International journal of non-linear mechanics, 37(4-5), 851-867.
133. Carrera, E. (2002). Theories and finite elements for multilayered, anisotropic, composite plates and shells. Archives of Computational Methods in Engineering, 9(2), 87–140.
134. Trinh, L. C., Ojo, S. O., Groh, R. M., & Weaver, P. M. (2021). A mixed inverse differential quadrature method for static analysis of constant-and variable-stiffness laminated beams based on Hellinger-Reissner mixed variational formulation. International Journal of Solids and Structures, 210, 66-87.
135. Carrera, E. (2004). On the use of the Murakami's zig-zag function in the modeling of layered plates and shells. Computers & Structures, 82(7-8), 541-554.
136. Gupta, A., & Pradyumna, S. (2021). Geometrically nonlinear bending analysis of variable stiffness composite laminated shell panels with a higher-order theory. Composite Structures, 276, 114527.
137. Carrera, E., & Ciuffreda, A. (2005). A unified formulation to assess theories of multilayered plates for various bending problems. Composite Structures, 69(3), 271-293.

138. Demasi, L., Santarpia, E., Cavallaro, R., Biagini, G., & Vannucci, F. (2017). Zig-Zag and Layerwise Models for Variable-Stiffness Composite Laminates Based on the Generalized Unified Formulation. In 58th AIAA/ASCE/AHS/ASC Structures, Structural Dynamics, and Materials Conference (p. 0891).
139. Demasi, L., Biagini, G., Vannucci, F., Santarpia, E., & Cavallaro, R. (2018). Generalized unified formulation-based bending analysis of variable angle tow panels in the presence of hole. In 2018 AIAA/ASCE/AHS/ASC Structures, Structural Dynamics, and Materials Conference (p. 1706).
140. Demasi, L., Biagini, G., Vannucci, F., Santarpia, E., & Cavallaro, R. (2017). Equivalent single layer, zig-zag, and layer wise theories for variable angle tow composites based on the generalized unified formulation. Composite Structures, 177, 54-79.
141. Demasi, L., Ashenafi, Y., Cavallaro, R., & Santarpia, E. (2015). Generalized Unified Formulation shell element for functionally graded Variable-Stiffness Composite Laminates and aeroelastic applications. Composite Structures, 131, 501-515.
142. Tornabene, F., & Bacciocchi, M. (2018). Effect of curvilinear reinforcing fibers on the linear static behavior of soft-core sandwich structures. Journal of Composites Science, 2(1), 14.
143. Ribeiro, P. (2015). Non-linear modes of vibration of thin cylindrical shells in composite laminates with curvilinear fibres. Composite Structures, 122, 184-197.
144. Blom, A. W., Setoodeh, S., Hol, J. M., & Gürdal, Z. (2008). Design of variable-stiffness conical shells for maximum fundamental eigenfrequency. Computers & structures, 86(9), 870-878.
145. Blom, A. W., Tatting, B. F., Hol, J. M., & Gürdal, Z. (2009). Fiber path definitions for elastically tailored conical shells. Composites part B: engineering, 40(1), 77-84.
146. Tornabene, F., Fantuzzi, N., Bacciocchi, M., & Viola, E. (2015). Higher-order theories for the free vibrations of doubly-curved laminated panels with curvilinear reinforcing fibers by means of a local version of the GDQ method. Composites Part B: Engineering, 81, 196-230.
147. Tornabene, F., Fantuzzi, N., & Bacciocchi, M. (2016). Higher-order structural theories for the static analysis of doubly-curved laminated composite panels reinforced by curvilinear fibers. Thin-Walled Structures, 102, 222-245.

148. Ojo, S. O., Zucco, G., & Weaver, P. M. (2021). Efficient three-dimensional geometrically nonlinear analysis of variable stiffness composite beams using strong Unified Formulation. Thin-Walled Structures, 163, 107672.
149. Patni, M., Minera, S., Groh, R. M. J., Pirrera, A., & Weaver, P. M. (2019). On the accuracy of localised 3D stress fields in tow-steered laminated composite structures. Composite Structures, 225, 111034.
150. Tornabene, F., Viola, E., & Fantuzzi, N. (2013). General higher-order equivalent single layer theory for free vibrations of doubly-curved laminated composite shells and panels. Composite Structures, 104, 94-117.
151. Viola, E., Tornabene, F., & Fantuzzi, N. (2013). Static analysis of completely doubly-curved laminated shells and panels using general higher-order shear deformation theories. Composite Structures, 101, 59-93.
152. Patni, M., Minera, S., Groh, R., Weaver, P. M., & Pirrera, A. (2019b). Efficient 3D stress capture of variable stiffness and sandwich beam structures. AIAA Scitech 2019 Forum.
153. Gherlone, M. (2013). On the use of zigzag functions in equivalent single layer theories for laminated composite and sandwich beams: a comparative study and some observations on external weak layers. Journal of Applied Mechanics, 80(6), 061004.
154. Vel, S. S., & Batra, R. C. (2002). Exact solution for thermoelastic deformations of functionally graded thick rectangular plates. AIAA journal, 40(7), 1421-1433.
155. Kumari, P., Singh, A., Rajapakse, R. K. N. D., & Kapuria, S. (2017). Three-dimensional static analysis of Levy-type functionally graded plate with in-plane stiffness variation. Composite Structures, 168, 780-791.
156. Pan, E. (2003). Exact solution for functionally graded anisotropic elastic composite laminates. Journal of Composite Materials, 37(21), 1903-1920.
157. Pagano, N. J. (1970). Exact solutions for rectangular bidirectional composites and sandwich plates. Journal of composite materials, 4(1), 20-34.
158. Fouaidi, M., Jamal, M., Zaite, A., & Belouaggadia, N. (2021). Bending analysis of functionally graded graphene oxide powder-reinforced composite beams using a meshfree method. Aerospace Science and Technology, 110, 106479.
159. Karamanlı, A. (2017). Bending behaviour of two directional functionally graded sandwich beams by using a quasi-3d shear deformation theory. Composite structures, 174, 70-86.

160. Li, J., Wang, G., Guan, Y., Zhao, G., Lin, J., Naceur, H., & Coutellier, D. (2021). Meshless analysis of bi-directional functionally graded beam structures based on physical neutral surface. Composite Structures, 259, 113502.
161. Ferreira, A. J. M., Batra, R. C., Roque, C. M. C., Qian, L. F., & Martins, P. A. L. S. (2005). Static analysis of functionally graded plates using third-order shear deformation theory and a meshless method. Composite structures, 69(4), 449-457.
162. Ferreira, A. J., Roque, C. M. C., Jorge, R. M. N., Fasshauer, G. E., & Batra, R. C. (2007). Analysis of functionally graded plates by a robust meshless method. Mechanics of Advanced Materials and Structures, 14(8), 577-587.
163. Ventura, G. (2002). An augmented Lagrangian approach to essential boundary conditions in meshless methods. International Journal for Numerical Methods in Engineering, 53(4), 825-842.
164. Liew, K. M., Zhao, X., & Ferreira, A. J. (2011). A review of meshless methods for laminated and functionally graded plates and shells. Composite Structures, 93(8), 2031-2041.
165. Chen, Y., Lee, J. D., & Eskandarian, A. (2006). Meshless methods in solid mechanics (pp. 97-106). New York: Springer.
166. Zenkour, A. M., & Alghamdi, N. A. (2010). Bending analysis of functionally graded sandwich plates under the effect of mechanical and thermal loads. Mechanics of Advanced Materials and Structures, 17(6), 419-432.
167. Reddy, J. N., Wang, C. M., & Kitipornchai, S. (1999). Axisymmetric bending of functionally graded circular and annular plates. European Journal of Mechanics-A/Solids, 18(2), 185-199.
168. Mantari, J. L., & Granados, E. V. (2015). A refined FSDT for the static analysis of functionally graded sandwich plates. Thin-Walled Structures, 90, 150-158.
169. Singha, M. K., Prakash, T., & Ganapathi, M. (2011). Finite element analysis of functionally graded plates under transverse load. Finite elements in Analysis and Design, 47(4), 453-460.
170. Thai, H. T., Nguyen, T. K., Vo, T. P., & Lee, J. (2014). Analysis of functionally graded sandwich plates using a new first-order shear deformation theory. European Journal of Mechanics-A/Solids, 45, 211-225.
171. Tornabene, F., & Viola, E. (2013). Static analysis of functionally graded doubly-curved shells and panels of revolution. Meccanica, 48, 901-930.

172. Nguyen, T. K., Sab, K., & Bonnet, G. (2007). Shear correction factors for functionally graded plates. Mechanics of Advanced Materials and Structures, 14(8), 567-575.

173. Nguyen, T. K., Sab, K., & Bonnet, G. (2008). First-order shear deformation plate models for functionally graded materials. Composite Structures, 83(1), 25-36.

174. Reddy, J. (2000). Analysis of functionally graded plates. International Journal for numerical methods in engineering, 47(1-3), 663-684.

175. Taj, M. G., Chakrabarti, A., & Sheikh, A. H. (2013). Analysis of functionally graded plates using higher order shear deformation theory. Applied Mathematical Modelling, 37(18-19), 8484-8494.

176. Mantari, J. L., Oktem, A. S., & Soares, C. G. (2012). A new higher order shear deformation theory for sandwich and composite laminated plates. Composites Part B: Engineering, 43(3), 1489-1499.

177. Daikh, A. A., & Zenkour, A. M. (2019). Effect of porosity on the bending analysis of various functionally graded sandwich plates. Materials Research Express, 6(6), 065703.

178. Mahi, A., & Tounsi, A. (2015). A new hyperbolic shear deformation theory for bending and free vibration analysis of isotropic, functionally graded, sandwich and laminated composite plates. Applied mathematical modelling, 39(9), 2489-2508.

179. Mantari, J. L., Oktem, A. S., & Soares, C. G. (2012). Bending response of functionally graded plates by using a new higher order shear deformation theory. Composite Structures, 94(2), 714-723.

180. Reddy, J. N., & Liu, C. (1985). A higher-order shear deformation theory of laminated elastic shells. International journal of engineering science, 23(3), 319-330.

181. Pandey, S., & Pradyumna, S. (2018). Analysis of functionally graded sandwich plates using a higher-order layerwise theory. Composites part B: engineering, 153, 325-336.

182. Liu, N., & Jeffers, A. E. (2017). Isogeometric analysis of laminated composite and functionally graded sandwich plates based on a layerwise displacement theory. Composite Structures, 176, 143-153.

183. Hirane, H., Belarbi, M. O., Houari, M. S. A., & Tounsi, A. (2021). On the layerwise finite element formulation for static and free vibration analysis of functionally graded sandwich plates. Engineering with computers, 1-29.
184. Li, D. (2021). Layerwise theories of laminated composite structures and their applications: a review. Archives of Computational Methods in Engineering, 28, 577-600.
185. Carrera, E., Brischetto, S., Cinefra, M., & Soave, M. (2011). Effects of thickness stretching in functionally graded plates and shells. Composites Part B: Engineering, 42(2), 123-133.
186. Mantari, J. L., Ramos, I. A., Carrera, E., & Petrolo, M. (2016). Static analysis of functionally graded plates using new non-polynomial displacement fields via Carrera Unified Formulation. Composites Part B: Engineering, 89, 127-142.
187. Rahmani, F., Kamgar, R., & Rahgozar, R. (2023). Analysis of metallic and functionally graded beams using isogeometric approach and Carrera Unified Formulation. Mechanics of Advanced Materials and Structures, 30(4), 894-911.
188. Gorgeri, A., Vescovini, R., & Dozio, L. (2022). Sublaminate variable kinematics shell models for functionally graded sandwich panels: Bending and free vibration response. Mechanics of Advanced Materials and Structures, 29(1), 15-32.
189. Carrera, E. (1996). C0 Reissner–Mindlin multilayered plate elements including zig-zag and interlaminar stress continuity. International Journal for Numerical Methods in Engineering, 39(11), 1797-1820.
190. Demasi, L. (2009). ∞ 6 Mixed plate theories based on the Generalized Unified Formulation. Part IV: Zig-zag theories. Composite Structures, 87(3), 195-205.
191. Khan, A. A., Naushad Alam, M., & Wajid, M. (2016). Finite element modelling for static and free vibration response of functionally graded beam. Latin American journal of solids and structures, 13, 690-714.
192. Nath, J. K., & Das, T. (2019). Static and free vibration analysis of multilayered functionally graded shells and plates using an efficient zigzag theory. Mechanics of Advanced Materials and Structures, 26(9), 770-788.
193. Natarajan, S., & Manickam, G. (2012). Bending and vibration of functionally graded material sandwich plates using an accurate theory. Finite Elements in Analysis and Design, 57, 32-42.
194. Garg, A., Chalak, H. D., & Chakrabarti, A. (2022). Bending analysis of functionally graded sandwich plates using HOZT including transverse

displacement effects. Mechanics based design of structures and machines, 50(10), 3563-3577.

195. Neves, A. M. A., Ferreira, A. J., Carrera, E., Cinefra, M., Jorge, R. M. N., & Soares, C. M. M. (2012). Static analysis of functionally graded sandwich plates according to a hyperbolic theory considering Zig-Zag and warping effects. Advances in Engineering Software, 52, 30-43.

196. Iurlaro, L. (2015). Development of Refined Models for Multilayered Composite and Sandwich Structures Analytical Formulation, FEM Implementation and Experimental Assessment: Thesis.

197. Iurlaro L, Gherlone M, Di Sciuva M. A comparison of zigzag functions for the bending, vibration and buckling analysis of multilayered composite and sandwich plates. Proc. 11th World Conf. Comput. Methods, Barcelona, Spain, 2014.

198. Iurlaro, L., Gherlone, M., & Di Sciuva, M. (2014). Bending and free vibration analysis of functionally graded sandwich plates using the refined zigzag theory. Journal of Sandwich Structures & Materials, 16(6), 669-699.

199. Tessler, A., Gherlone, M., Versino, D., & Di Sciuva, M. (2012). Analytic and computational perspectives of multi-scale theory for homogeneous, laminated composite, and sandwich beams and plates.

200. Gherlone, M., Tessler, A., & Di Sciuva, M. (2011). C0 beam elements based on the refined zigzag theory for multilayered composite and sandwich laminates. Composite Structures, 93(11), 2882-2894.

201. Di Sciuva, M., Gherlone, M., Iurlaro, L., & Tessler, A. (2015). A class of higher-order C0 composite and sandwich beam elements based on the Refined Zigzag Theory. Composite Structures, 132, 784-803.

202. Wimmer, H., & Celigoj, C. (2021). An edge-based smoothed three-node composite plate element with refined zigzag kinematics. Composite Structures, 274, 114204.

203. Honda, S., & Narita, Y. (2016, September). Vibration analysis and optimization of sandwich composite with curvilinear fibers. In Journal of Physics: Conference Series (Vol. 744, No. 1, p. 012020). IOP Publishing.

204. Farhatnia, F., & Sarami, M. (2019). Finite element approach of bending and buckling analysis of FG beams based on refined zigzag theory. Universal Journal of Mechanical Engineering, 7(4), 147-158.

205. Chen, C. D., & Su, P. W. (2021). An analytical solution for vibration in a functionally graded sandwich beam by using the refined zigzag theory. Acta Mechanica, 232, 4645-4668.

206. Di Sciuva, M., & Sorrenti, M. (2021). Bending and free vibration analysis of functionally graded sandwich plates: An assessment of the Refined Zigzag Theory. Journal of Sandwich Structures & Materials, 23(3), 760-802.

207. Dorduncu, M. (2020). Stress analysis of sandwich plates with functionally graded cores using peridynamic differential operator and refined zigzag theory. Thin-Walled Structures, 146, 106468.

208. Dorduncu, M. (2020). Peridynamic modeling of adhesively bonded beams with modulus graded adhesives using refined zigzag theory. International Journal of Mechanical Sciences, 185, 105866.

209. Kashtalyan, M. (2004). Three-dimensional elasticity solution for bending of functionally graded rectangular plates. European Journal of Mechanics-A/Solids, 23(5), 853-864.

210. Jin, G., Su, Z., Shi, S., Ye, T., & Gao, S. (2014). Three-dimensional exact solution for the free vibration of arbitrarily thick functionally graded rectangular plates with general boundary conditions. Composite Structures, 108, 565-577.

211. Ferreira, A. J. M. (2003). A formulation of the multiquadric radial basis function method for the analysis of laminated composite plates. Composite structures, 59(3), 385-392.

212. Liu, G. R., Zhao, X., Dai, K. Y., Zhong, Z. H., Li, G. Y., & Han, X. (2008). Static and free vibration analysis of laminated composite plates using the conforming radial point interpolation method. Composites Science and Technology, 68(2), 354-366.

213. Moosavi, M. R., Delfanian, F., & Khelil, A. (2011). The orthogonal meshless finite volume method for solving Euler–Bernoulli beam and thin plate problems. Thin-walled structures, 49(7), 923-932.

214. Diyaroglu, C., Oterkus, E., Madenci, E., Rabczuk, T., & Siddiq, A. (2016). Peridynamic modeling of composite laminates under explosive loading. Composite Structures, 144, 14-23.

215. Ma, X., Zhou, B., & Xue, S. (2022). A Hermite interpolation element-free Galerkin method for functionally graded structures. Applied Mathematics and Computation, 419, 126865.

216. Gruttmann, F., & Wagner, W. (2004). A stabilized one-point integrated quadrilateral Reissner–Mindlin plate element. International Journal for Numerical Methods in Engineering, 61(13), 2273-2295.
217. Yuqiu, L., & Fei, X. (1992). A universal method for including shear deformation in thin plate elements. International journal for numerical methods in engineering, 34(1), 171-177.
218. Hughes, T. J., Cohen, M., & Haroun, M. (1978). Reduced and selective integration techniques in the finite element analysis of plates. Nuclear Engineering and design, 46(1), 203-222.
219. Zienkiewicz, O. C., Taylor, R. L., Papadopoulos, P., & Oñate, E. (1990). Plate bending elements with discrete constraints: new triangular elements. Computers & Structures, 35(4), 505-522.
220. Hinton, E., & Huang, H. C. (1986). A family of quadrilateral Mindlin plate elements with substitute shear strain fields. Computers & structures, 23(3), 409-431.
221. Oñate, E., Zienkiewicz, O. C., Suarez, B., & Taylor, R. L. (1992). A general methodology for deriving shear constrained Reissner-Mindlin plate elements. International journal for numerical methods in engineering, 33(2), 345-367.
222. Katili, I. (1993). A new discrete Kirchhoff-Mindlin element based on Mindlin–Reissner plate theory and assumed shear strain fields—part II: An extended DKQ element for thick-plate bending analysis. International Journal for Numerical Methods in Engineering, 36(11), 1885-1908.
223. Katili, I. (1993). A new discrete Kirchhoff-Mindlin element based on Mindlin-Reissner plate theory and assumed shear strain fields—part I: An extended DKT element for thick-plate bending analysis. International Journal for Numerical Methods in Engineering, 36(11), 1859-1883.
224. Batoz, J. L., & Katili, I. (1992). On a simple triangular Reissner/Mindlin plate element based on incompatible modes and discrete constraints. International Journal for Numerical Methods in Engineering, 35(8), 1603-1632.
225. Batoz, J. L., & Lardeur, P. (1989). A discrete shear triangular nine dof element for the analysis of thick to very thin plates. International journal for numerical methods in engineering, 28(3), 533-560.

226. Bletzinger, K. U., Bischoff, M., & Ramm, E. (2000). A unified approach for shear-locking-free triangular and rectangular shell finite elements. Computers & Structures, 75(3), 321-334.

227. Schnabl, S., Saje, M., Turk, G., & Planinc, I. (2007). Locking-free two-layer Timoshenko beam element with interlayer slip. Finite Elements in Analysis and Design, 43(9), 705-714.

228. Edem, I. B. (2006). The exact two-node Timoshenko beam finite element using analytical bending and shear rotation interdependent shape functions. International Journal for Computational Methods in Engineering Science and Mechanics, 7(6), 425-431.

229. Reddy, J. (1997). On locking-free shear deformable beam finite elements. Computer methods in applied mechanics and engineering, 149(1-4), 113-132.

230. Bathe, K. J., Iosilevich, A., & Chapelle, D. (2000). An evaluation of the MITC shell elements. Computers & Structures, 75(1), 1-30.

231. Bucalem, M. L., & Bathe, K. J. (1993). Higher-order MITC general shell elements. International Journal for Numerical Methods in Engineering, 36(21), 3729-3754.

232. Bathe, K. J., & Brezzi, F. (1985). On the convergence of a four–node plate bending element based on Mindlin/Reissner plate theory and a mixed interpolation. In The mathematics of finite elements and applications (pp. 491-503). Academic Press.

233. Bathe, K. J., & Dvorkin, E. N. (1986). A formulation of general shell elements—the use of mixed interpolation of tensorial components. International journal for numerical methods in engineering, 22(3), 697-722.

234. Dvorkin, E. N., & Bathe, K. J. (1984). A continuum mechanics based four-node shell element for general non-linear analysis. Engineering computations, 1(1), 77-88.

235. Tessler, A., & Mohr, J. W. (2000, June). A three-node shell element with drilling degrees of freedom for laminated composite and sandwich structures. In Fourth International Colloquium on Computation of Shell & Spatial Structures. Chania, Crete, Greece.

236. Tessler, A., & Hughes, T. J. (1985). A three-node Mindlin plate element with improved transverse shear. Computer Methods in Applied Mechanics and Engineering, 50(1), 71-101.

237. Tessler, A., & Dong, S. B. (1981). On a hierarchy of conforming Timoshenko beam elements. Computers & structures, 14(3-4), 335-344.
238. Tessler, A. (2000, August). Comparison of interdependent interpolations for membrane and bending kinematics in shear-deformable shell elements. In Proceedings of international conference on computational engineering and sciences, Los Angeles, CA.
239. Zienkiewicz, O. C., & Taylor, R. L. (2005). The finite element method for solid and structural mechanics. Elsevier.
240. Anderson, T., Madenci, E., Burton, W. S., & Fish, J. C. (1998). Analytical solution of finite-geometry composite panels under transient surface loading. International journal of solids and structures, 35(12), 1219-1239.
241. Zoghipour, P., Hasim, K. A., Kefal, A., & Yildiz, M. (2023). Implementation of shear-locking-free triangular refined zigzag element for structural analysis of multilayered plates with curvilinear fibers. Composite Structures, 305, 116462.